Fluorescence Anisotropy Measurements of Single Molecules to Probe Solution-Phase Conformational Heterogeneity of Intrinsically Disordered Proteins

By
Lydia H. Manger

A dissertation submitted in partial fulfillment
of the requirements for the degree of

Doctor of Philosophy
(Chemistry)

at the
UNIVERSITY OF WISCONSIN-MADISON
2018

Date of final oral examination: August 6, 2018

The dissertation is approved by the following members of the Final Oral Committee:

Randall Goldsmith, Assistant Professor, Chemistry
James Weisshaar, Professor, Chemistry
Aaron Hoskins, Assistant Professor, Biochemistry
John Wright, Professor, Chemistry

Abstract

Single-molecule studies have opened a new avenue to pursue the heterogeneity of molecular systems that is obscured at the bulk level. Likewise, time-correlated single photon counting methods can provide characterization of evolving populations of photoexcited species that contribute to a bulk property such as photoluminescence.

Tau protein is an intrinsically disordered protein (IDP) that is implicated in neurodegenerative diseases such as Alzheimer's disease. Characterizing and understanding the conformations that this protein adopts in solution is critical to understanding disease pathology. We examine the conformations adopted by tau protein in solution at the single-molecule level in order to elucidate the extent of structural heterogeneity. Traditional single-molecule fluorescence studies of proteins, however, rely on recording freely-diffusing molecules as they pass through a confocal volume — resulting in short observation time and unrestricted motion — or tethering the molecule to a surface — providing longer observation times but potentially introducing artifacts. Herein we describe the use of the anti-Brownian electrokinetic (ABEL) trap to prolong measurement of the anisotropy of individual proteins in solution to investigate the diversity of conformations sampled by the protein. In Chapter 2 we describe how tau protein exists in two families of conformations in solution, differentiated by their degree of compaction. Chapter 3 then provides an overview of different labeling positions that may be useful for further studying the conformational heterogeneity of tau protein.

In Chapter 4, we describe a study of the recombination kinetics of a metal halide perovskite, methylammonium lead iodide ($MAPbI_3$). Time-resolved photoluminescence is recorded using time-correlated single photon counting. These measurements provide insight into the time-varying populations of the photoexcited species present in the material that are obscured at the bulk level. These

measurements are then used to define a set of rate equations to describe the evolving populations, leading us to invoke geminate recombination as an important method for recombination of electrons and holes.

Acknowledgements

My time in graduate school is a blur. Even though I have looked forward to this day for years, I can't believe it has come to an end. The people I have met here, and the friends I made along the way, make this ending bittersweet. I wouldn't have made it through grad school had it not been for the friends I made and their willingness to listen when I needed to talk or make me laugh when I needed to be cheered up.

I would like to thank the whole Goldsmith group, past (Angela, Katie, Kevin, Sharla, Sudheer, Sunil) and present (Alex, Andrew, Ceci, Daniel, David, Erik, Feng, Hoang, James, Kasie, Levi, Mike, Morgan, Ruohan, Veronica), for their support and friendship over the years. You were some of the greatest people to work with, and I doubt I'll have an office that shares as many laughs (or baked goods) as we did. I will truly miss the time I spent with all of you.

I would like to thank the whole UW-Madison Chemistry department for making this a great place to work and live for the past 5 years. Special thanks to all the staff that help the department run smoothly. The department also provided a great environment for collaborations and I was lucky to have some great collaborators from whom I learned a lot. I also thank Michael Holden and Martin Margittai from the University of Denver for providing us with tau protein and sharing their knowledge.

I would like to thank Randy for being the best advisor. He has been supportive and encouraging throughout the high and low points of research, yet still pushed me to grow as a scientist. The opportunity to dive into the perovskite literature and embrace a new project was an invaluable learning experience and gave me confidence in my ability to teach myself a new field of research. And I would like to thank the others on my committee – Aaron, Jim and John – for their support and participation in my graduate school journey.

Lastly, I thank my family for their love and support. My mom deserves a special acknowledgement for providing me with everything I have needed to succeed over the years.

Table of Contents

List of Figures

List of Tables

Publications

(1) **Lydia H. Manger**, A.K. Foote, S.L. Wood, M.R. Holden, K.D. Heylman, M. Margittai, R.H. Goldsmith. "Revealing Conformational Variants of Solution-Phase Intrinsically Disordered Tau Protein at the Single-Molecule Level." *Angewandte Chemie Int. Ed*. **2017, 56**(49):15584-15588 (Designated "Hot Paper" by editor)

(2) Y. Fu, M.T. Rea, J. Chen, D. Morrow, M.P. Hautzinger, Y. Zhao, D. Pan, **Lydia H. Manger**, J.C. Wright, R.H. Goldsmith, S. Jin. "Selective Stabilization and Photophysical Properties of Metastable Perovskite Polymorphs of $CsPbI_3$ in Thin Films." *Chemistry of Materials* **2017**.

(3) **Lydia H. Manger**, M.B. Rowley, Y. Fu, A.K. Foote, M.T. Rea, S.L. Wood, S. Jin, J.C. Wright, R.H. Goldsmith. "Global Analysis of Perovskite Photophysics Reveals Importance of Geminate Pathways." *Journal of Physical Chemistry C* **2017, 121**(2)**:** 1062-1071.

(4) J. Dai, Y. Fu, **Lydia H. Manger**, M.T. Rea, L. Hwang, R.H. Goldsmith, S. Jin. "Carrier Decay Properties of Mixed Cation Formamidinium–Methylammonium Lead Iodide Perovskite $[HC(NH_2)_2]_{1-x}[CH_3NH_3]_xPbI_3$ Nanorods." *Journal of Physical Chemistry Letters* **2016:** 5036-5043.

Chapter 1

1. Introduction to Tau Protein and the ABEL Trap

1.1 Intrinsically Disordered Proteins (IDPs)

Proteins are versatile macromolecules that perform a variety of essential biological functions. Traditionally, the amino acid sequence was thought to determine its conformation, and that conformation subsequently determined its function, known as the structure-function paradigm.[2] Around the year 2000, however, the number of publications related to intrinsically disordered proteins (IDPs) started to increase exponentially.[3] These uncharacterized proteins challenged the traditional understanding of the structure-function relationship because they had no well-defined equilibrium structure and instead consisted of an ensemble of highly dynamic conformers with similar free energies.[3-5] While originally thought to be artifacts that did not conform to the paradigm, they have since proved to be important players in cell signaling, regulation, recognition and pathogenesis, their structural plasticity lending functional diversity.[3, 5-6] In fact, strictly ordered proteins only comprise about 50 % of various proteomes and are not the ubiquitous presence that was once thought.[6]

Only about a third of the crystal structures in the protein data bank are fully ordered.[6] Instead, proteins exist along a continuum of increasing disorder: folded, molten globule, premolten globule and unfolded/random coil (Figure 1-1).[6-8] The molten globule state was added to the traditional folded/unfolded binary to describe intermediate conformational states that lacked native tertiary structure.[8] Then a fourth state — premolten globule — was added to describe a subset of unfolded

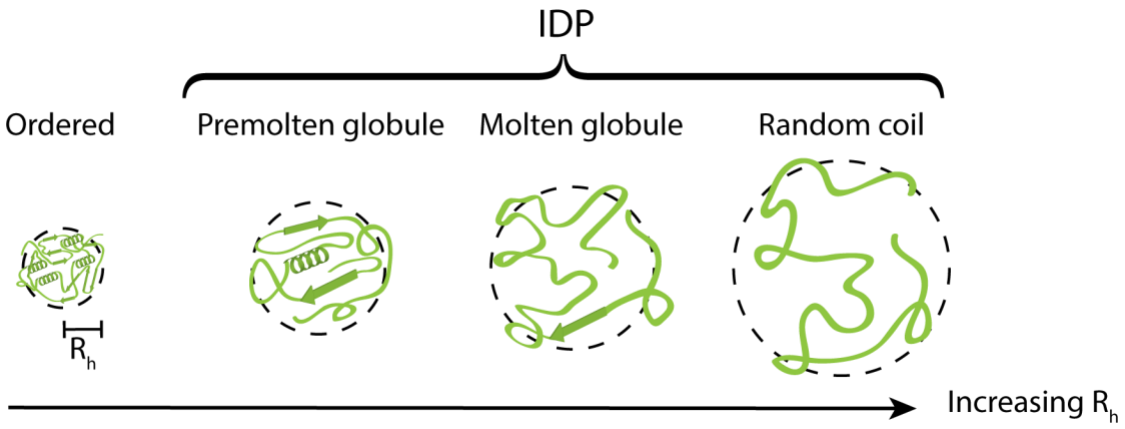

Figure 1-1. Intrinsically disordered proteins are not a homogeneous structural class. Conformations exist on a continuum of disorder. IDPs can exist as either premolten globules, molten globules, or random coils, ranging in size from more compact with some secondary structure to fully extended, respectively. As disorder increases, so does radius of gyration (R_g) and hydrodynamic radius (R_h).

proteins that still retain significant secondary structure.[8] Intrinsically disordered proteins, depending on the content of secondary structure, can be described as either premolten globules, molten globules or random-coil-like conformations (Figure 1-1).[6]

Differences between these states can be clarified by comparing protein molar mass to a protein's size. The two most commonly used measures of protein size are hydrodynamic (or Stokes) radius, R_h, and radius of gyration, R_g.[9-10] A molecule's hydrodynamic radius represents the radius of a sphere that would diffuse at the same rate as the molecule under consideration.[9] Radius of gyration, alternatively, is based on the geometry of the molecule and is the mean squared distance of each point on the object from its center of gravity.[10-11] For proteins that deviate from the traditional globular structure, such as IDPs, R_g tends to be larger than R_h because the molecule is in a more extended conformation.

Because of this continuum of disorder, the definition of an IDP is ambiguous, yet analysis of known IDPs and their amino acid sequences revealed typical characteristics. By comparing IDP amino acid sequences with those for structured proteins, IDPs were found to be deficient in Ile, Leu, Val, Trp, Tyr, Phe, Cy and Asn, which have been termed 'order promoting amino acids'.[4-5, 1112] These same proteins are enriched in Ala, Arg, Gly, Gln, Ser, Glu, Lys and Pro, so-called 'disorder promoting amino acids'.[4-5, 1112] IDPs

contain a high net charge and low overall hydrophobicity, leading to a less compact structure and a larger hydrodynamic radius.[6-7, 13] IDPs have a low content of secondary structure and have a high degree of flexibility, yet can adopt a relatively rigid conformation upon binding of a ligand.[7, 14]

1.1.1 Brief overview of techniques used to characterize IDPs

Any secondary structure that exists in IDPs is typically transient and difficult to characterize.[14] Traditional methods of characterizing the structure of proteins, such as X-ray crystallography, nuclear magnetic resonance (NMR) spectroscopy, and circular dichroism (CD) are not ideal for capturing the flexibility and solution-phase dynamics of the protein; these methods either rely on a static structure, produce dramatic signal overlap, or only confirm that the protein is disordered, respectively.[3, 15-17] While CD can be used to confirm that fluorescently labeled proteins still have a random coil,[18] synchrotron radiation is needed to provide better discrimination of structures in the far-UV wavelength range, which has been used to study conformations of collapsed unfolded molecules.[19-20]

Signal overlap can be overcome by using solid-state NMR techniques to remove the rapid interconversion of structures, but at the cost of understanding those dynamics.[14] Certain NMR techniques however, such as paramagnetic relaxation enhancement (PRE) have been successful in ascertaining long-range contacts in ensembles of IDPs,[6, 8, 14] while pulse-field gradient (PFG) NMR enables measurement of the hydrodynamic radius which can imply long-range contacts.[14] Residual dipolar couplings (RDC) are sensitive to weak alignment of the polypeptide chain and are sensitive to local secondary structure.[6, 14] Using a variety of NMR methods and model development can lead to detailed studies of the conformational heterogeneity of IDPs.[8, 21] A great complementary technique to NMR is small-angle X-ray scattering (SAXS).[6] SAXS provides low resolution macromolecular shapes of intermediate conformations, is sensitive to flexibility of solution-phase proteins, and can be used to determine the radius of gyration.[6, 14-15, 22-23]

Advances in cryogenic electron microscopy (cryo-EM) since 2013 have revolutionized the field of structural characterization of IDPs.[15] Both hardware and software developments have pushed the boundaries of cyro-EM to smaller scale proteins. Direct electron detectors and new image processing techniques have made available the characterization of 100 – 150 kDa enzymes with resolution <2 Å.[15] Cryo-EM relies on flash-freezing samples, rather than crystallizing them, so that the sample is preserved in a native-like state. This flash-freezing process also allows stabilization of transient states without allowing water time to crystallize, allowing characterization of intermediate conformations.[15, 24] Taken together with SAXS and NMR, cryo-EM becomes another tool in the search for IDP structural characterization.[25]

Single-molecule techniques for studying protein disorder have matured and provided a new dimension for visualizing the conformations that are adopted by individual proteins.[26] These techniques, including single-molecule Förster resonance energy transfer (smFRET) and fluorescence correlation spectroscopy, have revealed heterogeneity obscured by the traditional ensemble averaging techniques.[19, 26-30] These techniques and their applications will be covered in more detail later as we discuss the state of characterization of tau protein.

1.2 Tau Protein and Alzheimer's Disease Etiology

1.2.1 Primary structure and function of tau protein

Tau protein is an intrinsically disordered protein (IDP)[31-32] that was first identified in 1975 from tubulin isolated from porcine brain.[33] There are six isoforms of tau protein ranging from 352 to 441 amino acids that are regulated by alternative splicing; isoforms contain either zero, one or two N-terminal inserts (i.e. 0N, 1N or 2N) and either three or four C-terminal repeats (i.e. 3R or 4R).[34] The isoelectric point for the six isoforms ranges from 6.5 to 6.9.[35]

Tau's importance to the central nervous system is characterized by regulation[36] and a stabilization[37] of microtubules.[36, 38-39] Microtubules are hollow cylinders of polymerized tubulin that maintain the shape

and structure of neurons while providing an internal highway for intracellular transport of cargo by motor proteins moving along the axon.[2] Tau weakly binds to microtubules[40] with low micromolar affinity[40-41] and provides a flexible scaffold for tubulin polymerization.[31] Tau's assistance in transportation of nutrients, neurotransmitters and organelles along axons is necessary for neuroplasticity.[35]

Tau protein can be divided into different domains based on how it interacts with molecules or its primary sequence (Figure 1-2): the N-terminal end projects outward from the microtubule while the C-terminal end binds to the microtubules.[39, 42] The N-terminal domain is highly charged and, while it does not bind strongly to microtubules ($K_d \geq 10^3$ μM) ,[39, 43] it is considered to be responsible for regulating the spacing between microtubules by adding to the repulsion.[33, 39, 44-45] Others suggest that larger microtubule associated proteins are responsible for regulating this spacing.[46] The 29 amino acid N-terminal inserts have no significant effect on microtubule binding.[44] The region from 150 – 240 is characterized by a high density of prolines.[39] These prolines, and specifically a seven amino acid sequence between K215 and R221, are responsible for a 10-fold strengthening of the microtubule-binding affinity in 3R and 4R tau and supports microtubule bundling.[39, 44] A repeat region that contains three or four imperfect repeats of 31 or 32 residues is known as the microtubule-binding region (MTBR) and constitutes the largest portion of the assembly domain.[39] Acrylodan fluorescence emission spectra confirm that these repeats undergo a transition from disordered to helical upon binding to tubulin.[31] The basic residues contained in the proline rich and repeat

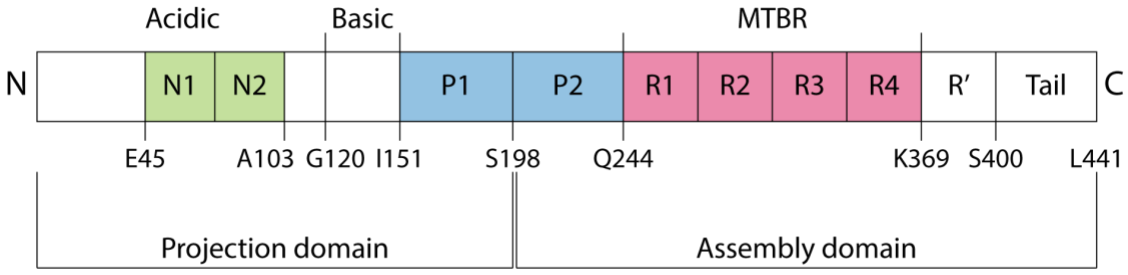

Figure 1-2. Diagram of htau40 (2N4R). Tau protein is divided into two domains: the projection domain responsible for regulating spacing of microtubules and the assembly domain that binds to microtubules. P1 and P2 are rich in prolines. R1 – R4 are microtubule binding repeats. R' is a region weakly homologous to the repeat region. The microtubule binding domain (MTBR) has strong affinity for microtubules.

regions can compensate for the negative charge of the microtubules, allowing them to approach one another and elongate and stabilize.[39] While these regions all have different functionalities, they also have different responses to environmental conditions — a response that may be necessary for increased functional diversity.[47]

1.2.2 Tau linked to Alzheimer's disease pathology

While tau protein plays an essential role in enhancing the stability and organization of microtubules, its aggregation has been linked to Alzheimer's disease[48-49] and other neurodegenerative diseases, known generally as tauopathies.[50] These diseases are characterized by pathological aggregation of tau into paired helical[51-52] or straight filaments,[48-49] which are formed after tau has adopted a β-sheet structure.[53] While some mutations of tau have been linked to familial neurodegenerative diseases,[54-55] other cases of Alzheimer's disease do not have a definitive origin. And while filamentous deposits of tau are a hallmark of the disease, some experiments suggest that these tangles are protective measures that sequester hyperphosphorylated tau[56] and it is actually the soluble precursor oligomers that are the toxic species.[57-58]

There are 85 residues on htau40 that are susceptible to phosphorylation,[59] and abnormal phosphorylation has been associated with Alzheimer's disease.[60] Hyperphosphorylation of tau results in a loss of proper function[61] by disrupting the normal equilibrium of bound and unbound tau protein to microtubules.[48, 56] The ratio of bound to unbound tau is important for cellular transport, so an imbalance affects transport along axons and maintenance of neuron synapses.[56, 62] Hyperphosphorylation also results in a conformational change[32, 63] where electrostatic attraction causes tau filaments to become more dense and compact in certain regions.[59] Molecular dynamics simulations have also shown that phosphorylation exposes the repeat region to more solvent.[59]

Phosphorylated tau monomer aggregates into paired helical filaments then into neurofibrillary tangles characteristic of tauopathies.[64] Paired helical filaments of tau contain all six naturally occurring isoforms[65-66] and form from parallel stacking of tau[67] that has adopted a β-sheet structure.[68] Filaments have a radius of 160 – 180 Å[59] with a helical repeat of about 800 Å.[64] NMR studies of these aggregates confirm that the middle of the protein has immobile residues that are unable to be detected.[69] Cryo-EM measurements show that there is a common core structure consisting of repeats R3 – R4[49] and that the same hexapeptide motif that initiates paired helical filament assembly[52] also forms the ordered core of the filaments.[49] Studies have shown that the conformation of monomers determines their seeding competency,[70] which subsequently may determine disease pathology.[71-72] Because the pathology of these diseases can be determined from the monomer stage, it becomes important to understand the conformational diversity of monomers and how single monomers begin to form aggregates.

1.2.3 Current understanding of tau structure and structural flexibility

While tau protein is characterized as an IDP — and indeed has a high degree of flexibility in solution — it is not completely devoid of secondary structure motifs and adopts many conformations in solution.[21, 67, 73-75] Using a combination of techniques, both ensemble-averaged and single-molecule, has provided a glimpse of the conformational heterogeneity experienced by the protein. Some of these studies will be discussed to give an overview of the current state of characterization of tau protein.

Early studies of tau protein demonstrated the random coil nature of tau protein via CD,[76-78] x-ray scattering[77] and NMR spectroscopy.[79] These early studies found a negligible amount of α-helix and β-sheet structure[76] due to the low ellipticity of CD spectra around 200 nm characteristic of disordered proteins,[80] and high flexibility when unbound from microtubules.[79] The radius of gyration was determined to be 6.5 nm,[21, 23, 81] and the hydrodynamic radius was determined to be 5.4 nm.[21]

Ensemble Förster resonance energy transfer (FRET) measurements describe the conformation of tau as a "paperclip", where the N- and C-termini are folded inward, a structure that does not preclude the high mobility of the backbone (Figure 1-3a).[18] The observed FRET can be altered by denaturation to loosen the conformation[18] or phosphorylation[82] which moderates the compactness by increasing or decreasing intramolecular contacts. Single-molecule FRET (smFRET) measurements, while qualitatively similar to the ensemble measurements, propose an "S-shaped" configuration of tau (Figure 1-3b),[83] a finding corroborated by time-resolved electrospray ionization mass spectrometry with hydrogen/deuterium exchange.[32] Small-angle X-ray scattering (SAXS) studies of the conformation of tau indicate that the repeat domain is extended;[23] NMR and smFRET experiments have demonstrated that the conformation of this same region is altered and compacted upon aggregation.[83-84] NMR studies, coupled with computation, have been used to characterize the highly dynamic conformations of tau protein.[21] These studies have confirmed the findings of others — namely the extended structure under normal conditions, weak intramolecular contacts, and propensity for β-sheet formation in the repeat region — but have also computationally derived a collection of at least 30 conformations.[21]

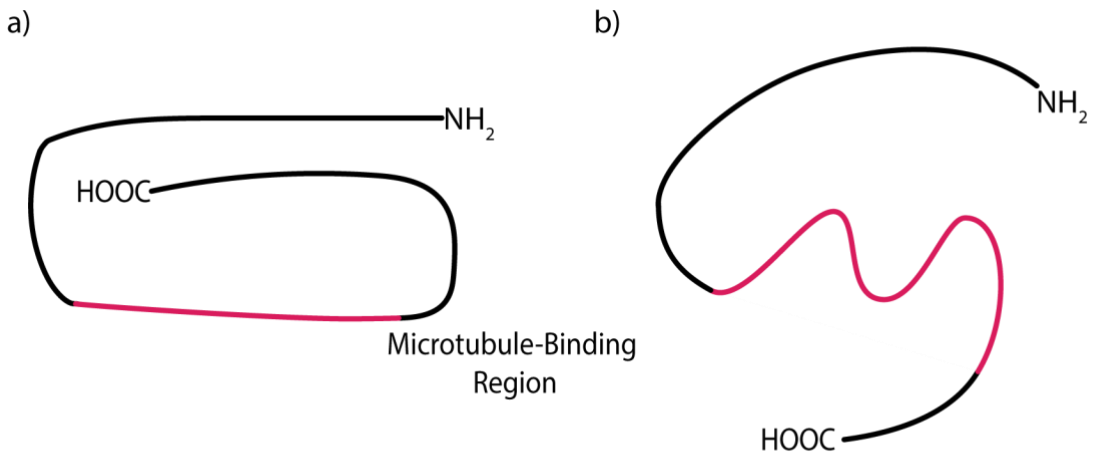

Figure 1-3. Proposed conformations of tau protein. (a) Paperclip structure determined by ensemble FRET measurements and (b) S-shaped structure determined by smFRET.

Further work is still required to fully characterize tau protein and its conformational heterogeneity. The conformations of transiently populated intermediates, the type that are obscured in ensemble measurements, may hold the key to determining subsequent toxic states of tau protein.[13]

1.3 Traditional Single-Molecule Techniques

Single-molecule fluorescence measurements provide a wealth of information about the heterogeneity of a sample that can be obscured in traditional ensemble-averaged methods. Solution-phase single-molecule measurements of biomolecules have reported on different conformations and assemblies,[83, 85-87] transition pathways[88-89] and conversion kinetics.[90-92] For single-molecule fluorescence measurements in solution, there are two major paradigms for the measurement: free diffusion and surface immobilization.

In studies of freely diffusing molecules, a laser is typically tightly focused into a solution containing fluorescently-labeled molecules at a low enough concentration such that most of the time there is no molecule being excited, and thus no signal. This low concentration (on the order of pM) is needed to ensure that the likelihood of observing more than one molecule is low. The molecules that are in the solution randomly diffuse via Brownian motion and will occasionally diffuse into the excitation volume, producing a spike in recorded fluorescence intensity. The amount of time the molecule resides in the excitation volume — and thus the length of time the molecule and its properties can be observed — depends on the molecule's diffusion coefficient, which is related to its size via the Stokes-Einstein equation:

$$D = \frac{k_B T}{6\pi\eta R_h} \qquad \text{(equation 1-1)}$$

where k_B is the Boltzmann constant, T is the temperature in Kelvin, η is the viscosity of the solvent and R_h is the hydrodynamic radius. This type of measurement is typically restricted by millisecond dwell times and is thus not suitable for observing processes that happen on the second timescale.

Immobilization of a protein to a surface can be achieved via many methods such as using a biotinylated surface and streptavidin, encapsulating biomolecules in vesicles and tethering the vesicle to a supported lipid bilayer, or relying on electrostatic interactions.[93] These methods provide prolonged observation of a molecule in an excited volume, with the length of observation limited only by the photobleaching time, at which point the molecule loses the ability to emit light. This method is widely used to study kinetics and structural changes of DNA, RNA and other biomolecules.[93-95] But immobilization introduces the question of whether or not the immobilization alters the function or conformation of the constrained biomolecule.[96-98] This may be a greater problem when studying IDPs since there is no well-defined structure and therefore artifacts are harder to discern.

These traditional methods leave one with the decision between limited signal but unperturbed motion or prolonged signal and possible alteration of conformations. Methods such as optical tweezers have been developed to overcome the limitations of this paradigm by using intense radiation and optical gradient forces to trap micrometer-sized objects.[99] Heat produced from the radiation, however, can cause damage to single molecules,[100] and the restoring forces needed for smaller objects makes trapping nanometer-sized objects increasingly difficult. The anti-Brownian electrokinetic (ABEL) trap, developed in the Moerner lab at Stanford University, is an excellent alternative that relies not on light gradient forces, but rather tracking a single molecule and applying electrokinetic feedback voltages to re-center a molecule of interest.[101-102]

1.4 Anti-Brownian Electrokinetic (ABEL) Trap

The ABEL trap relies on tracking the location of a single fluorescent molecule, calculating its Brownian motion from a defined center position, and applying an electrokinetic force to re-center the molecule in the excitation volume. With these calculations being performed at 40 kHz, the molecule becomes effectively trapped in the excitation volume and observation time is only limited by photobleaching. This system has been used previously to study the diffusion and mobility of multi-subunit proteins,[103] observe redox events for single enzymes,[104] detect shape fluctuations of DNA,[105] and even to study the photophysics of single fluorophores in solution.[106] In order to successfully trap a single molecule, a sample holder that will allow for manipulation of single molecules, a mechanism for tracking the position of the molecule, and a method for counteracting the Brownian diffusion of the molecule are required.

1.4.1 Microfluidic device

A microfluidic device is made from a quartz wafer using standard microfabrication techniques (Figure 2-11).[107] The device is then bonded to a fused silica coverslip to create a sample chamber (Figure 1-4a). The center of this microfluidic trap is approximately 10 µm x 10 µm x 1 µm. Four electrodes are placed in the x- and y- directions for applying electrokinetic voltages, and in the z-direction molecules are confined by the depth of the trap. The electrodes produce an electric field in solution that will be used for trapping molecules.

1.4.2 Position tracking

The first requirement for tracking a single molecule is to have some reporter to follow, in this case a fluorophore. ATTO dyes are chosen for their high stability at the high photon count rate required by the

system.[98] A pattern of 32 spots is traced in the center of the trapping region by a single laser deflected using acousto-optic beam deflectors, a pattern referred to as the "knight's tour" (Figure 1-4b).[103, 108] As this pattern proceeds, the laser will overlap in time and space with a fluorescently-labeled molecule, excite it, and a photon will be detected (Figure 1-4c). The position of the laser at the time the photon is detected is

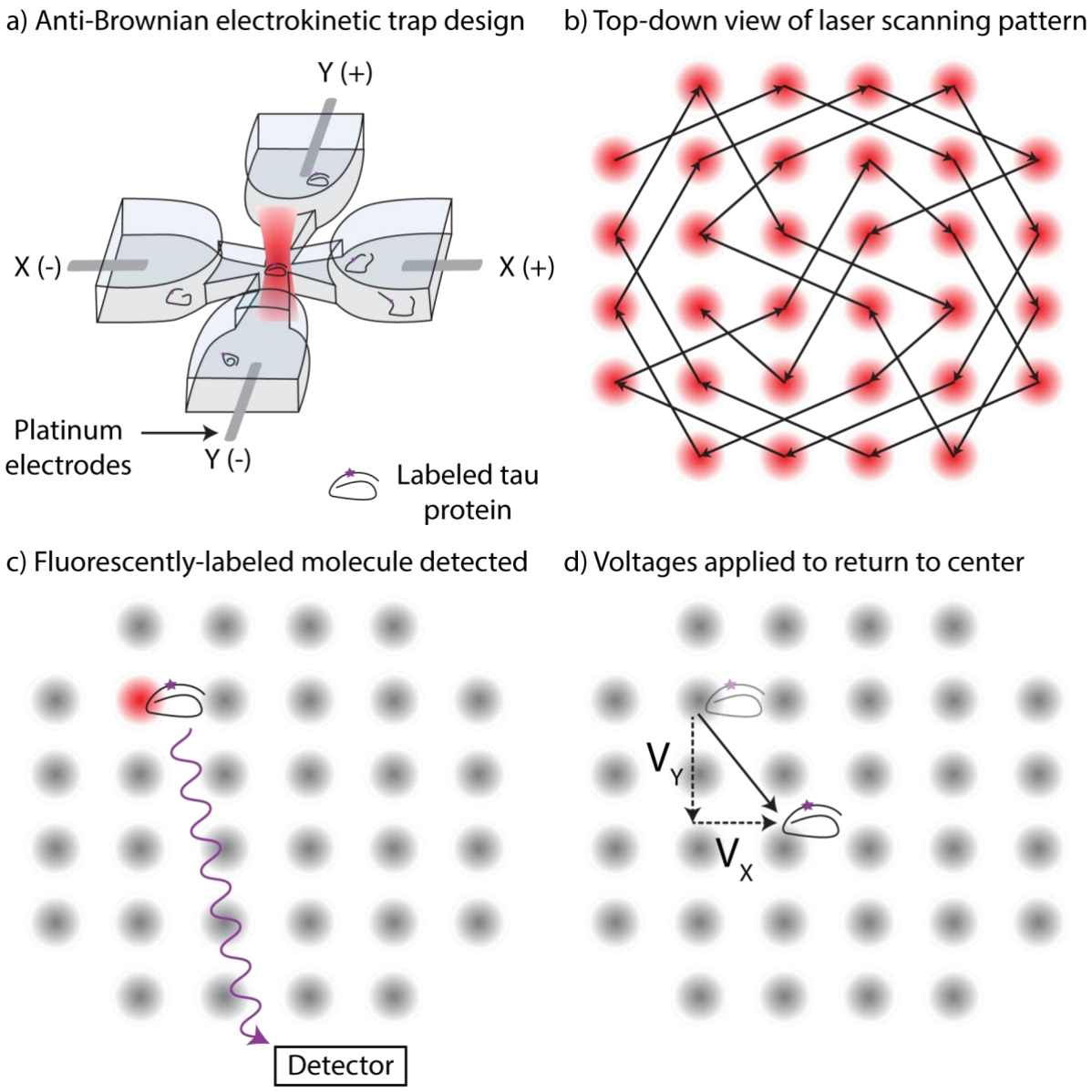

Figure 1-4. Anti-Brownian electrokinetic (ABEL) trap. (a) Voltages applied to the platinum electrodes induce an electrokinetic force in the microfluidic device to return the protein back to the center. (b) A top-down view of the trapping region exposes a pattern that a single laser spot scans over, as indicated by the solid line. The laser repeats the pattern every 25 µs. The molecule is confined in the z-direction by the height of the trapping region, 1 µm. (c) A photon is detected when a fluorescently-labeled molecule overlaps with the excitation beam. (d) X and Y feedback voltages are applied to restore the molecule's position to the center.

taken as the raw position measurement, and in the simplest incarnation of the trap, the raw position is taken as the actual position and feedback voltages are calculated to return the molecule to the center (Figure 1-4d). These voltages are applied every 25 µs.

1.4.2.1 *Kalman filter*

While the position of the laser at the photon detection event gives a rough estimate of the position of the molecule of interest, it does not give the best guess for the position of the molecule. In order to improve the position tracking of the molecule, a Kalman filter is implemented and calculates the optimal estimation of the object's position.

The Kalman filter is named for R.E. Kalman, who published the mathematical equations to efficiently estimate the state of a process in 1960.[109] Since then, it has been extensively researched and applied, even to problems of assisted navigation.[109] The Kalman filter uses recursive formulas to predict the position of an object at a time, *k*, by incorporating information about the location of the object at time *k-1*,

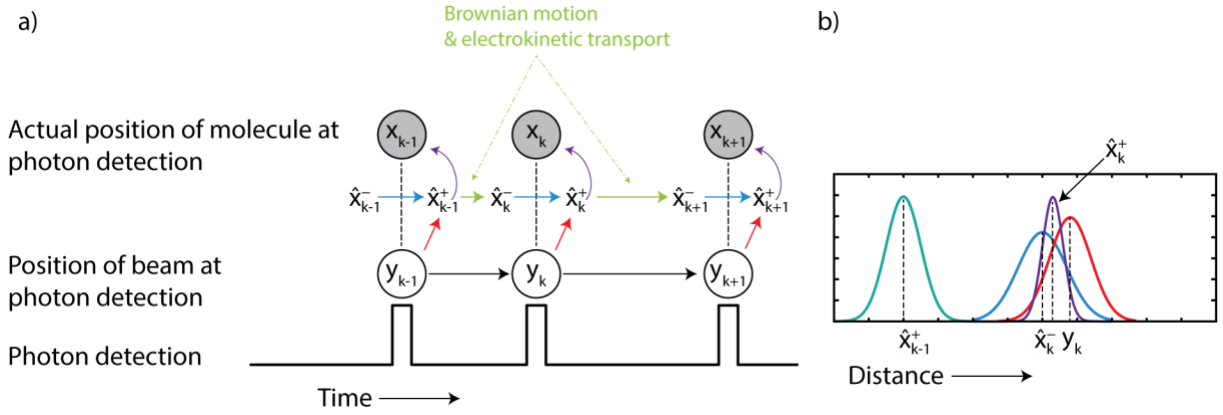

Figure 1-5. Kalman filter representation. (a) A photon is detected when the laser is at position y_k. The best guess of the position of the molecule immediately after detection, $\hat{x}_k^+$, is found by incorporating the prior estimate from the current event, $\hat{x}_k^-$ (blue arrow), with the measurement at y_k (red arrow). $\hat{x}_k^-$ is estimated based on the posterior estimate from the previous event, $\hat{x}_{k-1}^+$, and the electrokinetic translation between events (green arrow). This prediction is used to infer x_k (purple arrow), which is otherwise hidden. (b) The estimated positions are represented as Gaussian curves with some variance. The measured value, y_k, has uncertainty in the measurement that contributes to the variance. The best guess for the position of the molecule at a particular point uses information from the measurement and the prior estimate, $\hat{x}_k^-$, of the molecule's location. The prior estimate of the location depends on the posterior estimate of the previous location. See text for more details.

estimates of Brownian motion and electrokinetic transport since the previous measurement, as well as the newest measurement, y_k (Figure 1-5).

Photons are detected stochastically during operation of the ABEL trap, as indicated by the irregular intervals between detection events in Figure 1-5a. When a photon is detected, the position of the laser at that time is recorded, y_k. The chance of detecting a molecule at position y_k is related to the shape of the laser spot, and thus the position of the laser alone does not give a definitive position of the molecule — since it could be anywhere within the excited volume — but does contribute some information about the location of the molecule (Figure 1-5a, red arrows). An estimate can be made prior to detection of a photon, indicated by $\hat{x}_k^-$ (superscript "–" indicates prior). This estimate is made by using the posterior estimate from the previous time step, $\hat{x}_{k-1}^+$ (superscript "+" indicates posterior), combined with information about the electrokinetic translation of the molecule (Figure 1-5a, green arrows). This estimate is also used to estimate the location of the molecule (Figure 1-5a, blue arrows). Together, the location of the laser spot, the knowledge of the previous location of the molecule and the prediction of electrokinetic translation applied since the last measurement can provide a best guess estimate for the current location of the molecule, x_k.[102]

An alternative understanding of the Kalman filter can be accomplished by imagining a molecule moving from left to right across the x axis in Figure 1-5b. The position of the object at $\hat{x}_{k-1}^+$ is represented by the mean value of the teal curve, represented as a Gaussian with an uncertainty in the estimation represented by the width of the curve. At the next time point, the object will be predicted to be at $\hat{x}_k^-$, with some uncertainty due to the estimation of its motion (Figure 1-5b, blue curve). A measurement of y_k will provide another estimation for the location of the molecule at time k (Figure 1-5b, red curve). Combined, the blue and red curves will provide a more accurate estimation of the molecule immediately after the measurement, $\hat{x}_k^+$ (Figure 1-5b, purple curve).[110]

This recursive process is repeated at each time step, combining estimations of prior states with estimates of current states to continually refine the predicted position. For a complete mathematical derivation of the Kalman filter as it pertains to the ABEL trap, please see Quan Wang's dissertation (Chapter 2).[102]

1.4.3 Electrokinetic feedback

When a voltage is applied to the microfluidic trap, a flow develops in the solution and provides the feedback to compensate for the Brownian motion of the molecule. The electrokinetic phenomenon is a combination of electrophoresis and electroosmosis. Both can contribute to the movement of the molecule in the trap. Electrophoresis is the movement of a charged particle in an externally applied electric field, and electroosmosis describes the movement of charges in a liquid under the influence of an external electric

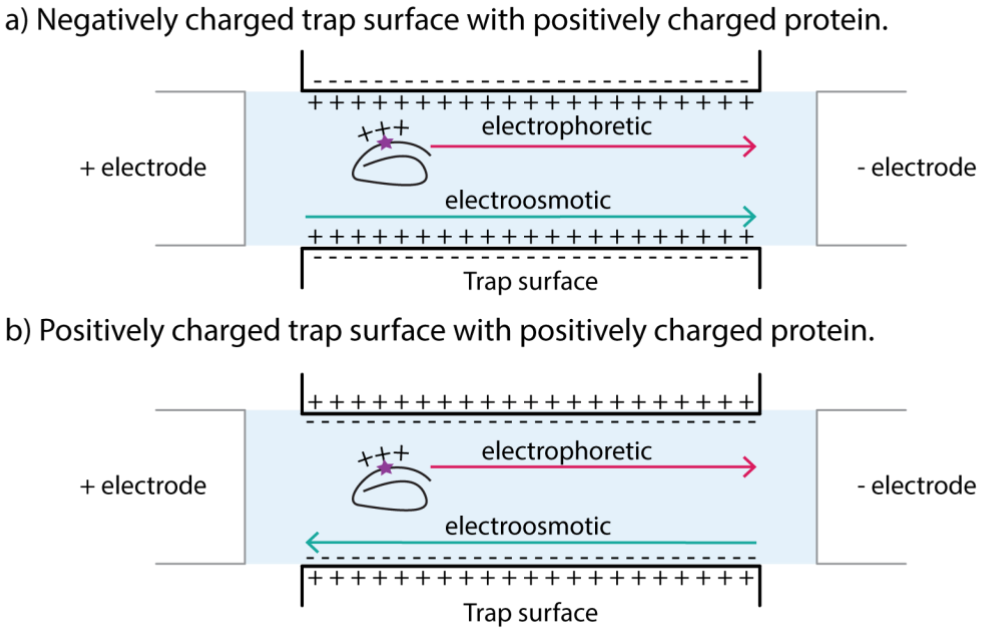

Figure 1-6. Trapping forces in the ABEL trap. The surface of the trap can be either (a) negatively or (b) positively charged, leading to a buildup of ions in solution along the trap surface. (a) Trapping forces are reinforced for a positively charged protein in a trap with a negatively charged surface. (b) Trapping forces counteract one another in the scenario with a positively charged protein and a positively charged trapping surface.

field (Figure 1-6). These two forces can either reinforce or counteract one another, as shown in Figure 1-6. For the samples analyzed here, electrophoretic flow is a minor contributor to the feedback since improving surface coverage of negative charges (such as in Figure 1-6a) improves trapping by improving electroosmotic flow. Alternatively, switching the polarity of the surface (as shown in Figure 1-6b) leads to worse trap performance. The use of electroosmotic flow has a particular advantage for trapping neutral objects, since no charge is required to affect the molecule's position.

1.4.3.1 *Surface passivation using polyelectrolyte layers*

Nonspecific adsorption to the fused silica surface of the microfluidic can be an issue that is relatively easily overcome by the use of polyelectrolyte layers (PELs). Polyethyleneimine (PEI) and polyacrylic acid (PAA) are used as positive and negative polymers, respectively.[111] The positively charged polymer is injected into the cell and allowed to incubate for 10 min before removal and incubation with the next, negatively charged, layer.[104] The process is repeated to improve the efficacy, presumably by providing more complete coverage of the trap surface. In this way, the electroosmotic flow is strengthened by the high surface density of charges.

1.5 Fluorescence Anisotropy

Once a molecule is trapped in the ABEL trap, it is desirable to extract as much information from the fluorescence as possible. By exciting with polarized light and detecting the polarization of the emission, anisotropy can be determined. Below, anisotropy is discussed for an intuitive understanding. For a complete mathematical derivation of anisotropy, see Principles of Fluorescence Spectroscopy by Joseph Lakowicz.[112]

1.5.1 ***Theory for steady-state anisotropy***

Fluorescence anisotropy (*r*) is an important measurement in biochemical research since it can be used to characterize motions in solution. If a randomly selected sample is excited with continuous, polarized light, the emission will likely also be polarized. The extent that this emission is polarized is described in terms of its anisotropy. Chromophores have transition moments (excitation and emission) that are oriented along specific molecular axes. In a homogeneous sample of fluorophores with excitation transition moments randomly oriented, those with the transition moment oriented parallel to the excitation polarization will preferentially absorb. This leads to an excited state population of partially oriented fluorophores (Figure 1-7). These dipoles, freely moving and rotating, will change the orientation of their dipole during the excited state lifetime. Upon emitting a photon, the dipole will have rotated by some measurable angle from its excitation position. Measuring the intensity of emission light polarized parallel ($I_{\parallel}$) and perpendicular ($I_{\perp}$) to the excitation light, will provide a measure of the anisotropy (*r*) (equation 1-2).[112] If the dipoles are able to rotate quickly, as in Figure 1-7a, more complete depolarization

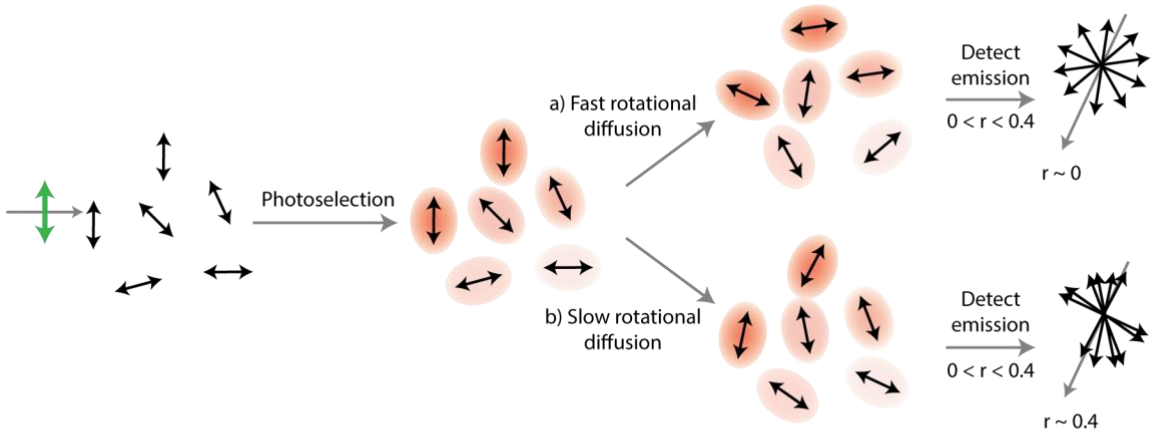

Figure 1-7. Principles of anisotropy measurements. (a) Fast rotational diffusion in solution leads to depolarization of excitation light. The depolarized emission is recorded as a low anisotropy value (near 0 for complete depolarization). (b) Slow rotational diffusion in solution will lead to emission that is more representative of the excitation polarization, leading to a higher value for anisotropy (approaching 0.4).

of the excitation light will occur and the anisotropy will approach zero. In the case where rotational diffusion is slow, due to size of the molecule or viscosity of the solvent, for example, the anisotropy will approach the upper limit of 0.4 (Figure 1-7b). While an anisotropy of r = 1 is possible for a single immobilized fluorophore oriented along the z-axis with colinear transitions, the maximum of r = 0.4 is a result of the photoselection of a collection of fluorophores and the probability of absorption.

$$r = \frac{I_{||} - G \times I_{\perp}}{I_{||} + 2 \times G \times I_{\perp}} \qquad \text{(equation 1-2)}$$

*1.5.2 **Time-resolved measurements***

While steady-state anisotropy can provide information about the extent of molecular tumbling, time-resolved measurements can elucidate the origins of the decay of anisotropy. Ideally, time-resolved measurements would rely on a single pulse of excitation followed by a measurement of the resulting fluorescence. Unfortunately, it is not possible to retrieve accurate information to characterize the fluorescence decay of a sample from a single excitation-emission cycle. Therefore, it becomes necessary to periodically excite the sample with a pulsed laser and collect data over many excitation-emission cycles. Time-correlated single photon counting (TCSPC) is used to precisely tag the arrival of the photons with respect to each excitation pulse (Figure 1-8a).[1] The time between the laser pulse exciting the sample and the detected photon is recorded and binned according to the Δt values. These Δt values are then used in a histogram that will represent the fluorescence decay of the sample (Figure 1-8b).

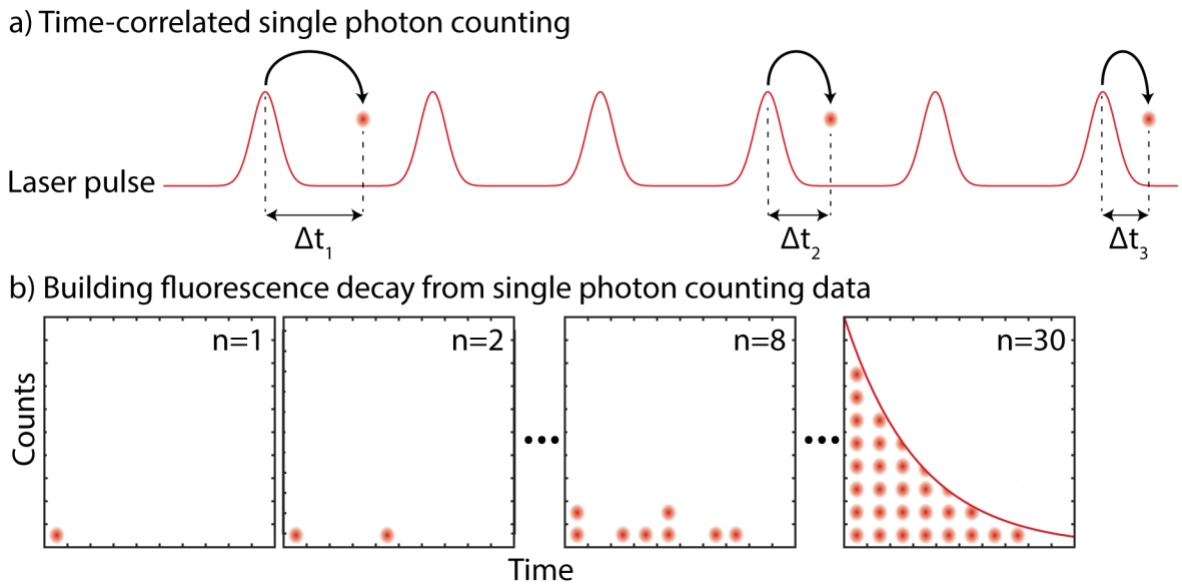

Figure 1-8. Time-correlated single photon counting. (a) A pulsed laser periodically excites a fluorescent sample and the emitted photons are time-tagged relative to the excitation pulse. (b) The time-tagged events are used to reconstruct a fluorescence decay histogram by sorting fluorescent photons into bins based upon the Δt. Figure inspired by PicoQuant's guide to TCSPC.[1]

It is worth noting that pile-up error is a potential concern when working with highly emissive samples, such as the perovskites studied in Chapter 4. Pile-up error occurs when the photon count rate far exceeds the excitation repetition rate so that for every excitation pulse on average >1 photon is emitted (Figure 1-9). This becomes a problem because there is a "dead time" associated with the avalanche photodiode (APD), during which time no photon can be recorded. This results in an overexpression of early-time photons since the first photon emitted is recorded, thus artificially increasing the decay rate of the measurement. For this reason, it is advisable to keep the detection count rate at 1 – 5 % of the excitation rate.[1] Pile-up error can also manifest as an extra "bump" in the decay of data taken at slower repetition rates due to the APD coming back online and starting to detect photons again (see Figure 4-15 for an example).

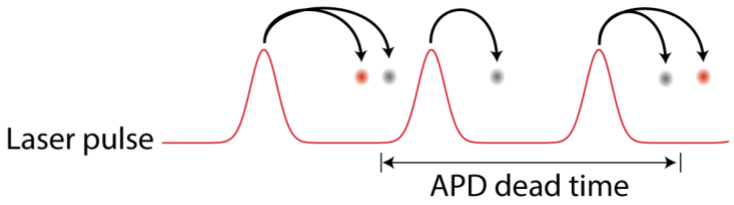

Figure 1-9. Pile-up error caused by photon emission rate exceeding excitation rate. Red photons represent photons that are recorded, while gray photons are missed because they are emitted during the dead time of the avalanche photodiode (APD). Figure based on PicoQuant's guide to TCSPC.[1]

1.5.3 Time-resolved fluorescence anisotropy

From time-resolved fluorescence data, two important rates can be determined: fluorescence lifetime and rotational correlation time. While the intensity and anisotropy both decay exponentially, they are not linked. The lifetime is a property of the fluorophore, and the rotational correlation time depends on the size, shape and flexibility of the molecule.[112] The rotational correlation time of a molecule is defined as the time at which the initial anisotropy has decayed to 1/*e* of the original value. While spherical molecules can have simple, single rotational correlation time decays, most biomolecules have more complex decays due to their non-spherical nature and the flexibility within the molecule.[112]

If a fluorophore is excited with a pulse of vertically polarized light, it will selectively excite those molecules oriented parallel to the excitation pulse, causing a higher signal in the parallel emission channel

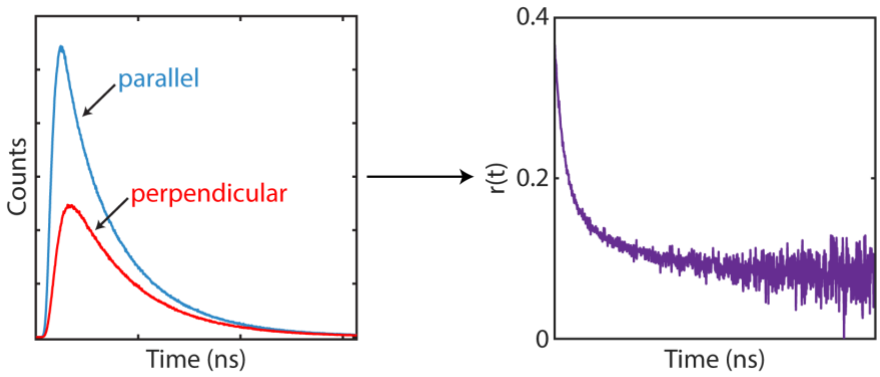

Figure 1-10. Example fluorescence and anisotropy decays.

initially (Figure 1-10, left, blue curve). The initial decay in the parallel channel is faster than the perpendicular, because the decay in the parallel channel is a combination of fluorescence intensity decay and rotation of molecules out of the parallel orientation. The perpendicular channel, on the other hand, decays slower at first because it is populated from these rotating molecules. From these intensity decays, an anisotropy decay (Figure 1-10, right) can be generated by calculating:

$$r(t) = \frac{I_{\parallel}(t) - I_{\perp}(t)}{I_{\parallel}(t) + 2I_{\perp}(t)} \quad \text{(equation 1-3)}$$

In order to fit the component intensity decays, the intensity and anisotropy decay must both be accounted for according to:

$$I_{||}(t) = \frac{1}{3} I(t)[1 + 2r(t)] \quad \text{(equation 1-4)}$$

$$I_{\perp}(t) = \frac{1}{3} I(t)[1 - r(t)] \quad \text{(equation 1-5)}$$

where *r(t)* is

$$r(t) = \sum_j r_{0j} \exp\left(-\frac{t}{\theta_j}\right) \quad \text{(equation 1-6)}$$

and r_{0j} are the amplitude of each rotational correlation time experienced by the molecule. *r(t)* can also be described by a multi-exponential decay describing wobbling-in-a-cone or cone-in-a-cone behavior with one or two local motions,[113-114]

$$\frac{r(t)}{r_0} = (1 - S_F^2) e^{-t\left[\frac{1}{\phi_f} + \frac{1}{\phi_s}\right]} + S_F^2 e^{-\frac{t}{\phi_s}} \quad \text{(equation 1-7)}$$

for a biexponential anisotropy decay or

$$\frac{r(t)}{r_0} \cong (1 - S_F^2) e^{-\frac{t}{\phi_f}} + S_F^2 (1 - S_I^2) e^{-\frac{t}{\phi_i}} + S_I^2 S_F^2 e^{-\frac{t}{\phi_s}} \quad \text{(equation 1-8)}$$

for a triexponential anisotropy decay, where S_F^2 and S_I^2 are the squared order parameters and indicate the extent to which the motion is restricted. Assuming reorientation of the dye transition dipole is confined within a cone of half-angle, θ_c, then θ_c can be determined by:[113, 115]

$$\frac{r_\infty}{r_0} = \mathrm{S}^2 = \left[\frac{1}{2}\cos\theta_c\,(1+\cos\theta_c)\right]^2 \qquad \text{(equation 1-9)}$$

where r_∞ is the residual anisotropy.

Time-resolved anisotropy will be used later in Chapter 2 to detail the timescales of motion present in tau protein and microbial transglutaminase (MTG) protein. Current work is being done by Alexander Foote to apply the same time-resolved anisotropy measurements discussed in this dissertation to single-molecules trapped in the ABEL trap, providing a more detailed picture of the heterogeneity of motions experienced by the protein.

1.6 Outline

I have worked on research that covers two pretty unrelated topics: conformational heterogeneity of tau protein and recombination kinetics of methylammonium lead iodide ($MAPbI_3$) perovskites. These projects overlap only in the technique used — time-resolved single photon counting. First, I will detail the work done with the ABEL trap to understand the conformations of tau protein. I will describe how the ABEL trap facilitates study of individual proteins by prolonging the observation time so that the resulting histograms may be more representative of molecular populations, rather than artifacts of limited photon statistics. I will then detail the preliminary studies I have performed to determine the aggregation competency of the fluorophore-labeled tau mutants, a characteristic that will be important in future studies that involve studying aggregation of tau protein from the single-molecule level. I end by describing a global analysis of the photophysics of methylammonium lead iodide ($MAPbI_3$) perovskite that lead us to employ geminate pathways as an important recombination mechanism.

1.7 References

1. Wahl, M., *Time-Correlated Single Photon Counting*; PicoQuant GmbH: Berlin, Germany, 2014, p 14.

2. Berg, J. M.; Stryer, L.; Tymoczko, J. L., *Biochemistry*; W.H. Freeman: New York, 2002.

3. Uversky, V. N., Introduction to intrinsically disordered proteins (IDPs). *Chem. Rev.* **2014**, *114*, 6557-6560.

4. Uversky, V. N., Intrinsically Disordered Proteins and Their Environment: Effects of Strong Denaturants, Temperature, pH, Counter Ions, Membranes, Binding Partners, Osmolytes, and Macromolecular Crowding. *Protein J.* **2009**, *28*, 305-325.

5. Dyson, H. J.; Wright, P. E., Intrinsically unstructured proteins and their functions. *Nat. Rev. Mol. Cell Biol.* **2005**, *6*, 197-208.

6. Habchi, J.; Tompa, P.; Longhi, S.; Uversky, V. N., Introducing protein intrinsic disorder. *Chem. Rev.* **2014**, *114*, 6561-6588.

7. Uversky Vladimir, N., What does it mean to be natively unfolded? *Eur. J. Biochem.* **2003**, *269*, 2-12.

8. Dyson, H. J., Expanding the proteome: disordered and alternatively folded proteins. *Q. Rev. Biophys.* **2011**, *44*, 467-518.

9. Schultz, S. G.; Solomon, A. K., Determination of the Effective Hydrodynamic Radii of Small Molecules by Viscometry. *J. Gen. Physiol.* **1961**, *44*, 1189.

10. Linegar, K. L.; Adeniran, A. E.; Kostko, A. F.; Anisimov, M. A., Hydrodynamic radius of polyethylene glycol in solution obtained by dynamic light scattering. *Colloid J.* **2010**, *72*, 279-281.

11. Jones, R. A. L., *Soft Condensed Matter*; Oxford University Press: Oxford; New York, 2002.

12. Williams, R. M.; Obradovi, Z.; Mathura, V.; Braun, W.; Garner, E. C.; Young, J.; Takayama, S.; Brown, C. J.; Dunker, A. K., The protein non-folding problem: amino acid determinants of intrinsic order and disorder. *Pac. Symp. Biocomput. 2001* **2001**, 89-100.

13. Nath, A.; Rhoades, E., A flash in the pan: dissecting dynamic amyloid intermediates using fluorescence. *FEBS Lett.* **2013**, *587*, 1096-1105.

14. Eliezer, D., Biophysical characterization of intrinsically disordered proteins. *Curr. Opin. Struct. Biol.* **2009**, *19*, 23-30.

15. Palamini, M.; Canciani, A.; Forneris, F., Identifying and Visualizing Macromolecular Flexibility in Structural Biology. *Front. Mol. Biosci.* **2016**, *3*.

16. Greenfield, N. J., Analysis of Circular Dichroism Data. In *Methods Enzymol.*, Academic Press: 2004; Vol. 383, pp 282-317.

17. Kelly, S. M.; Jess, T. J.; Price, N. C., How to study proteins by circular dichroism. *Biochim. Biophys. Acta* **2005**, *1751*, 119-139.

18. Jeganathan, S.; von Bergen, M.; Brutlach, H.; Steinhoff, H. J.; Mandelkow, E., Global hairpin folding of tau in solution. *Biochemistry* **2006**, *45*, 2283-2293.

19. Hoffmann, A.; Kane, A.; Nettels, D.; Hertzog, D. E.; Baumgartel, P.; Lengefeld, J.; Reichardt, G.; Horsley, D. A.; Seckler, R.; Bakajin, O., et al., Mapping protein collapse with single-molecule fluorescence and kinetic synchrotron radiation circular dichroism spectroscopy. *Proc. Natl. Acad. Sci. U. S. A.* **2007**, *104*, 105-110.

20. Miles, A. J.; Wallace, B. A., Synchrotron radiation circular dichroism spectroscopy of proteins and applications in structural and functional genomics. *Chem. Soc. Rev.* **2006**, *35*, 39-51.

21. Mukrasch, M. D.; Bibow, S.; Korukottu, J.; Jeganathan, S.; Biernat, J.; Griesinger, C.; Mandelkow, E.; Zweckstetter, M., Structural polymorphism of 441-residue tau at single residue resolution. *PLoS Biol.* **2009**, *7*, e34.

22. Kachala, M.; Valentini, E.; Svergun, D. I., Application of SAXS for the Structural Characterization of IDPs. In *Intrinsically Disordered Proteins Studied by NMR Spectroscopy*, Felli, I. C.; Pierattelli, R., Eds. Springer International Publishing: Cham, 2015; pp 261-289.

23. Mylonas, E.; Hascher, A.; Bernadó, P.; Blackledge, M.; Mandelkow, E.; Svergun, D. I., Domain Conformation of Tau Protein Studied by Solution Small-Angle X-ray Scattering. *Biochemistry* **2008**, *47*, 10345-10353.

24. Kühlbrandt, W., Cryo-EM enters a new era. *eLife* **2014**, *3*, e03678.

25. Knowles, T. P.; Vendruscolo, M.; Dobson, C. M., The amyloid state and its association with protein misfolding diseases. *Nat. Rev. Mol. Cell Biol.* **2014**, *15*, 384-396.

26. Brucale, M.; Schuler, B.; Samori, B., Single-molecule studies of intrinsically disordered proteins. *Chem. Rev.* **2014**, *114*, 3281-3317.

27. Soranno, A.; Koenig, I.; Borgia, M. B.; Hofmann, H.; Zosel, F.; Nettels, D.; Schuler, B., Single-molecule spectroscopy reveals polymer effects of disordered proteins in crowded environments. *Proc. Natl. Acad. Sci. U. S. A.* **2014**, *111*, 4874-4879.

28. Schuler, B.; Lipman, E. A.; Eaton, W. A., Probing the free-energy surface for protein folding with single-molecule fluorescence spectroscopy. *Nature* **2002**, *419*, 743-747.

29. Soranno, A.; Holla, A.; Dingfelder, F.; Nettels, D.; Makarov, D. E.; Schuler, B., Integrated view of internal friction in unfolded proteins from single-molecule FRET, contact quenching, theory, and simulations. *Proc. Natl. Acad. Sci. U. S. A.* **2017**, *114*, E1833-e1839.

30. Basak, S.; Chattopadhyay, K., Fluorescence correlation spectroscopy study on the effects of the shape and size of a protein on its diffusion inside a crowded environment. *Langmuir* **2013**, *29*, 14709-14717.

31. Li, X. H.; Culver, J. A.; Rhoades, E., Tau Binds to Multiple Tubulin Dimers with Helical Structure. *J. Am. Chem. Soc.* **2015**, *137*, 9218-9221.

32. Zhu, S.; Shala, A.; Bezginov, A.; Sljoka, A.; Audette, G.; Wilson, D. J., Hyperphosphorylation of intrinsically disordered Tau protein induces an amyloidogenic shift in its conformational ensemble. *PLoS One* **2015**, *10*, e0120416.

33. Weingarten, M. D.; Lockwood, A. H.; Hwo, S. Y.; Kirschner, M. W., A protein factor essential for microtubule assembly. *Proc. Natl. Acad. Sci. U. S. A.* **1975**, *72*, 1858-1862.

34. Goedert, M.; Spillantini, M. G.; Jakes, R.; Rutherford, D.; Crowther, R. A., Multiple isoforms of human microtubule-associated protein tau: sequences and localization in neurofibrillary tangles of Alzheimer's disease. *Neuron* **1989**, *3*, 519-526.

35. Savelieff, M. G.; Lee, S.; Liu, Y.; Lim, M. H., Untangling amyloid-beta, tau, and metals in Alzheimer's disease. *ACS Chem. Biol.* **2013**, *8*, 856-865.

36. Levy, S. F.; LeBoeuf, A. C.; Massie, M. R.; Jordan, M. A.; Wilson, L.; Feinstein, S. C., Three- and Four-repeat Tau Regulate the Dynamic Instability of Two Distinct Microtubule Subpopulations in Qualitatively Different Manners: Implications for Neurodegeneration. *J. Biol. Chem.* **2005**, *280*, 13520-13528.

37. Mandelkow, E. M.; Mandelkow, E., Tau in Alzheimer's disease. *Trends Cell Biol.* **1998**, *8*, 425-427.

38. Harada, A.; Oguchi, K.; Okabe, S.; Kuno, J.; Terada, S.; Ohshima, T.; Sato-Yoshitake, R.; Takei, Y.; Noda, T.; Hirokawa, N., Altered microtubule organization in small-calibre axons of mice lacking tau protein. *Nature* **1994**, *369*, 488-491.

39. Gustke, N.; Trinczek, B.; Biernat, J.; Mandelkow, E. M.; Mandelkow, E., Domains of tau protein and interactions with microtubules. *Biochemistry* **1994**, *33*, 9511-9522.

40. Butner, K. A.; Kirschner, M. W., Tau protein binds to microtubules through a flexible array of distributed weak sites. *J. Cell Biol.* **1991**, *115*, 717-730.

41. Elbaum-Garfinkle, S.; Cobb, G.; Compton, J. T.; Li, X. H.; Rhoades, E., Tau mutants bind tubulin heterodimers with enhanced affinity. *Proc. Natl. Acad. Sci. U. S. A.* **2014**, *111*, 6311-6316.

42. Mandelkow, E. M.; Biernat, J.; Drewes, G.; Gustke, N.; Trinczek, B.; Mandelkow, E., Tau domains, phosphorylation, and interactions with microtubules. *Neurobiol. Aging* **1995**, *16*, 355-362.

43. Kadavath, H.; Jaremko, M.; Jaremko, L.; Biernat, J.; Mandelkow, E.; Zweckstetter, M., Folding of the Tau Protein on Microtubules. *Angew. Chem., Int. Ed. Engl.* **2015**, *54*, 10347-10351.

44. Goode, B. L.; Denis, P. E.; Panda, D.; Radeke, M. J.; Miller, H. P.; Wilson, L.; Feinstein, S. C., Functional interactions between the proline-rich and repeat regions of tau enhance microtubule binding and assembly. *Mol. Biol. Cell* **1997**, *8*, 353-365.

45. Chen, J.; Kanai, Y.; Cowan, N. J.; Hirokawa, N., Projection domains of MAP2 and tau determine spacings between microtubules in dendrites and axons. *Nature* **1992**, *360*, 674-677.

46. Scholz, T.; Mandelkow, E., Transport and diffusion of Tau protein in neurons. *Cell. Mol. Life Sci.* **2014**, *71*, 3139-3150.

47. Jebarupa, B.; Muralidharan, M.; Srinivasu, B. Y.; Mandal, A. K.; Mitra, G., Effect of altered solution conditions on tau conformational dynamics: Plausible implication on order propensity and aggregation. *Biochim. Biophys. Acta* **2018**.

48. Ittner, L. M.; Götz, J., Amyloid-β and tau — a toxic pas de deux in Alzheimer's disease. *Nat. Rev. Neurosci.* **2011**, *12*, 67-72.

49. Fitzpatrick, A. W. P.; Falcon, B.; He, S.; Murzin, A. G.; Murshudov, G.; Garringer, H. J.; Crowther, R. A.; Ghetti, B.; Goedert, M.; Scheres, S. H. W., Cryo-EM structures of tau filaments from Alzheimer's disease. *Nature* **2017**, *547*, 185-190.

50. Crowther, R. A.; Goedert, M., Abnormal tau-containing filaments in neurodegenerative diseases. *J. Struct. Biol.* **2000**, *130*, 271-279.

51. Himmelstein, D. S.; Ward, S. M.; Lancia, J. K.; Patterson, K. R.; Binder, L. I., Tau as a therapeutic target in neurodegenerative disease. *Pharmacol. Ther.* **2012**, *136*, 8-22.

52. von Bergen, M.; Friedhoff, P.; Biernat, J.; Heberle, J.; Mandelkow, E. M.; Mandelkow, E., Assembly of tau protein into Alzheimer paired helical filaments depends on a local sequence motif ((306)VQIVYK(311)) forming beta structure. *Proc. Natl. Acad. Sci. U. S. A.* **2000**, *97*, 5129-5134.

53. von Bergen, M.; Barghorn, S.; Biernat, J.; Mandelkow, E. M.; Mandelkow, E., Tau aggregation is driven by a transition from random coil to beta sheet structure. *Biochim. Biophys. Acta* **2005**, *1739*, 158-166.

54. Hutton, M.; Lendon, C. L.; Rizzu, P.; Baker, M.; Froelich, S.; Houlden, H.; Pickering-Brown, S.; Chakraverty, S.; Isaacs, A.; Grover, A., et al., Association of missense and 5'-splice-site mutations in tau with the inherited dementia FTDP-17. *Nature* **1998**, *393*, 702-705.

55. Coppola, G.; Chinnathambi, S.; Lee, J. J.; Dombroski, B. A.; Baker, M. C.; Soto-Ortolaza, A. I.; Lee, S. E.; Klein, E.; Huang, A. Y.; Sears, R., et al., Evidence for a role of the rare p.A152T variant in MAPT in increasing the risk for FTD-spectrum and Alzheimer's diseases. *Hum. Mol. Genet.* **2012**, *21*, 3500-3512.

56. Spires-Jones, T. L.; Stoothoff, W. H.; de Calignon, A.; Jones, P. B.; Hyman, B. T., Tau pathophysiology in neurodegeneration: a tangled issue. *Trends Neurosci.* **2009**, *32*, 150-159.

57. de Calignon, A.; Fox, L. M.; Pitstick, R.; Carlson, G. A.; Bacskai, B. J.; Spires-Jones, T. L.; Hyman, B. T., Caspase activation precedes and leads to tangles. *Nature* **2010**, *464*, 1201-1204.

58. Kopeikina, K. J.; Hyman, B. T.; Spires-Jones, T. L., Soluble forms of tau are toxic in Alzheimer's disease. *Transl. Neurosci.* **2012**, *3*, 223-233.

59. Xu, L.; Zheng, J.; Margittai, M.; Nussinov, R.; Ma, B., How Does Hyperphopsphorylation Promote Tau Aggregation and Modulate Filament Structure and Stability? *ACS Chem. Neurosci.* **2016**, *7*, 565-575.

60. Grundke-Iqbal, I.; Iqbal, K.; Tung, Y. C.; Quinlan, M.; Wisniewski, H. M.; Binder, L. I., Abnormal phosphorylation of the microtubule-associated protein tau (tau) in Alzheimer cytoskeletal pathology. *Proc. Natl. Acad. Sci. U. S. A.* **1986**, *83*, 4913-4917.

61. Alonso, A. C.; Grundke-Iqbal, I.; Iqbal, K., Alzheimer's disease hyperphosphorylated tau sequesters normal tau into tangles of filaments and disassembles microtubules. *Nat. Med.* **1996**, *2*, 783-787.

62. Pooler, A. M.; Usardi, A.; Evans, C. J.; Philpott, K. L.; Noble, W.; Hanger, D. P., Dynamic association of tau with neuronal membranes is regulated by phosphorylation. *Neurobiol. Aging* **2012**, *33*, 431 e427-438.

63. Schwalbe, M.; Kadavath, H.; Biernat, J.; Ozenne, V.; Blackledge, M.; Mandelkow, E.; Zweckstetter, M., Structural Impact of Tau Phosphorylation at Threonine 231. *Structure* **2015**, *23*, 1448-1458.

64. Giannetti, A. M.; Lindwall, G.; Chau, M. F.; Radeke, M. J.; Feinstein, S. C.; Kohlstaedt, L. A., Fibers of tau fragments, but not full length tau, exhibit a cross beta-structure: implications for the formation of paired helical filaments. *Protein Sci.* **2000**, *9*, 2427-2435.

65. Crowther, R. A.; Olesen, O. F.; Smith, M. J.; Jakes, R.; Goedert, M., Assembly of Alzheimer-like filaments from full-length tau protein. *FEBS Lett.* **1994**, *337*, 135-138.

66. Goedert, M.; Wischik, C. M.; Crowther, R. A.; Walker, J. E.; Klug, A., Cloning and sequencing of the cDNA encoding a core protein of the paired helical filament of Alzheimer disease: identification as the microtubule-associated protein tau. *Proc. Natl. Acad. Sci. U. S. A.* **1988**, *85*, 4051-4055.

67. Margittai, M.; Langen, R., Template-assisted filament growth by parallel stacking of tau. *Proc. Natl. Acad. Sci. U. S. A.* **2004**, *101*, 10278-10283.

68. Sanders, D. W.; Kaufman, S. K.; DeVos, S. L.; Sharma, A. M.; Mirbaha, H.; Li, A.; Barker, S. J.; Foley, A. C.; Thorpe, J. R.; Serpell, L. C., et al., Distinct tau prion strains propagate in cells and mice and define different tauopathies. *Neuron* **2014**, *82*, 1271-1288.

69. Bibow, S.; Mukrasch, M. D.; Chinnathambi, S.; Biernat, J.; Griesinger, C.; Mandelkow, E.; Zweckstetter, M., The dynamic structure of filamentous tau. *Angew. Chem., Int. Ed. Engl.* **2011**, *50*, 11520-11524.

70. Falcon, B.; Cavallini, A.; Angers, R.; Glover, S.; Murray, T. K.; Barnham, L.; Jackson, S.; O'Neill, M. J.; Isaacs, A. M.; Hutton, M. L., et al., Conformation determines the seeding potencies of native and recombinant Tau aggregates. *J. Biol. Chem.* **2015**, *290*, 1049-1065.

71. Clavaguera, F.; Akatsu, H.; Fraser, G.; Crowther, R. A.; Frank, S.; Hench, J.; Probst, A.; Winkler, D. T.; Reichwald, J.; Staufenbiel, M., et al., Brain homogenates from human tauopathies induce tau inclusions in mouse brain. *Proc. Natl. Acad. Sci. U. S. A.* **2013**, *110*, 9535-9540.

72. Frost, B.; Ollesch, J.; Wille, H.; Diamond, M. I., Conformational diversity of wild-type Tau fibrils specified by templated conformation change. *J. Biol. Chem.* **2009**, *284*, 3546-3551.

73. Lippens, G.; Wieruszeski, J. M.; Leroy, A.; Smet, C.; Sillen, A.; Buee, L.; Landrieu, I., Proline-directed random-coil chemical shift values as a tool for the NMR assignment of the tau phosphorylation sites. *ChemBioChem* **2004**, *5*, 73-78.

74. Eliezer, D.; Barré, P.; Kobaslija, M.; Chan, D.; Li, X.; Heend, L., Residual Structure in the Repeat Domain of Tau: Echoes of Microtubule Binding and Paired Helical Filament Formation. *Biochemistry* **2005**, *44*, 1026-1036.

75. Daly, N. L.; Hoffmann, R.; Otvos, L.; Craik, D. J., Role of Phosphorylation in the Conformation of τ Peptides Implicated in Alzheimer's Disease. *Biochemistry* **2000**, *39*, 9039-9046.

76. Cleveland, D. W.; Hwo, S. Y.; Kirschner, M. W., Physical and chemical properties of purified tau factor and the role of tau in microtubule assembly. *J. Mol. Biol.* **1977**, *116*, 227-247.

77. Schweers, O.; Schonbrunn-Hanebeck, E.; Marx, A.; Mandelkow, E., Structural studies of tau protein and Alzheimer paired helical filaments show no evidence for beta-structure. *J. Biol. Chem.* **1994**, *269*, 24290-24297.

78. Jeganathan, S.; von Bergen, M.; Mandelkow, E. M.; Mandelkow, E., The natively unfolded character of tau and its aggregation to Alzheimer-like paired helical filaments. *Biochemistry* **2008**, *47*, 10526-10539.

79. Woody, R. W.; Clark, D. C.; Roberts, G. C. K.; Martin, S. R.; Bayley, P. M., Molecular flexibility in microtubule proteins: proton nuclear magnetic resonance characterization. *Biochemistry* **1983**, *22*, 2186-2192.

80. Greenfield, N. J., Using circular dichroism spectra to estimate protein secondary structure. *Nat. Protoc.* **2006**, *1*, 2876-2890.

81. Nath, A.; Sammalkorpi, M.; DeWitt, D. C.; Trexler, A. J.; Elbaum-Garfinkle, S.; O'Hern, C. S.; Rhoades, E., The conformational ensembles of alpha-synuclein and tau: combining single-molecule FRET and simulations. *Biophys. J.* **2012**, *103*, 1940-1949.

82. Jeganathan, S.; Hascher, A.; Chinnathambi, S.; Biernat, J.; Mandelkow, E. M.; Mandelkow, E., Proline-directed pseudo-phosphorylation at AT8 and PHF1 epitopes induces a compaction of the paperclip folding of Tau and generates a pathological (MC-1) conformation. *J. Biol. Chem.* **2008**, *283*, 32066-32076.

83. Elbaum-Garfinkle, S.; Rhoades, E., Identification of an Aggregation-Prone Structure of Tau. *J. Am. Chem. Soc.* **2012**, *134*, 16607-16613.

84. Akoury, E.; Mukrasch, M. D.; Biernat, J.; Tepper, K.; Ozenne, V.; Mandelkow, E.; Blackledge, M.; Zweckstetter, M., Remodeling of the conformational ensemble of the repeat domain of tau by an aggregation enhancer. *Protein Sci.* **2016**, *25*, 1010-1020.

85. Mao, A. H.; Crick, S. L.; Vitalis, A.; Chicoine, C. L.; Pappu, R. V., Net charge per residue modulates conformational ensembles of intrinsically disordered proteins. *Proc. Natl. Acad. Sci. U. S. A.* **2010**, *107*, 8183-8188.

86. Orte, A.; Birkett, N. R.; Clarke, R. W.; Devlin, G. L.; Dobson, C. M.; Klenerman, D., Direct characterization of amyloidogenic oligomers by single-molecule fluorescence. *Proc. Natl. Acad. Sci. U. S. A.* **2008**, *105*, 14424-14429.

87. Sisamakis, E.; Valeri, A.; Kalinin, S.; Rothwell, P. J.; Seidel, C. A. M., Accurate Single-Molecule FRET Studies Using Multiparameter Fluorescence Detection. *Methods Enzymol.* **2010**, *475*, 455-514.

88. Banerjee, P. R.; Mitrea, D. M.; Kriwacki, R. W.; Deniz, A. A., Asymmetric Modulation of Protein Order-Disorder Transitions by Phosphorylation and Partner Binding. *Angew. Chem., Int. Ed. Engl.* **2016**, *55*, 1675-1679.

89. Aznauryan, M.; Nettels, D.; Holla, A.; Hofmann, H.; Schuler, B., Single-molecule spectroscopy of cold denaturation and the temperature-induced collapse of unfolded proteins. *J. Am. Chem. Soc.* **2013**, *135*, 14040-14043.

90. Chung, H. S.; McHale, K.; Louis, J. M.; Eaton, W. A., Single-molecule fluorescence experiments determine protein folding transition path times. *Science* **2012**, *335*, 981-984.

91. Banerjee, P. R.; Deniz, A. A., Shedding light on protein folding landscapes by single-molecule fluorescence. *Chem. Soc. Rev.* **2014**, *43*, 1172-1188.

92. Cremades, N.; Cohen, S. I.; Deas, E.; Abramov, A. Y.; Chen, A. Y.; Orte, A.; Sandal, M.; Clarke, R. W.; Dunne, P.; Aprile, F. A., et al., Direct observation of the interconversion of normal and toxic forms of alpha-synuclein. *Cell* **2012**, *149*, 1048-1059.

93. Rasnik, I.; McKinney, S. A.; Ha, T., Surfaces and orientations: much to FRET about? *Acc. Chem. Res.* **2005**, *38*, 542-548.

94. Ha, T., Single-molecule fluorescence resonance energy transfer. *Methods* **2001**, *25*, 78-86.

95. Akabayov, B.; Henn, A.; Elbaum, M.; Sagi, I., RNA labeling and immobilization for nano-displacement measurement: probing three-dimensional RNA structure. *IEEE Trans. NanoBioscience* **2003**, *2*, 70-74.

96. Friedel, M.; Baumketner, A.; Shea, J. E., Effects of Surface Tethering on Protein Folding Mechanisms. *Proc. Natl. Acad. Sci. U. S. A.* **2006**, *103*, 8396-8401.

97. Talaga, D. S.; Lau, W. L.; Roder, H.; Tang, J.; Jia, Y.; DeGrado, W. F.; Hochstrasser, R. M., Dynamics and Folding of Single Two-Stranded Coiled-Coil Peptides Studied by Fluorescent Energy Transfer Confocal Microscopy. *Proc. Natl. Acad. Sci. U. S. A.* **2000**, *97*, 13021-13026.

98. Wang, Q.; Goldsmith, R. H.; Jiang, Y.; Bockenhauer, S. D.; Moerner, W. E., Probing single biomolecules in solution using the anti-Brownian electrokinetic (ABEL) trap. *Acc. Chem. Res.* **2012**, *45*, 1955-1964.

99. Moffitt, J. R.; Chemla, Y. R.; Smith, S. B.; Bustamante, C., Recent advances in optical tweezers. *Annu Rev Biochem* **2008**, *77*, 205-228.

100. Peterman, E. J. G.; Gittes, F.; Schmidt, C. F., Laser-Induced Heating in Optical Traps. *Biophys. J.* **2003**, *84*, 1308-1316.

101. Cohen, A. Trapping and Manipulating Single Molecules in Solution. Stanford University, 2006.

102. Wang, Q. Enabling Multivariate Investigation of Single-Molecule Dynamics in Solution by Counteracting Brownian Motion. Stanford University, 2014.

103. Wang, Q.; Moerner, W. E., An Adaptive Anti-Brownian ELectrokinetic trap with real-time information on single-molecule diffusivity and mobility. *ACS Nano* **2011**, *5*, 5792-5799.

104. Goldsmith, R. H.; Tabares, L. C.; Kostrz, D.; Dennison, C.; Aartsma, T. J.; Canters, G. W.; Moerner, W. E., Redox cycling and kinetic analysis of single molecules of solution-phase nitrite reductase. *Proc. Natl. Acad. Sci. U. S. A.* **2011**, *108*, 17269-17274.

105. Cohen, A. E.; Moerner, W. E., Principal-components analysis of shape fluctuations of single DNA molecules. *Proc. Natl. Acad. Sci. U. S. A.* **2007**, *104*, 12622-12627.

106. Wang, Q.; Moerner, W. E., Lifetime and Spectrally Resolved Characterization of the Photodynamics of Single Fluorophores in Solution Using the Anti-Brownian Electrokinetic Trap. *J. Phys. Chem. B* **2013**, *117*, 4641-4648.

107. Cohen, A. E.; Moerner, W. E., Controlling Brownian motion of single protein molecules and single fluorophores in aqueous buffer. *Opt. Express* **2008**, *16*, 6941-6956.

108. Wang, Q.; Moerner, W. E., Optimal strategy for trapping single fluorescent molecules in solution using the ABEL trap. *Appl. Phys. B* **2010**, *99*, 23-30.

109. Welch, G.; Bishop, G. *An Introduction to the Kalman Filter*; University of North Carolina at Chapel Hill: 1995.

110. MathWorks Understanding Kalman Filters. https://www.mathworks.com/videos/understanding-kalman-filters-part-4-optimal-state-estimator-algorithm--1493129749201.html (accessed July 17, 2018).

111. Kartalov, E. P.; Unger, M. A.; Quake, S. R., Polyelectrolyte surface interface for single-molecule fluorescence studies of DNA polymerase. *BioTechniques* **2003**, *34*, 505-510.

112. Lakowicz, J. R., *Principles of fluorescence spectroscopy*, 3rd ed.; Springer: New York, 2006.

113. Ellis, J. P.; Culviner, P. H.; Cavagnero, S., Confined dynamics of a ribosome-bound nascent globin: Cone angle analysis of fluorescence depolarization decays in the presence of two local motions. *Protein Sci.* **2009**, *18*, 2003-2015.

114. Lipari, G.; Szabo, A., Effect of librational motion on fluorescence depolarization and nuclear magnetic resonance relaxation in macromolecules and membranes. *Biophys. J.* **1980**, *30*, 489-506.

115. Kinosita, K., Jr.; Ikegami, A.; Kawato, S., On the wobbling-in-cone analysis of fluorescence anisotropy decay. *Biophys. J.* **1982**, *37*, 461-464.

Chapter 2

2. Detecting Conformational Variants of Solution-Phase Intrinsically Disordered Tau Protein at the Single-Molecule Level

The material in this chapter was originally published as Manger, L. H.; Foote, A. K.; Wood, S. L.; Holden, M. R.; Heylman, K. D.; Margittai, M.; Goldsmith, R. H., Revealing Conformational Variants of Solution-Phase Intrinsically Disordered Tau Protein at the Single-Molecule Level. *Angew. Chem., Int. Ed. Engl.* **2017**, 56, 15584-15588.

2.1 Abstract

Intrinsically disordered proteins, such as tau protein, adopt a variety of conformations in solution, complicating solution-phase structural studies. We employ an anti-Brownian electrokinetic (ABEL) trap to prolong measurements of single tau proteins in solution. Once trapped, we record the fluorescence anisotropy to investigate the diversity of conformations sampled by the single molecules. A distribution of anisotropy values obtained from trapped tau protein is conspicuously bimodal while those obtained by trapping a globular protein or individual fluorophores are not. Time-resolved fluorescence anisotropy measurements are used to provide an explanation of the bimodal distribution as originating from a shift in the compaction of the two different families of conformations.

2.2 Introduction

Tau protein is an intrinsically disordered protein (IDP) that performs a vital role in the human central nervous system by regulating[1] and stabilizing microtubules in the axons of neurons.[2] Tau consists of an N-

terminal projection domain, proline rich region, microtubule-binding region (MTBR), and C-terminal tail (Figure 2-1a).[3] The MTBR consists of 3 or 4 imperfect repeats that have a strong affinity for microtubules.[4] In the pathogenic form, however, this repeat region loses this affinity, adopts a β-sheet structure,[5] and aggregates into paired helical and straight filaments associated with Alzheimer's disease[6-7] or other types of filaments associated with other tauopathies.[8] Pathogenic aggregation is also influenced in a complex manner by phosphorylation of tau by cellular kinases.[9] Importantly, it has also been suggested that it is not the insoluble aggregates, but rather the soluble precursor oligomers that are the toxic species.[10] These studies highlight that understanding the conformations of monomers and the earliest steps of aggregation are critical to understanding Alzheimer's disease etiology.

Tau protein is flexible and known to display conformational dynamics in solution. Circular dichroism measurements of tau monomer show a characteristic trough around 200 nm indicating a random coil structure.[11] Electron paramagnetic resonance measurements confirm a high degree of mobility of residues in the MTBR and C-terminal end.[12-13] Even though tau is an IDP, there is evidence that it is not completely devoid of structural motifs. Intramolecular distances — as determined by Förster resonance energy transfer (FRET) — are shorter than would be expected for a perfect random coil, leading to the proposed "paperclip" conformation.[14] Detailed single molecule (SM) FRET measurements further confirm the global compactness

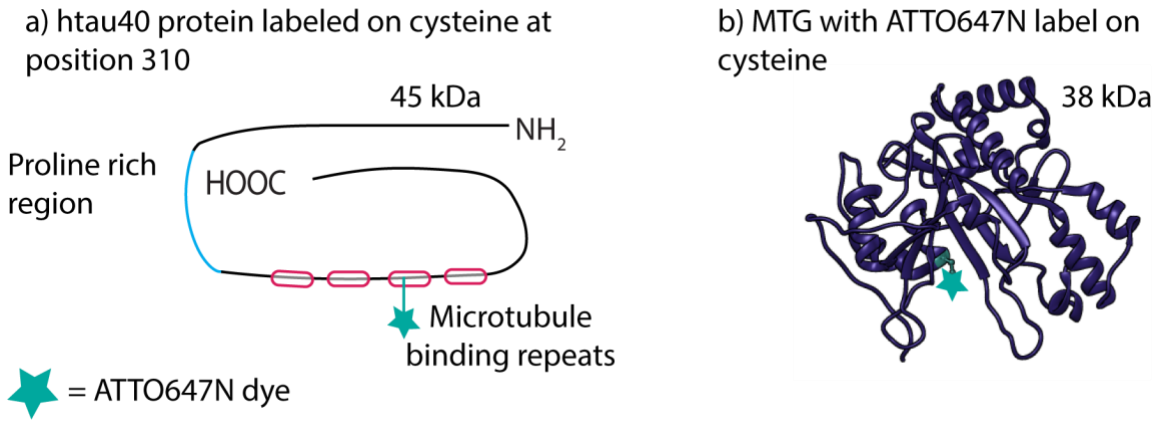

Figure 2-1. Structures of (a) htau40 with cysteine residue labeled with ATTO647N dye and (b) microbial transglutaminase (MTG) based on crystal structure 1IU4 from Kashiwagi *et al.*, *J. Biol. Chem.* 2002, *277* (46), 44252-44260.

of the tau protein with the N- and C-termini in relatively close contact with the MTBR while proposing an "S-shaped" conformation.[15] There is also evidence through the interaction of tau protein with microtubules and aggregation inducers that different regions of the protein adopt different conformations[16] and different degrees of compaction.[15] NMR techniques are also capable of reporting on intramolecular distances and, when combined with computational studies, imply that monomeric tau adopts at least 30 different conformers in solution.[17]

Solution-phase SM measurements are a powerful tool for characterizing the heterogeneity of protein conformations, particularly when attachment to a surface is likely to induce artificial conformations.[18-20] Solution-phase SM studies can report not only on different conformations and assemblies,[15, 21-23] but also the transition pathways,[24-25] and kinetics of the conversions.[26-29] These methods, however, examine freely diffusing proteins as they transiently pass through a near diffraction-limited confocal volume. Due to the limited time (and number of photons collected) during the molecule's residence in the excitation volume, measurements are often characterized by low signal-to-noise ratios, with histograms significantly broadened by shot noise.

Here, we prolong the measurement of the freely diffusing protein by employing an anti-Brownian electrokinetic (ABEL) trap. This microfluidic device tracks the position of a fluorescently labeled tau protein and provides real-time feedback voltages which induce an electrokinetic flow to push the protein back to center, allowing observation for multiple seconds without perturbative immobilization.[20, 30-31] These long observation times allow collection of orders of magnitude more photons, leading to histograms whose widths may be representative of distinct molecular populations, rather than a consequence of limited statistics.

In this work, we use the ABEL trap to perform the first prolonged single-molecule investigation on a monomeric IDP. We employ fluorescence anisotropy as a reporter for solution-phase conformations of individual tau proteins. Fluorescence anisotropy is a versatile tool for monitoring rotational dynamics of

interacting biomolecules in solution.[32] Anisotropy is a measure of the shift in polarization of emitted photons relative to excitation photons, providing a way of characterizing the extent and timescale of molecular reorientation during the nanosecond excited-state lifetime.

We investigate the full-length isoform of tau protein (htau40) containing 441 residues and weighing 45 kDa.[33] For our studies, the naturally occurring cysteine residues at 291 and 322[33] have been mutated to serine residues, and the tyrosine residue at 310 has been mutated to a cysteine (htau40-Y310C). The cysteine is then labeled by covalently linking an ATTO647N dye (Figure 2-1a), chosen for its high stability at the required high photon count rate.[20] This labeling position has been used previously without disturbing the structure or functionality of tau protein.[14] We will refer to this dye-labeled mutant simply as htau40, unless otherwise noted.

2.3 Results

2.3.1 Anisotropy histograms reveal heterogeneity in single-molecule motions

To properly calibrate our method and gain meaningful insight into solution-phase conformations of htau40, we establish a baseline for comparison consisting of multiple control samples: free ATTO647N dye and microbial transglutaminase (MTG), a globular protein comparable in size (38 kDa) to htau40 with a single cysteine residue in the active site available for labeling (Figure 2-1b).[34]

Upon activation of the ABEL trap, solution-phase molecules were trapped for an average of 3 seconds (Figure 2-2) and the steady-state anisotropy was determined (Figure 2-3). All protein samples were trapped in 25 % glycerol to slow the evaporation of the buffer during the experiment and to facilitate trapping by lowering the diffusion constant. Free ATTO647N dye was trapped in 50 % and 80 % glycerol in order to produce a comparable anisotropy to htau40 and MTG, respectively (Figure 2-4).

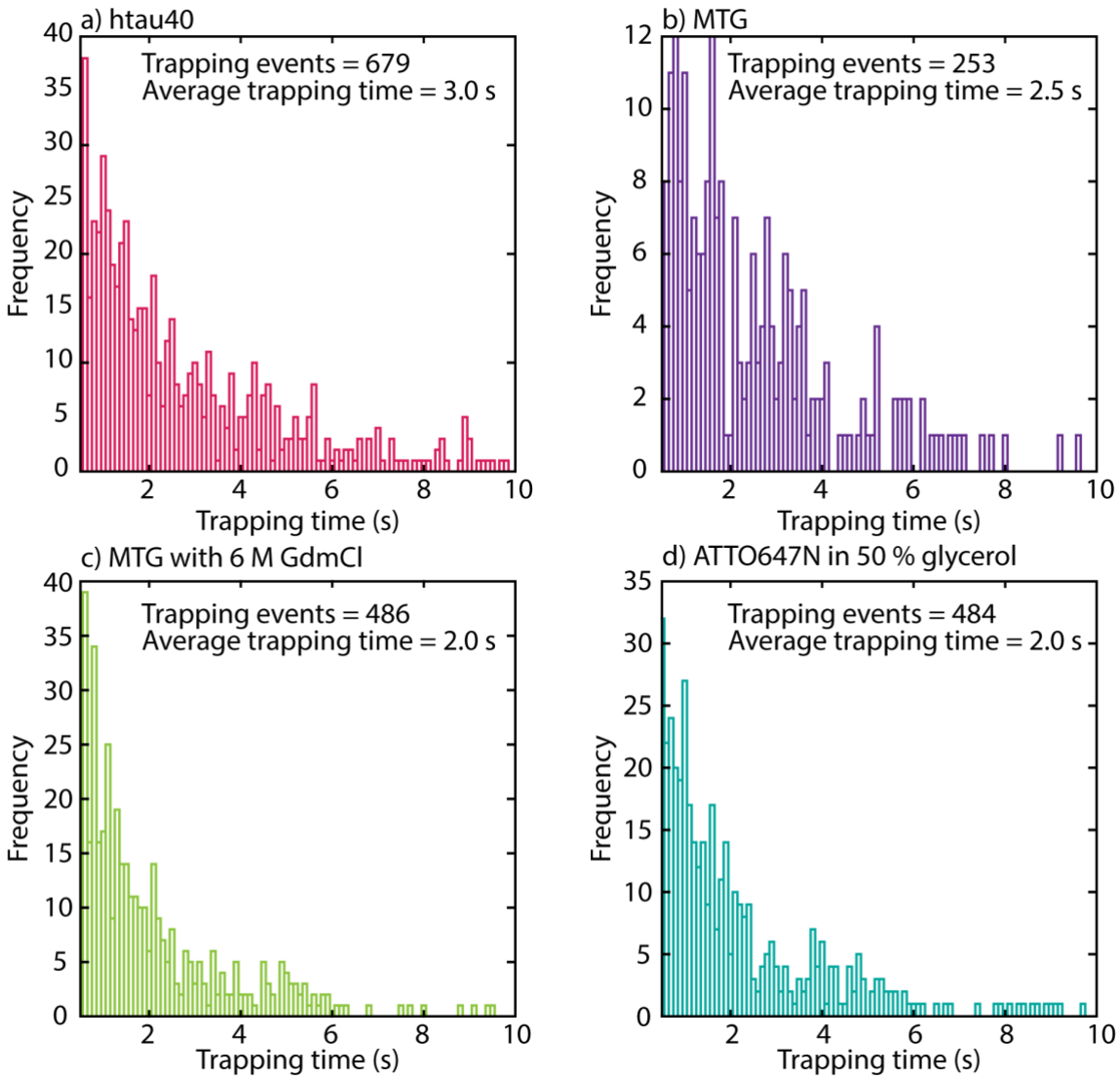

Figure 2-2. Trapping times for individual trapping events. (a) htau40, (b) MTG and (c) MTG with 6 M GdmCl were trapped in 25 % glycerol solution. (d) Individual hydrolyzed ATTO647N molecules were trapped in a solution of 50 % glycerol. The trapping time is ultimately limited by the photobleaching of the fluorophore; upon photobleaching, the molecule becomes invisible to the system and cannot be tracked. Other more minor causes of losing a molecule include the molecule moving beyond the scanning pattern so that the fluorophore is no longer excited, or another, brighter, molecule diffusing into the center of the trap.

The fluorescence anisotropy of each molecule is indicative of the freedom of rotational motion of the attached ATTO647N dye. If the fluorophore can quickly explore a full range of angles, the steady-state anisotropy value will be near zero due to complete depolarization. If the molecule has a restricted range of motion, or if rotational motions are sluggish, higher values of anisotropy are expected.

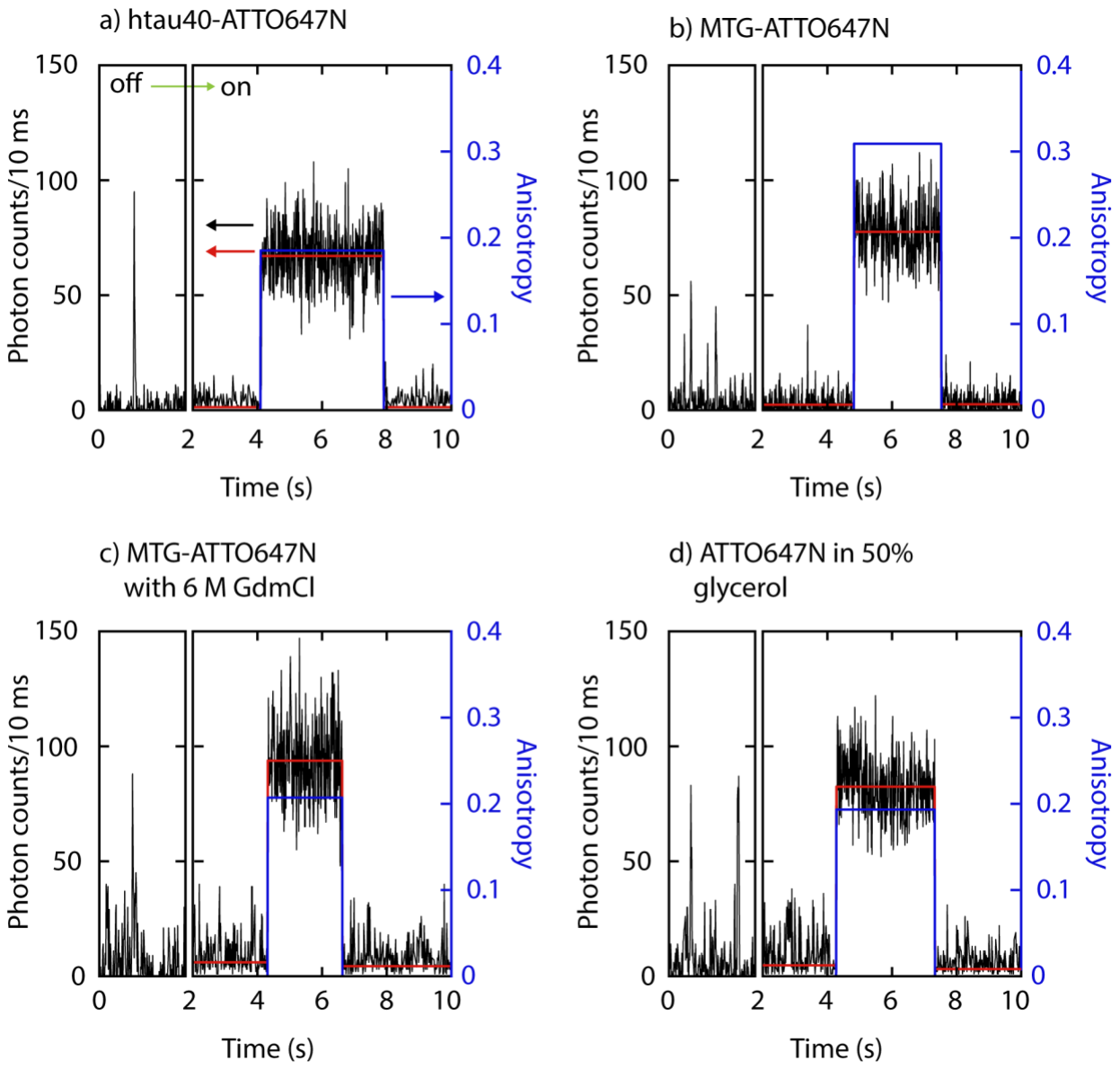

Figure 2-3. Representative traces for molecules in the ABEL trap, with feedback voltages off (left) and on (right). (a) htau40-ATTO647N, (b) MTG-ATTO647N, and (c) MTG-ATTO647N denatured with 6 M guanidinium chloride (GdmCl) were trapped in solutions with 25 % glycerol. (d) Hydrolyzed ATTO647N was trapped in buffer with 50 % glycerol. Change points in the trapping data are shown in red (left axis) and anisotropy is shown in blue (right axis).

After prolonged trapping of hundreds of individual molecules, we constructed anisotropy histograms for each sample (Figure 2-4). The histogram for htau40 displays a conspicuous bimodal distribution of anisotropy values (Figure 2-4a), while the distribution for MTG can be fit to a single, narrower

Gaussian (Figure 2-4b). The differences in shape and center anisotropy values indicate a difference between the fluorescence-depolarizing motions of the two samples: the htau40 sample has a lower anisotropy value and bimodal distribution and thus more freedom of rotation and conformational heterogeneity. If the label on MTG were situated in a less constrained environment, a center anisotropy value closer to htau40 would be expected as the dye would likely have more rotational freedom, though a single peak would still be anticipated. The average anisotropy values for these two histograms agree with bulk samples, indicating that trapping does not influence protein rotational motions (Table 2-1).

Table 2-1. Comparison of average single-molecule (SM) anisotropy data with bulk steady-state fluorimeter anisotropy data (mean ± standard deviation of the mean).

Sample	r (SM data)	r (fluorimeter)
htau40-ATTO647N	0.188 ± 0.001	0.169 ± 0.003
htau40-ATTO633	0.142 ± 0.001	0.1445 ± 0.0008
MTG	0.308 ± 0.001	0.319 ± 0.008
MTG with 6 M GdmCl	0.223 ± 0.001	0.237 ± 0.001
ATTO647N in 50 % glycerol	0.1836 ± 0.0009	0.142 ± 0.003
ATTO647N in 80 % glycerol	0.293 ± 0.001	0.296

2.3.2 Width of htau40 anisotropy histogram characteristic of IDP

In order to determine whether the wide, bimodal distribution is unique to htau40 or whether it is characteristic of any disordered protein, we induced disorder in MTG by denaturing it with 6 M guanidinium chloride (GdmCl). Upon denaturation of MTG, the anisotropy histogram shifts to a lower value despite the increase in viscosity, indicating that the fluorophore is able to rotate more freely, as expected, and also shows a single, broad, dominant peak in the anisotropy histogram (Figure 2-4d). While htau40 lacks a stable secondary structure and tertiary contacts, htau40 has also been known to adopt weak intramolecular interactions, such as in the paperclip model.[14] Upon adding 6 M GdmCl to completely disrupt any of these

potential weak interactions, the distribution merges into a single peak with an average anisotropy value between the two peaks in Figure 2-4a (Figure 2-4c).

Another important comparison is made between a protein — which has the potential for solution-phase heterogeneity — and samples such as free molecular ATTO647N which is not expected to have

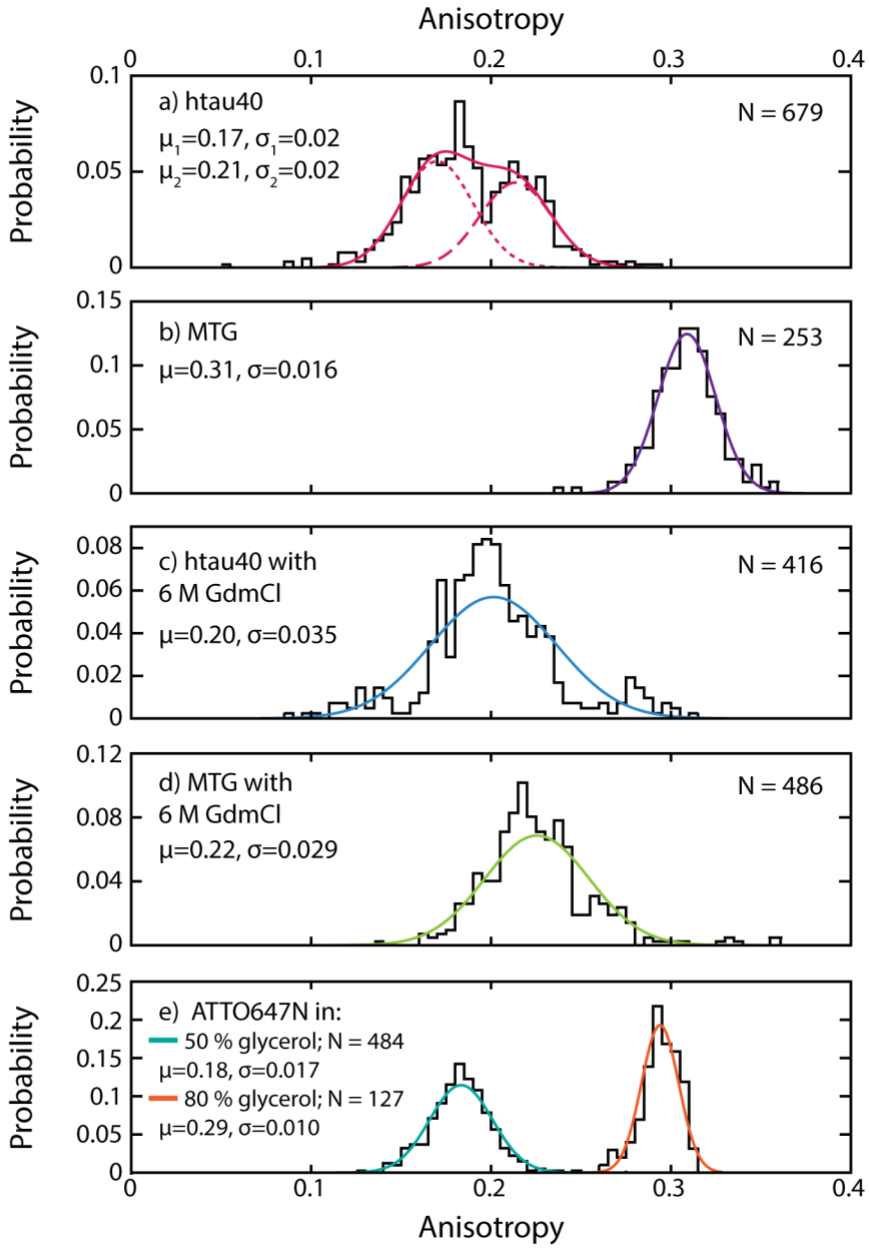

Figure 2-4. Histograms of single-molecule anisotropy values (black) fit with Gaussian curves (multiple colors). μ is the average anisotropy and σ is the standard deviation. Samples for plots (a) — (d) were prepared in a buffer with 25 % glycerol.

multiple conformations in solution (Figure 2-4e). Since the dye samples produced comparable number of photons per event, these samples were used to ascertain the narrowest width of anisotropy histogram that we can resolve at each anisotropy value due to instrument limitations or dye photophysics.[35-36] Comparison of the widths of the protein histograms to the dye histograms at the same average anisotropy value

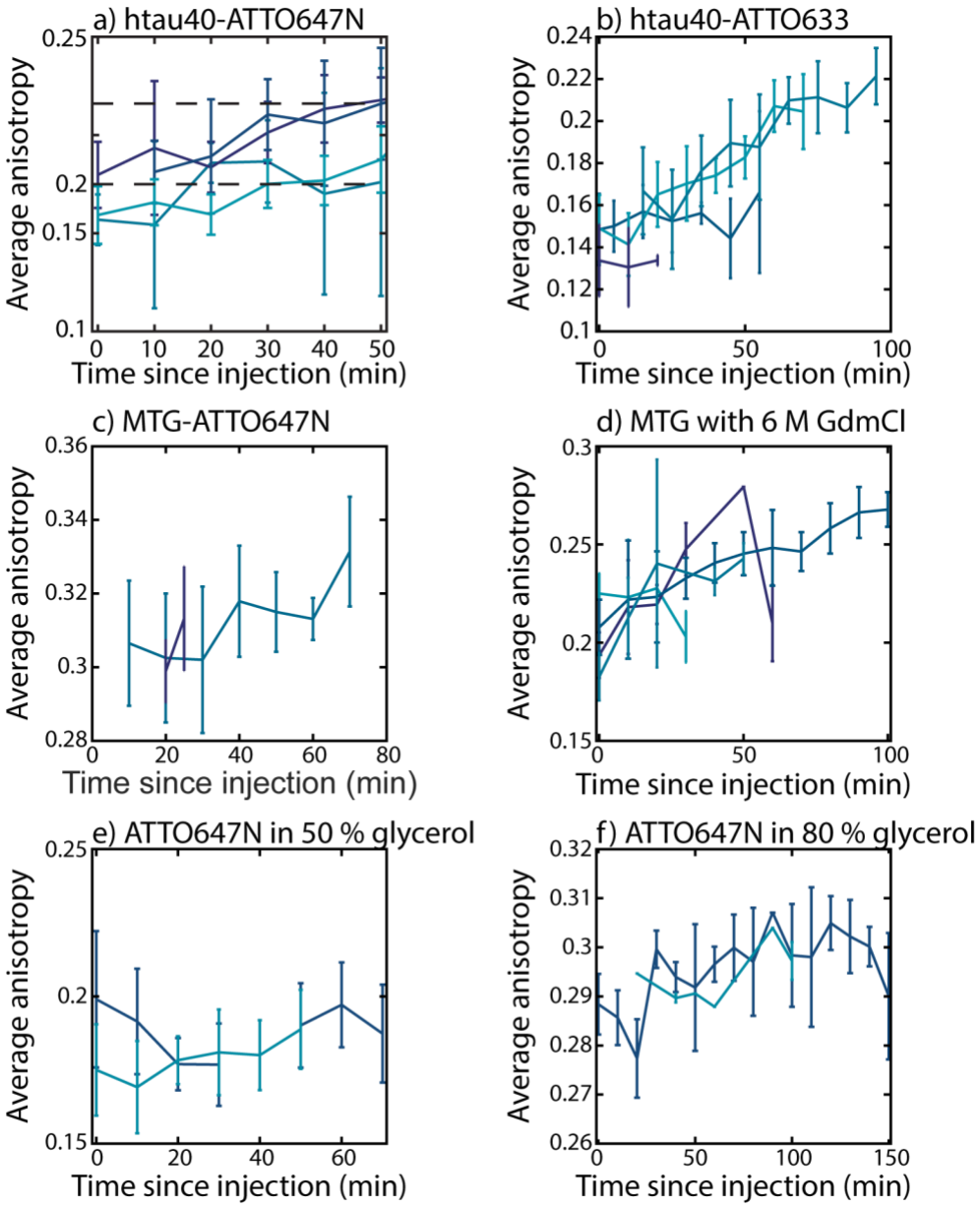

Figure 2-5. Average anisotropy ± standard deviation fluctuates during the experiment. Different colors represent different trapping experiments. Samples (a) — (d) were prepared in a solution of 25 % glycerol. Dashed lines in (a) represent the average anisotropy of the two peaks in Figure 2-4a.

suggests that while these processes contribute to the observed anisotropy, the protein heterogeneity makes the dominant contribution to the observed anisotropy distribution.

Though NMR techniques have found at least 30 solution-phase conformers,[17] our single-molecule experiments indicate two underlying populations. We attribute these two underlying conformations to two families of related conformers and not simply two conformations. We also note that we saw no evidence of transitions between these families within the average trapping window, and thus these conformations are stable on the timescale of multiple seconds (see 2.6.12.3). We do note that over an hour of trapping htau40, the average anisotropy slowly changes from favoring the lower anisotropy peak (r_L = 0.17) to the upper anisotropy peak (r_U = 0.21) (Figure 2-5). This detail indicates that conversion between the states occurs over a timescale of tens of minutes.

2.3.3 Molecular motions revealed by time-resolved anisotropy

To gain insight into the molecular motions responsible for the observed heterogeneity, bulk time-resolved fluorescence anisotropy measurements were performed (Figure 2-6). The free dye samples show monoexponential anisotropy decays, as expected, due to their lack of available conformations (Figure 2-7). Anisotropy decays for htau40 samples, on the other hand, display triexponential behavior with an initial fast (ϕ_F) decay followed by an intermediate (ϕ_I) and slow (ϕ_S) decay (Figure 2-6, magenta). The timescales of the decays were used to assign their likely originating motions. We have assigned the fastest component to dye rotations about their flexible linkers and the intermediate component to a segmental motion of the protein.[37] The slowest component could either be a different segmental motion for a larger domain or a global motion around the shorter axis of a non-spherical object. Global motions corresponding to motion around longer axes of the IDP take too long to be observed here (see 2.4.2).

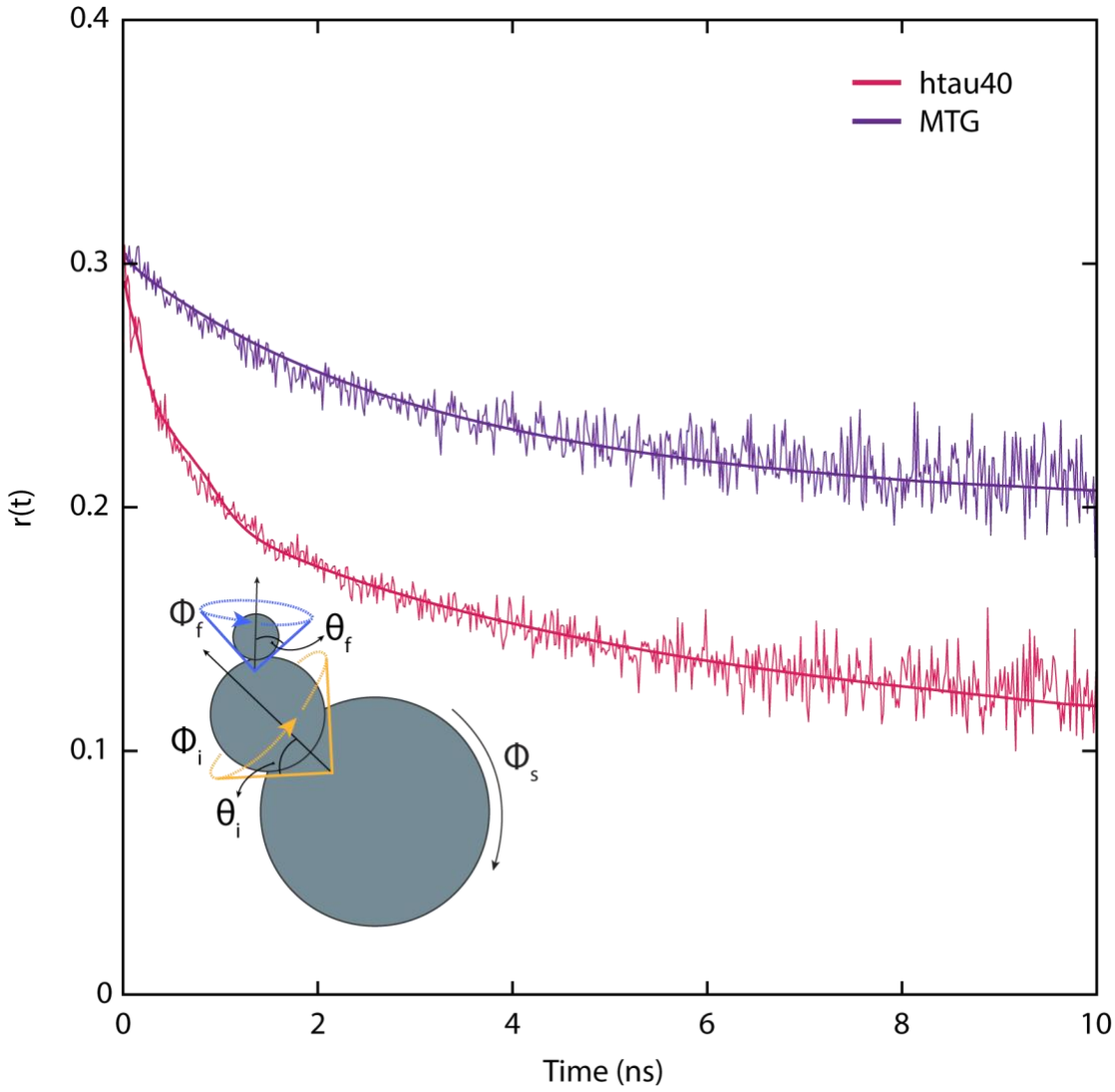

Figure 2-6. Time-resolved anisotropy of htau40-ATTO647N (magenta) and MTG (purple). Anisotropy fit parameters are given in Table 2-3. Samples were measured in a buffer which contained 25 % glycerol.

MTG samples, on the other hand, show biexponential decay behavior (Figure 2-6, purple). The short decay for MTG is also likely due to the rotation of the dye around the linker, though it may also contain contributions from segmental motion of a short loop. The absence of an intermediate decay is consistent with the more defined structure of MTG, with the longer component ascribed to global motion.

The protein anisotropy decays are fit to equations describing wobbling-in-a-cone or cone-in-a-cone behavior with one or two local motions, where the critical parameters include cone half-angles (θ) and

rotational correlation times (ϕ), Figure 2-6, inset (see 2.6.12.2).[38-39] Critically, the θs of the fast components corresponding to local dye motion are quite similar for the two proteins (29° for ATTO647N attached to htau40 and 30° when attached to MTG) even as the average timescales of these motions are very different (ϕ_f = 0.25 ns for htau40 and 1.9 ns for MTG) (Table 2-3). The significantly slower motion in MTG is expected due to the restrictive environment of the active site, which may preclude large amplitude dye motions that contribute to anisotropy decay.[40] In contrast, the dye attached to htau40 exhibits some limitations in motion compared to an untethered dye, but is substantially freer than in MTG.

Segmental motions of the tau protein are likely responsible for the intermediate component in the anisotropy decay as IDPs have been identified via time-resolved anisotropy to have high backbone flexibility that may stiffen upon binding to a partner.[37] The intermediate timescale dynamics corresponding to the segmental motion of htau40 was found to have an average correlation time of ϕ_i = 5.3 ns and a cone of

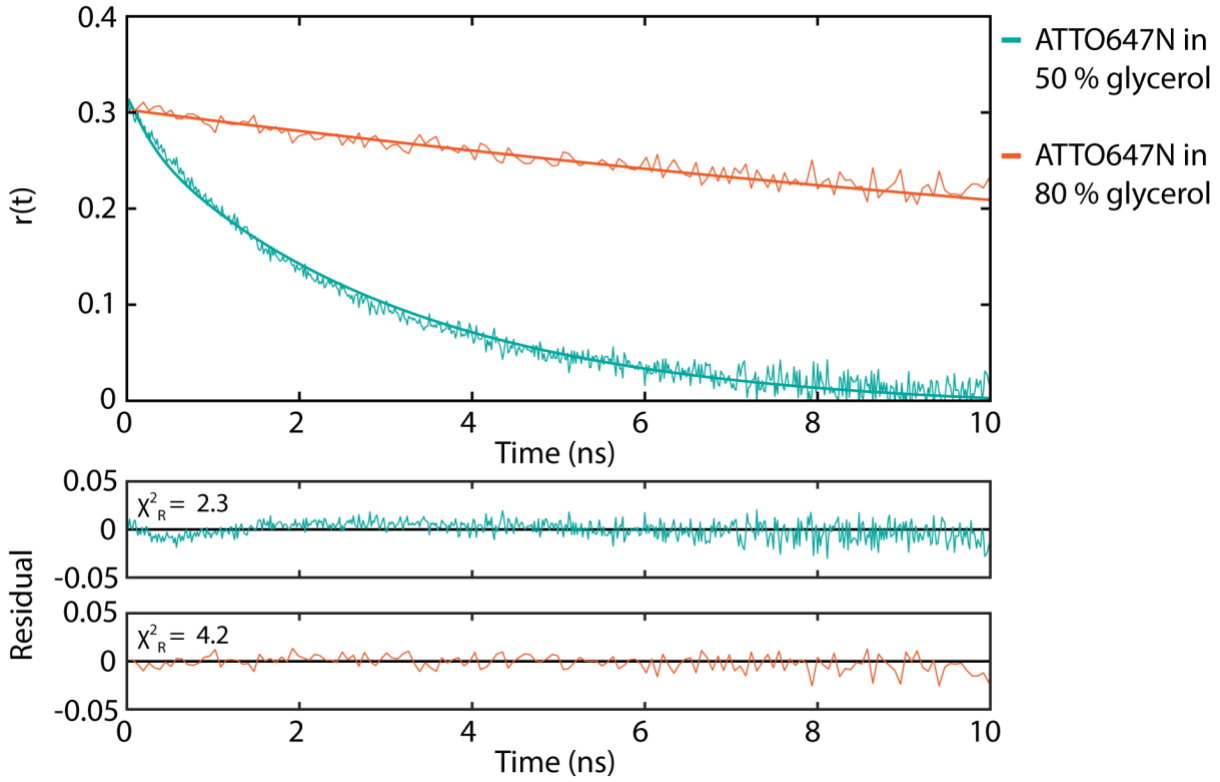

Figure 2-7. Time-resolved anisotropy decay of ATTO647N in 50 % and 80 % glycerol fit with monoexponential decays. χ^2_R is the reduced χ^2 value for the fit shown. Anisotropy fit parameters are given in Table 2-3.

half-angle θ_i = 30°. The existence of this intermediate segmental motion is unique to the IDP. MTG does not display an intermediate timescale motion, and beyond the fast decay, only showed one slow motion, ϕ_s = 90 ns, likely originating from the global motion of the molecule. The long timescale motion of htau40 exhibits ϕ_s = 118 ns.

2.3.4 ATTO647N and protein non-specific interaction

Although ATTO647N has been shown to be hydrophobic,[41] we chose to use it because of its photostability, which is necessary for achieving long trapping times. We verified that the hydrophobicity of the dye was not detrimental to our measurements by analyzing the bulk anisotropy using a fluorimeter for samples of hydrolyzed ATTO647N dye with excess unlabeled protein. The anisotropy of hydrolyzed dye in 25 % glycerol is 0.075 ± 0.003 (mean ± standard deviation of the mean). Upon addition of a ten-fold excess of unlabeled htau40 (mutated to have no cysteines), the anisotropy of the hydrolyzed dye remains essentially unchanged at 0.074 ± 0.004. This lack of a shift indicates an absence of strong non-specific interactions between the htau40 and the dye that could affect the anisotropy. When a ten-fold excess of unlabeled MTG was added, the anisotropy rose slightly from 0.075 to 0.12 ± 0.02. In contrast to htau40, MTG shows a small increase in anisotropy, indicative of some interaction, likely in the binding pocket. Observation of this rise demonstrates the ability of this method to discern strong hydrophobic interactions if they are present.

2.3.5 Comparison of labeling with ATTO647N and ATTO633

Since ATTO647N is known to be a hydrophobic dye,[41] we wanted to assess whether using another less hydrophobic dye, ATTO633, would produce the same results. ATTO633 has been used previously for ABEL trap experiments[42] and is a less hydrophobic alternative to ATTO647N, as indicated by retention times in reverse HPLC measurements and aggregation behavior in aqueous solution of dye-streptavidin

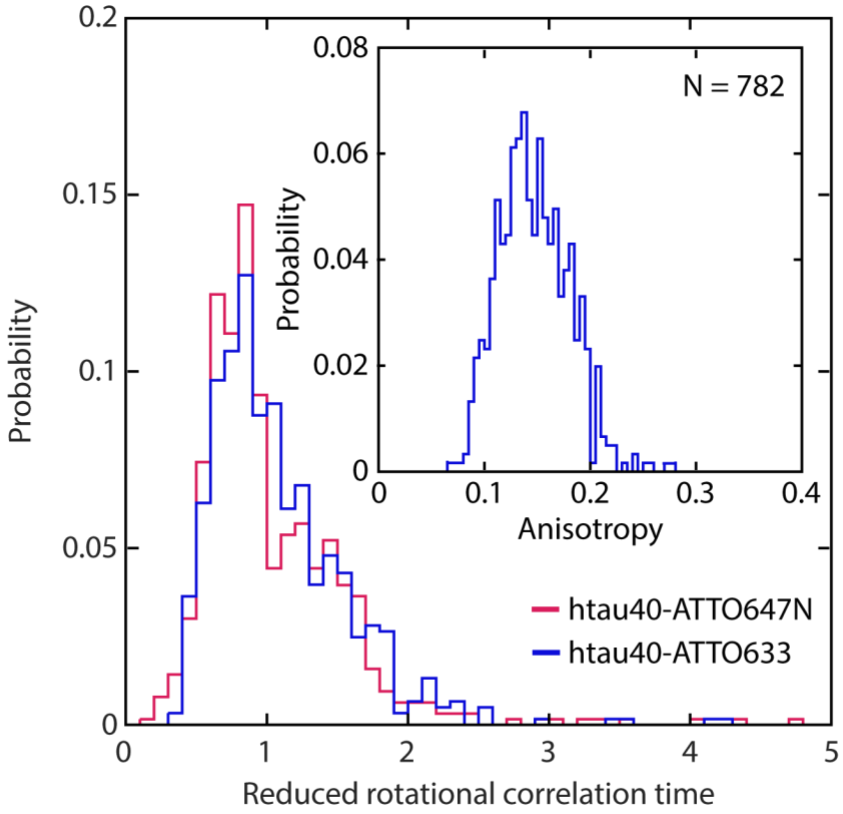

Figure 2-8. Reduced rotational correlation time histograms for htau40 with each dye showing similar distributions even though the htau40-ATTO633 anisotropy histogram (inset) is different from the htau40-ATTO647N histogram.

conjugates (ATTO-TEC, private communication). Upon trapping htau40-ATTO633, the anisotropy histogram (Figure 2-8, inset) appears different from the anisotropy histogram for htau40-ATTO647N (Figure 2-4a), presenting only one broad peak at a lower average anisotropy value. To make a more direct comparison since anisotropy is an inherently non-linear quantity, the anisotropy values were converted to rotational correlation times using the Perrin equation (equation 2-4) and measured values of τ and r_0 (Table 2-2). These histograms were then scaled (each correlation time was divided by the most probable correlation time) so that they were centered at 1 and easily comparable (Figure 2-8).

Table 2-2. Fundamental anisotropy (r_0) and fluorescence lifetime (τ) of samples.

Sample	r_0	τ (ns)
htau40-ATTO647N	0.32	3.1
htau40-ATTO633	0.33	3.1
MTG	0.36	3.5
ATTO647N in 50 % glycerol	0.32	3.4
ATTO633 in 50 % glycerol	0.33	3.4

Though the anisotropy histograms were different, the reduced rotational correlation time histograms show remarkable similarity, including evidence of two distinct solution-phase conformations. Using the Kolmogorov-Smirnov statistical test, we determined that the data for these two samples were not statistically different at the 1 % significance level ($p = 0.0148$) (Figure 2-13).

Though the conclusion of two underlying families of populations is robust across both dyes, it is worthwhile to speculate on the origin of the different anisotropies. One possibility is that the dyes contribute differently to the internal friction of the protein motion. Internal friction has been shown to have an important role in protein conformational dynamics by causing an increase in the roughness of the potential energy landscape, leading to increased reconfiguration times in solution.[43] The sources of internal friction are an active area of research, but charge repulsion and amino acid composition have been shown to contribute.[43] Therefore, an increase in friction between the protein and the ATTO647N dye, possibly due to its higher hydrophobicity, may slow the reconfiguration time enough to better resolve the two populations of conformers in htau40-ATTO647N. For example, molecular dynamics have shown that large amplitude motions that interconvert between different dye “resting positions” may contribute to observed anisotropy decays, and the timescale of this decay is expected to be influenced by the details of the interaction between the dye and the protein.[40] That both histograms have a conspicuous shoulder in the reduced rotational correlation time histograms implies that the difference in the samples due to labeling is subtle and the bimodality of the htau40-ATTO647N anisotropy histogram is not primarily due to dye-

protein interactions. This picture of internal friction is also consistent with the time-resolved decays of htau40 with different dyes both showing three different decay components and similar cone angles (Figure 2-9, Table 2-3). Ultimately, these experiments suggest an underlying distribution of protein conformations with both labels.

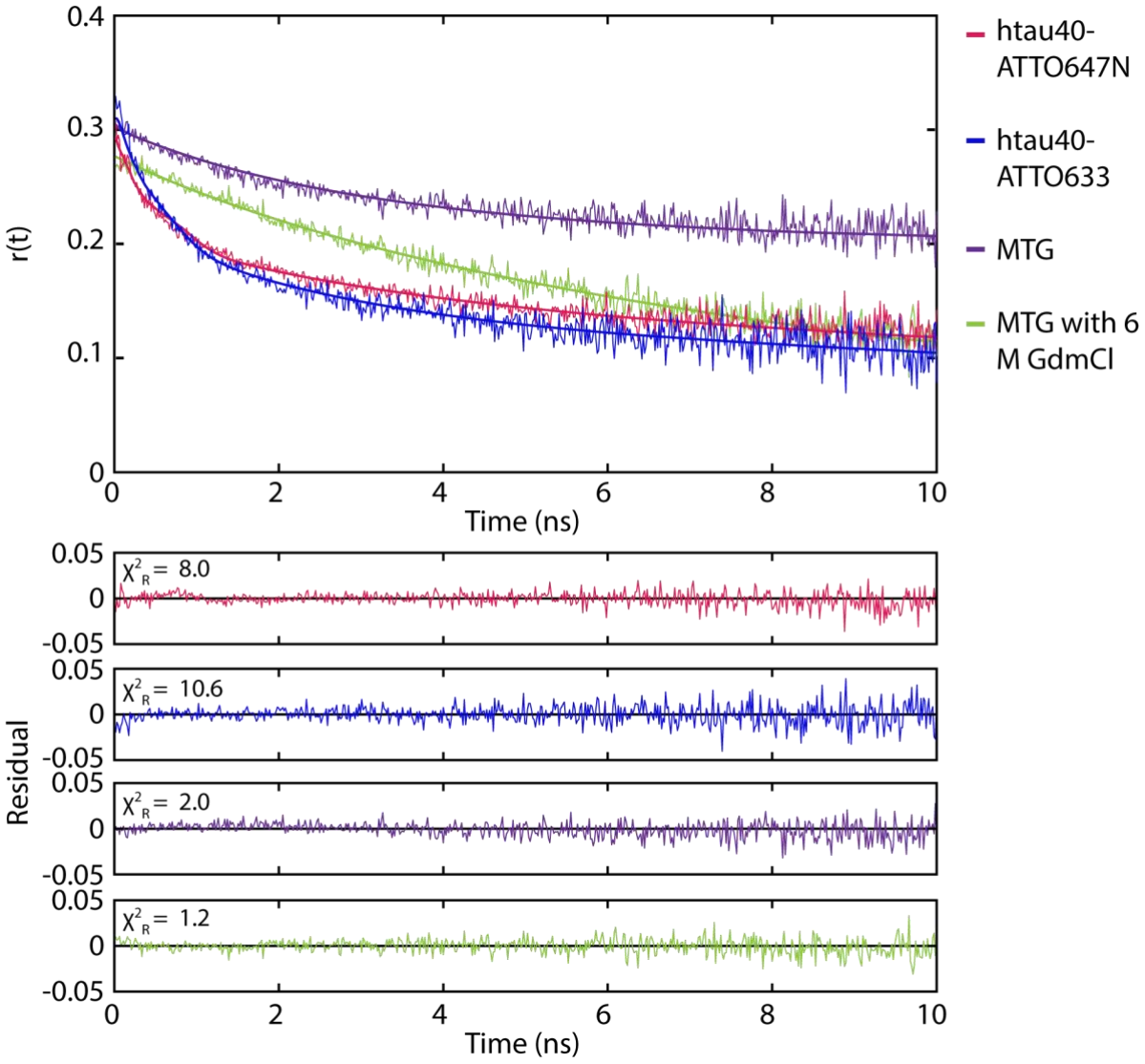

Figure 2-9. Time-resolved anisotropy of htau40-ATTO647N (magenta), htau40-ATTO633 (blue), MTG (purple), MTG with 6 M GdmCl (green). χ^2_R is the reduced χ^2 value for the fit shown. Anisotropy fit parameters are given in Table 2-3.

*2.3.6 **Time-resolved anisotropy of protein samples***

The protein anisotropy decays are fit to equations given in the Data Analysis section (see 2.6.12.2). Fitting parameters can be found in Table 2-3. The reduced χ^2 values shown in Figure 2-7 and Figure 2-9 were calculated as described in the Data Analysis section. While the reduced χ^2 values for the fits of MTG and denatured MTG approach 1, suggesting the two-component model completely describes MTG's behavior, the reduced χ^2 values for the htau40 samples are 8.0 and 10.6 for htau40-ATTO647N and htau40-ATTO633, respectively, even as the fits qualitatively capture the data. The minimum obtainable reduced χ^2 value depends on the ability of the chosen model to capture the observed behavior. Therefore, the choice of the cone-in-a-cone model for htau40 samples is likely a slight oversimplification of the motion. This modest deficiency is not surprising, as the IDP is large and may have many segmental motions with overlapping timescales. However, though the IDP has a large number of degrees of freedom, the fits qualitatively capture the decay dynamics, and thus the cone-in-a-cone model accurately captures the dominant behaviors of the IDP.

Table 2-3. Average ± standard deviation of the mean for fitting parameters of the time-resolved anisotropy decays.

Sample	ϕ_f (ns)	ϕ_i (ns)	ϕ_s (ns)	S_f^2	S_i^2	τ (ns)	θ_f (°)	θ_i (°)
htau40–ATTO647N	0.25 ± 0.04	5.3 ± 0.6	118 ± 4	0.67 ± 0.02	0.65 ± 0.03	3.244 ± 0.006	29 ± 1	30 ± 2
htau40–ATTO633	0.20 ± 0.02	2.5 ± 0.2	107 ± 2	0.54 ± 0.05	0.55 ± 0.04	2.6 ± 0.1	36 ± 3	35 ± 2
MTG	1.9 ± 0.6	--	90 ± 40	0.65 ± 0.04	--	3.22 ± 0.03	30 ± 2	--
MTG with 6 M GdmCl	4.3 ± 0.7	--	19 ± 3	0.70 ± 0.06	--	3.643 ± 0.009	27 ± 3	--
ATTO647N in 50 % glycerol	3.2	--	--	--	--	3.6	--	--
ATTO647N in 80 % glycerol	27	--	--	--	--	3.8	--	--

2.3.7 Reduced rotational correlation time of htau40 and MTG in 6 M GdmCl

We converted the anisotropy histograms in Figure 2-4c and Figure 2-4d into reduced rotational correlation time plots (Figure 2-10). These plots show that the denatured proteins have a slight shoulder in reduced rotational correlation time space, but it is not nearly as pronounced as that seen for htau40-ATTO647N or htau40-ATTO633 without denaturant (Figure 2-8).

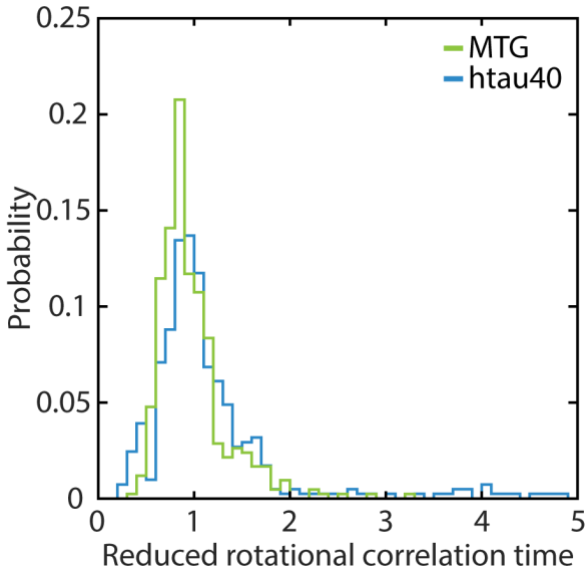

Figure 2-10. Reduced rotational correlation time of denatured htau40 and MTG. Both samples are prepared in 25 % glycerol with 6 M GdmCl.

2.4 Discussion

2.4.1 Understanding the origin of single-molecule heterogeneity

Using the single-molecule and time-resolved data presented in Figure 2-4 and Figure 2-6, we can understand the origins of the bimodal anisotropy distribution for htau40. That a bimodal distribution is observed only in htau40 and not the other samples suggests root causes specific to the IDP. One possibility is that hydrophobic interactions between the dye and protein result in this bimodal distribution.[41] However, several pieces of evidence suggest such interactions are not the origin. First, molecular dynamics

simulations have shown that fluorescent dyes generally track the motions of their proximal residues.[40] Second, when hydrolyzed ATTO647N is mixed with unlabeled htau40 (mutant with no cysteine residues), the bulk anisotropy of the dye is not altered, indicative of an absence of strong hydrophobic interactions (see 2.3.4). Third, when replacing ATTO647N with the less hydrophobic ATTO633 (see 2.3.5), the time-resolved anisotropy shows that both have three qualitatively similar component decays (Figure 2-9). Fourth, and perhaps most compelling, although the ATTO633-labeled htau40 does not show two conspicuous peaks (Figure 2-8, inset), the distribution of anisotropies is broad and asymmetric, and analysis of the underlying rotational correlation times reveals a bimodal distribution for the ATTO633-labeled sample that is strikingly similar to the bimodal distribution for the ATTO647N-labeled sample (Figure 2-8), and the distributions of both dye-labeled samples imply two populations (Figure 2-13). Thus, even as the specific distribution of observed anisotropies is sensitive to the hydrophobicity of the dye (see 2.3.4), the existence of two underlying populations of protein conformations is confirmed by observation of two populations of reduced correlation times for both labels and is thus independent of the label and intrinsic to the protein.

We can examine the role of the five parameters (ϕ_f, ϕ_i, ϕ_s, θ_f, and θ_i) that could cause the observed partitioning into the two anisotropy populations, with an upper anisotropy $r_U = 0.21$ and a lower anisotropy of $r_L = 0.17$ (two peaks in Figure 2-4a), observed in our single-molecule experiments. For each parameter, we examine how reasonable it is for the average value from the bulk anisotropy to be distributed among an upper and lower population needed to generate the two steady-state anisotropy peaks. Partitioning of the fast component of the decay (0.25 ns) could cause the population centered at $r_U = 0.21$ if the upper value, $\phi_{f,U}$, were 0.69 ns, but not even a value of 0 ns for the lower value, $\phi_{f,L}$, could account for the peak at $r_L = 0.17$. Thus, partitioning in ϕ_f cannot account for the observed single-molecule behavior. Similarly, ϕ_i and ϕ_s would have to change dramatically to account for the bimodal distribution of htau40, with ϕ_i partitioning from 5.3 ns into lower and upper values of 1.1 ns and 10.5 ns and ϕ_s partitioning from 118 ns into values of

11.3 ns and over 1 μs. This spread is extremely large, as even attachment to binding partners and consequent increase in rigidity only results in slowing of segmental motions by a factor of six,[37] suggesting an alternative explanation is necessary.

A change in cone angle is thus a more likely origin of partitioning. A split from 29° for the cone half-angle of the dye motion (θ_f) into 27° and 35° could cause this partitioning. Alternatively, the 30° cone half-angle of the protein segmental motion (θ_i) could split into 22° and 49° in order to account for this observation. Thus, even as very large changes in timescale of rotational decay are required for partitioning, even subtle changes in θ_f could more reasonably achieve the same effect, making fluorescence polarization anisotropy essentially an amplifier of a small conformational change. Consequently, we ascribe the partitioning of steady-state anisotropies into two solution-phase populations with different cone angles, though we are unable to decipher which one is the root cause.

Since htau40 is an IDP, it is expected to have a variety of conformations, yet we illustrate through single-molecule fluorescence anisotropy that these solution-phase conformations partition into two families of stable conformers. These families are distinguished by a change in cone angle explored by the fluorescent probe and proximal protein segment, suggesting a more compact family and a less compact family. That these families were not observed in freely-diffusing single-molecule FRET experiments[15] suggests that the conformational changes are fairly subtle, highlighting two notions: 1) that anisotropy and FRET are complementary techniques that may be sensitive to different structural differences and 2) that a critical benefit of higher photon counts due to a prolonged trapping time is a reduced contribution of shot noise, allowing resolution of smaller structural differences.

One possible interpretation of our finding is that one family may be more prone to pathological aggregation, and thus a preferred intermediate. Less compact structures, including those induced by binding to heparin[15] or caused by mutations,[44] expose the MTBR region, facilitating inter-molecular contacts. Alternatively, the Alz-50 configuration, recognized by Alz-50 antibodies, has the N-terminus

blocking the MTBR region. This spatial arrangement is observed in tau paired helical filaments, but is believed to be a precursor to aggregation.[45] Observation of a more compact solution-phase structure of tau may also be related to the solution-phase presence of this species. Additional experiments to further characterize these solution-phase conformers are ongoing and will be necessary to definitively determine the nature and biological role of these species. However, use of a new single-molecule method for IDPs to identify and begin to characterize these families of monomer conformations is a critical step toward understanding the first stages of the htau40 aggregation pathway that leads to disease.

2.4.2 Estimates of global motions

We assigned the longer time component of MTG, ϕ_s=90 ns to global motion. One can calculate the rotational correlation time for the global motion of MTG assuming it is a sphere, using the Stokes-Einstein-Debye equation,[46]

$$\phi = \frac{\eta V}{k_B T} \qquad \text{(equation 2-1)}$$

where *T* is the temperature in K, k_B is the Boltzmann constant, η is the viscosity, and *V* is the hydrodynamic volume. One can further relate the hydrodynamic volume to the molecular weight of the protein to yield,

$$\phi = \frac{(\eta M)}{k_B T}(v + h) \qquad \text{(equation 2-2)}$$

where v is the specific volume and is near 0.73 mL/g for proteins, and *h* is the hydration and is around 0.23 g water per g protein. Since MTG is slightly asymmetric, estimates using the different radii of MTG[34] (and assuming a somewhat larger hydrodynamic radius than crystallographic radius) or using the molecular weight result in correlation times ranging from 30 – 120 ns in 25 % glycerol, consistent with our observed value of 90 ns.

An estimate of the global motion for htau40 is more difficult to assess. Use of (equation 2-1) and (equation 2-2) will provide lower limits, as the IDP exhibits a significantly smaller degree of compaction.

Further, existing estimates of htau40 geometry[14] suggest a prolate ellipsoid model would provide a more realistic estimate. A hydrated prolate ellipsoid of molecular weight 50,000 is expected[46] to exhibit three decay timescales on the order of ~20 ns, ~50 ns, and ~90 ns, though these are likely all significant underestimates as the hydration of the IDP is expected to be significantly higher than a globular protein that has undergone hydrophobic collapse and the compaction is expected to be substantially lower. A less undervalued estimate can be made by examining a protein of molecular weight 100,000,[46] which suggests decay time scales of ~40 ns, ~90 ns, and ~200 ns, though these values are still likely undervalued. While the intermediate and slower motions are sensitive to the precise shape of the ellipsoid, they are likely all too long to be contributing here. On the other hand, the shortest timescale is relatively independent of this parameter. Thus, our longest observed decay time, ϕ_s = 90 ns, could be a segmental motion of the IDP, but could also be the faster global motion component.

2.5 Conclusion

There is an outstanding need for a molecular understanding of the earliest steps of tau conformational change and aggregation, even as substantial progress is being made understanding later steps in the process for tau[7, 29] and other IDPs.[28] Our approach can potentially satisfy this need — both for tau and other IDPs — by providing increased observation time, which has allowed us to differentiate between two families of long-lived conformations adopted by tau protein in solution by their degree of compaction. Further, fluorescence polarization anisotropy can be combined with other complementary probes to maximize information content,[23, 47] all while trapping molecules in solution.

2.6 Experimental Section

2.6.1 Plasmid constructs

The construction of htau40 with natural cysteines replaced by serines (C291S and C322S) and a Y310C mutation, for subsequent thiol maleimide labeling, was described previously.[13]

2.6.2 Protein expression and purification

Transformation of the pET28 vector into *E.coli* BL21 (DE3) was performed by heat shock according to manufacturer's instructions (Agilent Technologies). The purification was an adaption of published procedures.[13, 48] Briefly, overnight cultures of transformed *E.coli* were diluted 1:100 with fresh LB broth (20 mg kanamycin/L) and grown at 37 °C with agitation until OD_{600nm}= 0.8 – 1.0. Expression was induced with 1 mM IPTG (Gold Biotechnology) and bacteria were incubated for 3.5 h at 37 °C with agitation. Cells were sedimented at 5,000 x g for 10 min, resuspended in 20 mM piperazine-N,N'-bis(ethanesulfonic acid (PIPES – JT Baker) pH = 6.5, 500 mM NaCl, 5 mM ethylenedinitrilotetraacetic acid (EDTA – JT Baker), and stored at –80 °C. Protein extraction was initiated by incubating the bacterial suspensions for 20 min at 80 °C and sonicating them for 1 min on ice using a tip probe (Fisher). The lysed cells were then sedimented at 5,000 x g for 30 min at 4 °C. Tau was precipitated from the supernatants by addition of 55 % (w/v) ammonium sulfate (VWR) followed by incubation at room temperature for 2 h. The samples were centrifuged for 10 min at 20,000 x g and protein pellets taken up in nanopure water supplemented with 4 mM DTT (Gold Biotechnology). Solutions were sonicated on ice and syringe filtered (Pall Acrodisc 0.45 µm). Protein was then loaded onto a Mono S 10/100 GL (GE Healthcare) cation exchange column using an ÄKTA system (GE Healthcare) with 20 mM PIPES pH 6.5, 50 mM NaCl and 0.5 mM EDTA and eluted with a linear gradient of 20 mM PIPES pH 6.5, 1 M NaCl, 0.5 mM EDTA. Fractions containing tau protein were determined using SDS-PAGE and Coomassie R-250 (Amresco) staining. Pooled protein was further purified via size

exclusion chromatography (Superdex S200, GE Healthcare) and precipitated overnight in 1:1 protein:methanol (Fisher Optima grade) supplemented with 4 mM DTT. Protein pellets were collected and stored at –80 °C until further use.

2.6.3 Protein labeling

Methanol was removed and pellets taken up in 8 M guanidinium HCl (Thermo Fisher Scientific). Proteins were labeled for 2 h with ATTO647N or ATTO633 (ATTO-TEC GmbH) using a 10-fold molar excess of dye over protein. Residual dye was reacted with 2-mercaptoethanol and removed by passage over a PD-10 column (GE Healthcare) equilibrated with 10 mM 2-[4-(2-hydroxyethyl)piperazin-1-yl]ethanesulfonic acid (HEPES) pH 7.4 and 100 mM NaCl. Protein concentration was determined by BCA assay (Pierce) using manufacturer's instructions in a Cary Bio100 UV Spectrophotometer. Proteins were determined to have a purity of >99% based on SDS-PAGE and Coomassie staining. Aliquots were snap frozen in liquid nitrogen and stored at –80 °C.

2.6.4 Glycerol purification for single-molecule experiments

Glycerol from various companies showed fluorescent impurities that impeded our ability to accurately trap single molecules of interest. We purified glycerol (JT Baker, Avantor) by extracting impurities into 2,2,4-trimethylpentane (Fisher Scientific). We performed the extraction three times, then the glycerol was stirred at 110 °C for 1 h to remove remaining 2,2,4-trimethylpentane. The purified glycerol was then put into a home-built photobleaching apparatus[49] for 3 days to photobleach remaining fluorescent impurities. This purified glycerol was used in all single-molecule experiments. To ensure that the glycerol was pure enough for experiments, we analyzed a solution of 25 % glycerol and 75 % buffer (10 mM phosphate buffer pH 6.9 and 100 mM NaCl) using our same single-molecule trapping protocol used for all

data acquisition. No trapping events were noted, and the glycerol was deemed pure for single-molecule experiments.

2.6.5 Sample preparation

All samples were prepared in a buffer of 100 mM NaCl, 10 mM phosphate buffer (pH 6.9), saturated trolox (6-hydroxy-2,5,7,8-tetramethylchroman-2-carboxylic acid)[50] and 25 % v/v glycerol (unless otherwise noted). The protocatechuic acid (PCA)/ protocatechuate-3,4-dioxygenase (PCD) oxygen scavenging system was also used for single-molecule experiments,[51] and were prepared as previously described.[52] Immediately before analysis, 0.5 units PCD and 2.5 mM PCA, final concentration, were added to the samples. The maleimide-functionalized ATTO647N dye was hydrolyzed before use by diluting to 5 µM in 10 mM phosphate buffer, pH 6.9, and stored at 4 °C overnight.[42] For single-molecule experiments, the protein and dye samples were diluted to low pM concentrations. For bulk fluorimeter experiments, the samples were prepared at 625 nM final concentrations. For time-resolved anisotropy measurements, samples were prepared at 1 µM final concentration.

2.6.6 Anti-Brownian electrokinetic (ABEL) trap fabrication

ABEL trap microfluidic devices were fabricated as previously described (Figure 2-11).[53] Briefly, ABEL traps were fabricated on GE-124 4" quartz wafers. In the initial step, approximately 500 nm of polysilicon was deposited onto the wafer using low pressure chemical vapor deposition at 680 °C. Contact photolithography was used to define the reservoirs (MicroChem, S-1800 series photoresist, Karl Suess MA6 Contact Aligner, ~10.0 mJ/cm^2 at 365 nm). The reservoirs were first etched into the polysilicon layer using an SF_6/O_2 plasma etch (Plasmatherm 770 ICP; 25 sccm O_2; 25 sccm SF_6; 7 mTorr pressure; 50W RIE and 500W ICP; ~90 nm/min), and the pattern was transferred into the quartz substrate using a 6:1 buffered oxide etchant (hydrofluoric acid). The reservoirs were etched into the quartz to a depth of 10.5 µm at an

etch rate of 90 nm/min in a recirculation tank. Once the reservoirs were etched, a second round of lithography was done to define the traps (MicroChem, SPR 220-7 photoresist, Karl Suess MA6 Contact Aligner, 405 nm, ~300 mJ/cm^2). Before exposure, the traps were exactly aligned to the center of the reservoirs. The same polysilicon plasma etch that was used to etch the reservoirs was used to etch the traps into the polysilicon layer. Then, the traps were etched into the quartz layer using a CHF_3/O_2 plasma etch to a depth of 1 µm (20 sccm O_2; 50 sccm CHF_3; 100 mTorr pressure; 150 W RIE; 16 nm/min), measured using profilometry. After the reservoirs and the traps were etched into the wafer, the remaining polysilicon was

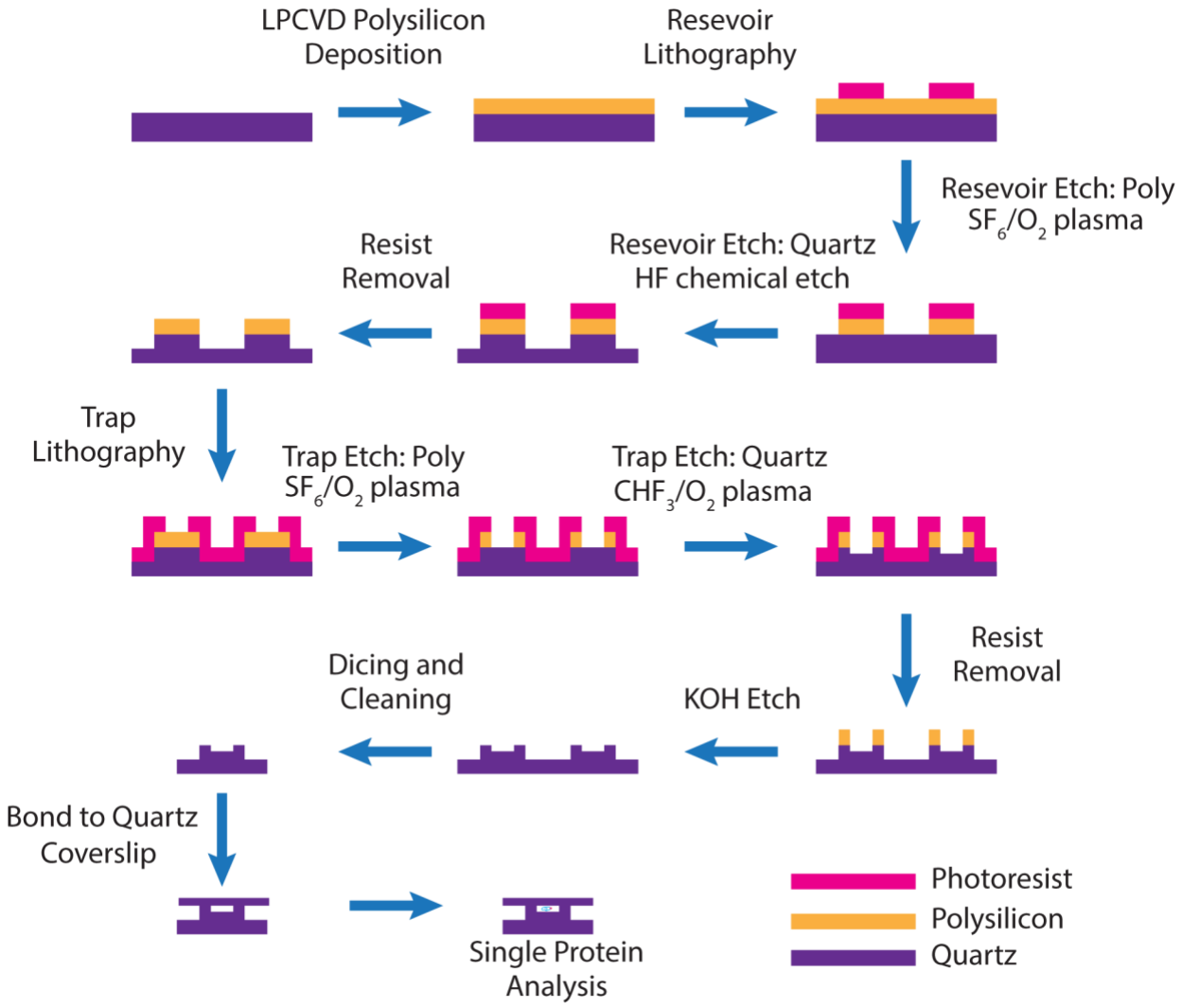

Figure 2-11. Fabrication scheme for the ABEL trap microfluidic device.

stripped using a potassium hydroxide etch (36 % KOH; 70 °C; 5 minutes). The wafer was then diced into chips containing individual ABEL trap devices. Traps had to be bonded to a glass plate with CrystalBond509 as they do not adhere well to standard tacky mat. Before dicing, a layer of S1800 photoresist was applied to protect the traps from particles generated during the dicing process. The photoresist was removed by soaking overnight with acetone and 5 % Triton-X 100. Fabricated devices and fused quartz coverslips (R525025, Esco Optics) were rinsed with HPLC grade acetone, isopropanol, ethanol and nanopure water before being soaked in 40 % wt. KOH at 70 °C for 2 min. Then, 100 µL of 70 % sodium silicate solution (JT Baker) was deposited on the coverslip and spun–coated at 4000 rpm for 25 s. The sodium silicate covered coverslip was then pressed onto the fabricated piece and annealed at 90 °C for 15 min, followed by 15 °C temperature increase every 15 min until 200 °C, where the pieces were bonded overnight.[54]

2.6.7 ABEL trap preparation

The microfluidic ABEL trap was cleaned based on published procedures.[55] Briefly, the trap was cleaned in a UV-ozone cleaner (Novascan Technologies) for 30 min then sonicated in 1 M KOH for 30 min. The trap was then rinsed thoroughly with ultrapure water and dried with a dry stream of N_2. Solutions of 1 mg/mL polyethyleneimine (PEI), pH 8.0 (MilliporeSigma), and 1 mg/mL polyacrylic acid (PAA), pH 8.0 (MilliporeSigma), were prepared and filtered with a 0.2 µm syringe filter.[56] The interior surface of the trap was then passivated with alternating layers of these solutions of PEI and PAA, as previously described.[55, 57] Briefly, PEI was injected into the trap and allowed to sit for 10 min, at which time the trap was blown dry with dry N_2, rinsed with ultrapure water then blown dry again. This process was repeated with PAA. A total of 4 layers, ending in PAA, produced a well-coated interior trap surface that prevented non-specific adsorption of molecules.

*2.6.8 **ABEL trap setup***

A 639 nm diode laser (LDH-D-C-640, PicoQuant, Berlin, Germany) in continuous-wave mode was directed through two orthogonal acousto-optic beam deflectors (MT110-B50A1.5-VIS, DDSPA-B8b15b-0, AMPA-B-30, AA Opto-Electronic, Orsay, France), producing a two-dimensional grid at the sample plane. The excitation beam passed through a 609/54-25 nm bandpass filter (FF01-609/54-25; Semrock), a $\lambda/2$ waveplate (AHWP05M-600; Thorlabs) and a linear polarizer (10GL08AR.14; Newport) immediately before the back of the objective to ensure vertical polarization. The vertically polarized light was focused (0.66 μm^2, ~30 μW) onto the sample plane via a 60x CFI Plan Apo Lambda oil-immersion objective (NA 1.4) (Nikon) mounted on a Nikon Eclipse Ti-U inverted microscope, and the emission was collected through the same objective. The emission passed through a 635 nm dichroic beamsplitter (Di02-R635-25x36; Semrock), a 635 nm long-pass filter (BLP01-635R-25; Semrock), a 200 μm pinhole (Newport Corporation) and a 785 nm short-pass filter (SP01-785RU-25; Semrock). Emission then passed through a polarizing beamsplitter (PBS252, Thorlabs) and was detected on two τ-SPAD single photon counting modules (PicoQuant). A microfluidic trap was placed on the microscope with 4 platinum electrodes arranged along the cardinal directions to allow for control in the X and Y directions. The molecule is trapped in the Z-dimension by the depth of the trap (1 μm).

The focused laser is deflected to a two-dimensional grid of 32 points using a pair of acousto-optic beam deflectors. The beam is scanned across those 32 points in a Knight's Tour pattern. Kalman filtering is applied as described previously,[58-59] and feedback voltages are calculated and applied once every 25 μs. Before trapping, however, these points must be correctly positioned so that each is $\sim \frac{1}{e}$ from adjacent points and the time-averaged intensity profile is homogeneous. A 200 nm fluorescent bead (F8807, Thermo Fisher Scientific) is positioned using an nPoint piezo-electric positioning stage and the deflection location is adjusted to maximize fluorescent signal, thereby ensuring that the excitation spot is properly located. Once the positions have all been established, the intensity of each spot can be adjusted to ensure homogeneous

intensity across the pattern. Finally, feedback voltages can be calibrated to induce the appropriate flows to cancel Brownian motion.

2.6.9 ***Bulk steady-state anisotropy measurements***

Bulk anisotropy measurements were performed on an ISS PC-1 Photon Counting Spectrofluorimeter. The samples were excited in an ultra micro quartz cuvette (105-252-85-40; Hellma Cells, Inc.) with 590 nm excitation and a 590/10 nm band-pass excitation filter. The emitted fluorescence was collected through a 645/75 nm band-pass emission filter.

2.6.10 ***Bulk time-resolved anisotropy measurements***

The bulk sample was contained in a perfusion chamber (Grace Bio-Labs) on a methanol rinsed and O_2 plasma cleaned (300 W, 3 min) glass coverslip (Fisher Scientific). Samples were analyzed using the same experimental setup as was used for ABEL trap experiments above, with the laser in pulsed mode with a repetition rate of 1 MHz or 10 MHz. The anisotropy decays of free ATTO647N dye fit to single exponential decays with lifetimes slightly longer than those reported for the same dye in 10 % glycerol.[42] The time-correlated single photon counting data from the two τ-SPAD detectors was passed through a PHR 800 router (PicoQuant) to a PicoHarp 300 (PicoQuant) time-correlated single photon counting module with a time resolution of 64 ps. The instrument response function was ~400 ps full width at half maximum.

2.6.11 ***Determination of G factor***

To determine the G correction factor for our system, we recorded the time-resolved fluorescence decay of oxazine 720 in water because its reorientation dynamics have been studied previously.[60] We integrated both the parallel and perpendicular decays and determined the G factor necessary to achieve the literature value for steady-state anisotropy for oxazine 720.[61] We did not find it necessary to include

any other correction factor to account for the high NA of the objective,[62] likely because we were not filling the objective with the excitation beam. Typical G factors ranged from 1.04 to 1.07.

2.6.12 Data analysis

2.6.12.1 *Analysis of trapping data and steady-state anisotropy*

Data was analyzed with custom Matlab (MathWorks) routines. Recorded photon counts from the τ-SPAD detectors were binned every 10 ms for analysis of the trapping data. Trapping events were identified by a change point finding algorithm[63-64] that analyzed the total fluorescence intensity and then the average intensity level between change points was used for further analysis.

Steady state anisotropy is calculated per:

$$r = \frac{I_{||} - G \times I_{\perp}}{I_{||} + 2 \times G \times I_{\perp}} \qquad \text{(equation 2-3)}$$

where $I_{||}$ is the emission detected that is polarized parallel to the excitation source, $I_{\perp}$ is emission polarized perpendicular to the excitation, and G is a correction factor determined for the system (see below).[46]

The rotational correlation time, ϕ, is defined as:

$$\phi = \frac{r\tau}{r_0 - r} \qquad \text{(equation 2-4)}$$

where τ is the lifetime of the fluorophore and r_0 is the fundamental anisotropy, experimentally determined from a Perrin plot of anisotropy^{-1} vs. viscosity^{-1} for each sample. The lifetimes were determined by fitting time-resolved fluorescence decays. Values of r_0 and τ are given in Table 2-2 for each sample.

Trapping events were analyzed further and included in the final histograms if (1) they were longer than 500 ms in duration and (2) the anisotropy of the event was less than or equal to the fundamental anisotropy of the sample. A third criterion (3) involves the total applied voltage during the trapping event. Since Brownian motion is random, the total integrated voltage (applied in 25 μs bursts) along each axis should be zero. In practice, small offset voltages can make this number non-zero. However, sticking events,

more often seen when polyelectrolyte layers are not used, are made conspicuous by prolonged non-zero voltages in the same direction (as the trap tries to compensate for the fixed position), resulting in significant deviations from zero. We found that a threshold of |2.5 V·s| was sufficient to filter out any nonspecific sticking events during which a constant voltage would be applied selectively in one direction. Thus, a small minority of trapping events that showed an integrated total voltage outside of the range of –2.5 V·s and 2.5 V·s were eliminated from the analysis.

2.6.12.2 *Time-resolved anisotropy decays*

For time-resolved fluorescence decays, the instrument response function, as measured from scattering the excitation beam off of a coverslip that contained a reservoir of buffer solution, was convoluted with the intensity decays (described below) in order to account for the excitation profile.[65] The model fit the polarized decay curves, $I_{//}(t)$ and $I_{\perp}(t)$, simultaneously using a least squares estimate according to:[46]

$$I_{||}(t) = \frac{1}{3} I(t)[1 + 2r(t)] \qquad \text{(equation 2-5)}$$

$$I_{\perp}(t) = \frac{1}{3} I(t)[1 - r(t)] \qquad \text{(equation 2-6)}$$

where *r(t)* is the multi-exponential decay describing wobbling-in-a-cone or cone-in-a-cone behavior with one or two local motions,[38-39] and S_F^2 and S_I^2 are the squared order parameters and indicate the extent to which the motion is restricted:

$$\frac{r(t)}{r_0} = (1 - S_F^2) e^{-t\left[\frac{1}{\phi_f} + \frac{1}{\phi_s}\right]} + S_F^2 e^{-\frac{t}{\phi_s}} \qquad \text{(equation 2-7)}$$

for a biexponential anisotropy decay or

$$\frac{r(t)}{r_0} \cong (1 - S_F^2) e^{-\frac{t}{\phi_f}} + S_F^2 (1 - S_I^2) e^{-\frac{t}{\phi_i}} + S_I^2 S_F^2 e^{-\frac{t}{\phi_s}} \qquad \text{(equation 2-8)}$$

for a triexponential anisotropy decay. Assuming reorientation of the dye transition dipole is confined within a cone of half-angle, θ_c, then θ_c can be determined by:[38, 66]

$$\frac{r_\infty}{r_0} = S^2 = \left[\frac{1}{2}\cos\theta_c\,(1+\cos\theta_c)\right]^2 \qquad \text{(equation 2-9)}$$

where r_∞ is the residual anisotropy. After the individual decays are fit, the time-resolved anisotropy decay is calculated according to:

$$r(t) = \frac{I_\parallel(t) - I_\perp(t)}{I_\parallel(t) + 2\times I_\perp(t)} \qquad \text{(equation 2-10)}$$

This provides the anisotropy decay curves as shown in Figure 2-6, Figure 2-7 and Figure 2-9. We can calculate the steady-state anisotropy from time-resolved anisotropy parameters by:[46]

$$r = \frac{\int_0^\infty I(t)r(t)dt}{\int_0^\infty I(t)dt} \qquad \text{(equation 2-11)}$$

where *I(t)* is the exponential decay of fluorescence intensity and *r(t)* is given in equation 2-7 or equation 2-8. Though such cone-in-a-cone models are common in the biophysical literature, it is important to state that non-idealities in dye motion (i.e. motion beyond simple cone exploration), may result in an overestimation of the derived protein cone angle.[40] The reduced χ^2 value (χ^2_R) was calculated to assess the goodness of fit.[65]

$$\chi^2_R = \frac{1}{2(N_2 - N_1 + 1) - n}\sum_{i=N_1}^{N_2}\left[\frac{\left(I_\parallel^O(i) - I_\parallel^C(i)\right)^2}{I_\parallel^O(i)} + \frac{\left(G*I_\perp^O(i) - I_\perp^C(i)\right)^2}{I_\perp^O(i)}\right] \qquad \text{(equation 2-12)}$$

where $I_\parallel^O$ is the observed intensity decay in the parallel channel, $I_\parallel^C$ is the fit curve in the parallel channel, $I_\perp^O$ is the observed intensity decay in the perpendicular channel, $I_\perp^C$ is the fit curve in the perpendicular channel, *G* is the G factor for the system, and N_1 and N_2 are the first and last bins considered in the analysis.

For the htau40 anisotropy decays, the parameter space that needed to be explored was large and finding local minimums that did not provide a calculated *r(t)* curve that aligned with the experimental *r(t)* curve was common. The parameters were therefore constrained so that ϕ_f was between 0 – 2 ns, ϕ_i was

between 1 – 20 ns and ϕ_s was between 50 – 150 ns. While the code was not able to freely scan the entire parameter space, and therefore may not have found the global minimum, it did provide an *r(t)* curve that looked to fit the data.

2.6.12.3 *Analysis of anisotropy changing during trapping event*

To determine whether the anisotropy of the molecule changed within a single trapping event, we changed the method of finding change points in our data. Instead of analyzing the total intensity for change points, we analyzed the parallel and perpendicular intensity independently for change points. We found that about 2 % of the trapping events showed a transition between anisotropy values. Of the 2 % that showed the transition, 75 % were transitions to or from an outlier anisotropy value. This makes about 0.5 % of trapping events plausible conversions between populations, so we concluded that the conformations are likely stable.

2.6.12.4 *Reduced rotational correlation time plots*

Anisotropy histograms of simulated data at various average anisotropy values are converted to reduced rotational correlation time histograms to illustrate the conversion process (Figure 2-12). If a single Gaussian is used to generate an anisotropy histogram, the reduced rotational correlation time histograms are also Gaussian. However, Gaussians of equal width in the anisotropy histogram will have slightly different widths in the reduced correlation time histogram due to the nonlinearity of the transformation between the two. This nonlinearity is the reason why the two conspicuous peaks in Figure 2-4a become somewhat less conspicuous in Figure 2-8.

2.6.12.5 *Analysis of histogram fit by Kolmogorov-Smirnov test*

Histograms were fit with custom Matlab codes that relied upon a maximum likelihood estimation to fit the histograms to 1, 2 or 3 Gaussian curves. The fitting parameters μ (mean) and σ (standard deviation) of the Gaussian curves were recorded and used as the basis for generating random numbers from a normal distribution ('normrnd' function in Matlab R2016a). Once we had a data histogram and a

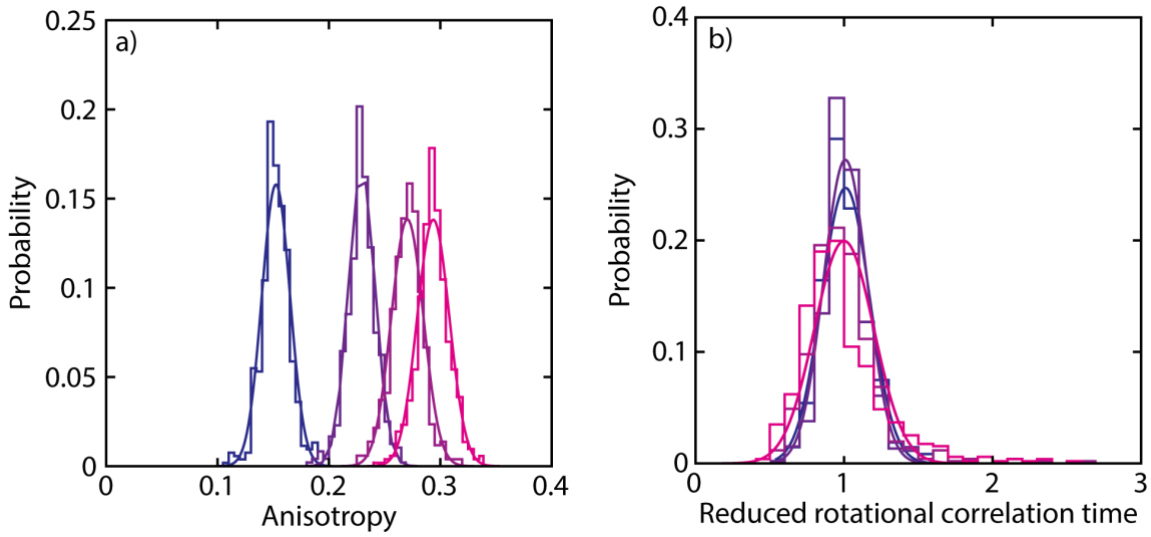

Figure 2-12. Transforming simulated anisotropy histograms to reduced rotational correlation time histograms.

simulated histogram from the fitting parameters (with one or two component Gaussians), we compared them using the two-sample Kolmogorov-Smirnov test ('kstest2' function in Matlab). This test determines whether the data in two vectors are from the same underlying distribution at a particular significance level. We used this analysis to examine histograms of reduced rotational correlation time for htau40-ATTO647N and htau40-ATTO633 (Figure 2-13). We first determined that both reduced rotational correlation time histograms must each be fit with a double Gaussian simulation since the Kolmogorov-Smirnov test fails to reject the null hypothesis at the 1 % significance level (Figure 2-13a, c). When these histograms were fit with a single Gaussian, the p-values indicate a rejection of the null hypothesis at the 1 % significance level (Figure 2-13b, d). We therefore conclude that the distributions of reduced rotational correlation times contain 2 underlying populations.

We then tested the validity of using a 2-component Gaussian fit of the htau40-ATTO647N anisotropy histogram (Figure 2-4a) rather than a 3-component Gaussian fit (Figure 2-14). For the comparison of a double Gaussian simulation with the htau40-ATTO647N data, we find a p-value of 0.13 and with a triple Gaussian simulation the p-value is 0.15. For both tests, we fail to reject the null hypothesis

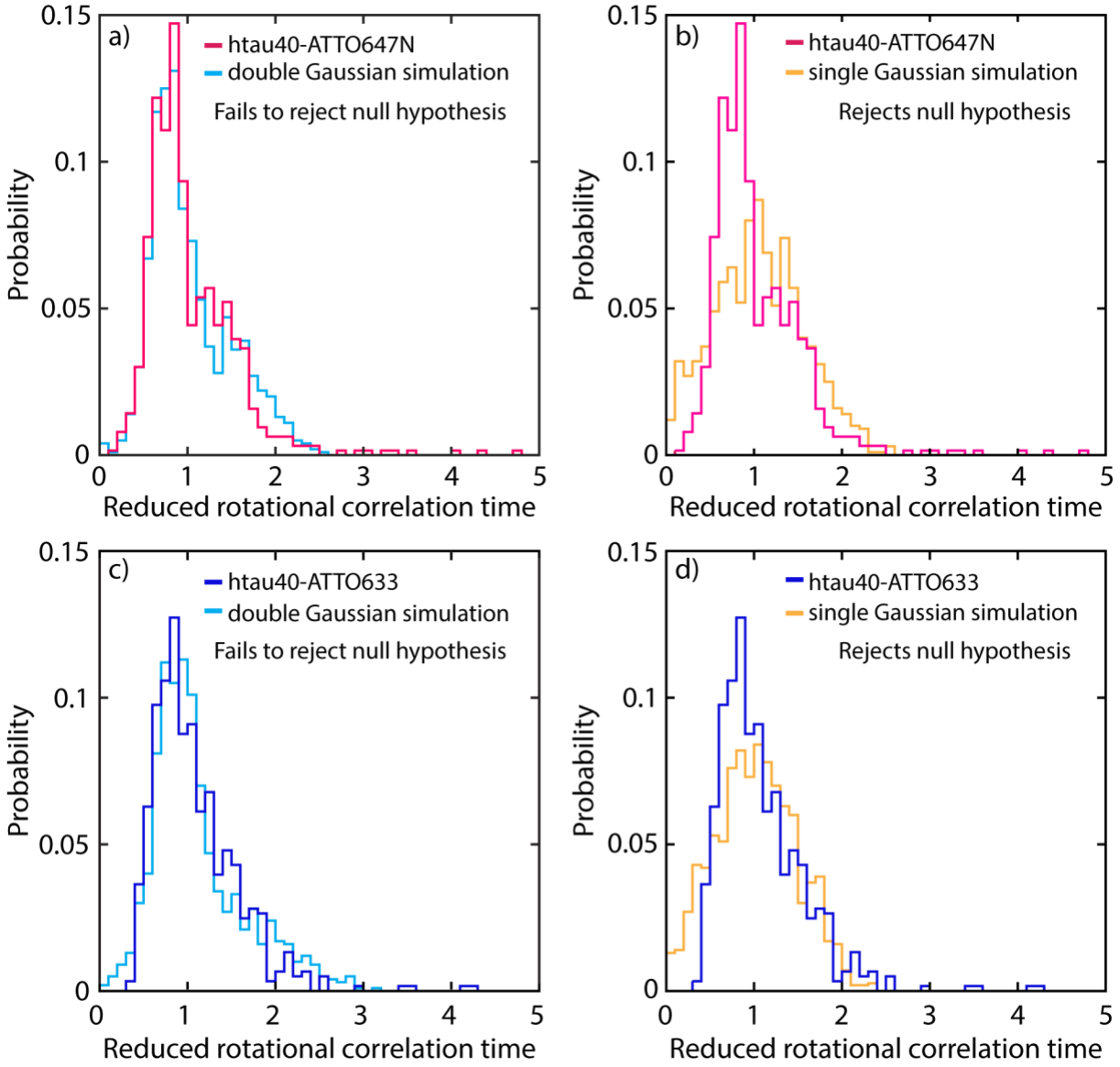

Figure 2-13. Kolmogorov-Smirnov test assesses whether the fit reflects the data. (a) htau40-ATTO647N fit with a double Gaussian ($\mu_1 = 0.7$, $\sigma_1 = 0.2$; $\mu_2 = 1.3$, $\sigma_2 = 0.5$) and the p-value of 0.53 fails to reject the null hypothesis at the 1 % significance level; (b) htau40-ATTO647N fit with 1 Gaussian ($\mu_1 = 1.0$, $\sigma_1 = 0.6$) and the p-value of 2.8×10^{-6} rejects the null hypothesis at the 1 % significance level; (c) htau40-ATTO633 was fit with a double Gaussian ($\mu_1 = 0.9$, $\sigma_1 = 0.2$; $\mu_2 = 1.5$, $\sigma_2 = 0.6$) and the p-value of 0.12 fails to reject the null hypothesis at the 1 % significance level; and (d) htau40-ATTO633 was fit with 1 Gaussian curve ($\mu_1 = 1.0$, $\sigma_1 = 0.5$) and the p-value of 7.6×10^{-6} rejects the null hypothesis at the 1 % significance level.

at the 1 % significance level and thus determine that the data and simulation likely come from the same underlying distribution. Since the addition of another component in our fit did not dramatically increase our p-value, we decided to continue the analysis with a double Gaussian fit.

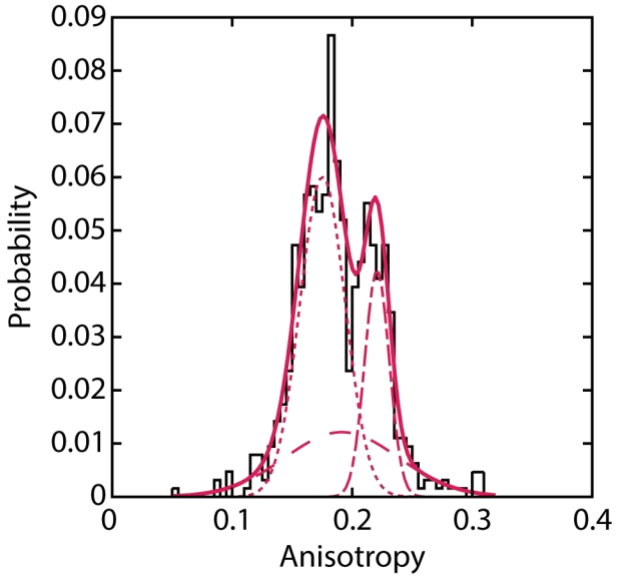

Figure 2-14. Alternative fit of htau40 anisotropy histogram with 3 component Gaussian curves (μ_1 = 0.18, σ_1 = 0.02; μ_2 = 0.19, σ_2 = 0.05; μ_3 = 0.22, σ_3 = 0.01). The p-value of 0.15 fails to reject the null hypothesis at the 1 % significance level. Sample was measured in buffer containing 25 % glycerol.

2.7 References

1. Levy, S. F.; LeBoeuf, A. C.; Massie, M. R.; Jordan, M. A.; Wilson, L.; Feinstein, S. C., Three- and Four-repeat Tau Regulate the Dynamic Instability of Two Distinct Microtubule Subpopulations in Qualitatively Different Manners: Implications for Neurodegeneration. *J. Biol. Chem.* **2005**, *280*, 13520-13528.

2. Mandelkow, E. M.; Mandelkow, E., Tau in Alzheimer's disease. *Trends Cell Biol.* **1998**, *8*, 425-427.

3. Gustke, N.; Trinczek, B.; Biernat, J.; Mandelkow, E. M.; Mandelkow, E., Domains of tau protein and interactions with microtubules. *Biochemistry* **1994**, *33*, 9511-9522.

4. Himmler, A.; Drechsel, D.; Kirschner, M. W.; Martin, D. W., Jr., Tau consists of a set of proteins with repeated C-terminal microtubule-binding domains and variable N-terminal domains. *Mol. Cell. Biol.* **1989**, *9*, 1381-1388.

5. von Bergen, M.; Barghorn, S.; Biernat, J.; Mandelkow, E. M.; Mandelkow, E., Tau aggregation is driven by a transition from random coil to beta sheet structure. *Biochim. Biophys. Acta* **2005**, *1739*, 158-166.

6. Ittner, L. M.; Götz, J., Amyloid-β and tau — a toxic pas de deux in Alzheimer's disease. *Nat. Rev. Neurosci.* **2011**, *12*, 67-72.

7. Fitzpatrick, A. W. P.; Falcon, B.; He, S.; Murzin, A. G.; Murshudov, G.; Garringer, H. J.; Crowther, R. A.; Ghetti, B.; Goedert, M.; Scheres, S. H. W., Cryo-EM structures of tau filaments from Alzheimer's disease. *Nature* **2017**, *547*, 185-190.

8. Crowther, R. A.; Goedert, M., Abnormal tau-containing filaments in neurodegenerative diseases. *J. Struct. Biol.* **2000**, *130*, 271-279.

9. Himmelstein, D. S.; Ward, S. M.; Lancia, J. K.; Patterson, K. R.; Binder, L. I., Tau as a therapeutic target in neurodegenerative disease. *Pharmacol. Ther.* **2012**, *136*, 8-22.

10. Kopeikina, K. J.; Hyman, B. T.; Spires-Jones, T. L., Soluble forms of tau are toxic in Alzheimer's disease. *Transl. Neurosci.* **2012**, *3*, 223-233.

11. Akoury, E.; Mukrasch, M. D.; Biernat, J.; Tepper, K.; Ozenne, V.; Mandelkow, E.; Blackledge, M.; Zweckstetter, M., Remodeling of the conformational ensemble of the repeat domain of tau by an aggregation enhancer. *Protein Sci.* **2016**, *25*, 1010-1020.

12. Siddiqua, A.; Margittai, M., Three- and four-repeat Tau coassemble into heterogeneous filaments: an implication for Alzheimer disease. *J. Biol. Chem.* **2010**, *285*, 37920-37926.

13. Margittai, M.; Langen, R., Template-assisted filament growth by parallel stacking of tau. *Proc. Natl. Acad. Sci. U. S. A.* **2004**, *101*, 10278-10283.

14. Jeganathan, S.; von Bergen, M.; Brutlach, H.; Steinhoff, H. J.; Mandelkow, E., Global hairpin folding of tau in solution. *Biochemistry* **2006**, *45*, 2283-2293.

15. Elbaum-Garfinkle, S.; Rhoades, E., Identification of an Aggregation-Prone Structure of Tau. *J. Am. Chem. Soc.* **2012**, *134*, 16607-16613.

16. Falcon, B.; Cavallini, A.; Angers, R.; Glover, S.; Murray, T. K.; Barnham, L.; Jackson, S.; O'Neill, M. J.; Isaacs, A. M.; Hutton, M. L., et al., Conformation determines the seeding potencies of native and recombinant Tau aggregates. *J. Biol. Chem.* **2015**, *290*, 1049-1065.

17. Mukrasch, M. D.; Bibow, S.; Korukottu, J.; Jeganathan, S.; Biernat, J.; Griesinger, C.; Mandelkow, E.; Zweckstetter, M., Structural polymorphism of 441-residue tau at single residue resolution. *PLoS Biol.* **2009**, *7*, e34.

18. Friedel, M.; Baumketner, A.; Shea, J. E., Effects of Surface Tethering on Protein Folding Mechanisms. *Proc. Natl. Acad. Sci. U. S. A.* **2006**, *103*, 8396-8401.

19. Talaga, D. S.; Lau, W. L.; Roder, H.; Tang, J.; Jia, Y.; DeGrado, W. F.; Hochstrasser, R. M., Dynamics and Folding of Single Two-Stranded Coiled-Coil Peptides Studied by Fluorescent Energy Transfer Confocal Microscopy. *Proc. Natl. Acad. Sci. U. S. A.* **2000**, *97*, 13021-13026.

20. Wang, Q.; Goldsmith, R. H.; Jiang, Y.; Bockenhauer, S. D.; Moerner, W. E., Probing single biomolecules in solution using the anti-Brownian electrokinetic (ABEL) trap. *Acc. Chem. Res.* **2012**, *45*, 1955-1964.

21. Mao, A. H.; Crick, S. L.; Vitalis, A.; Chicoine, C. L.; Pappu, R. V., Net charge per residue modulates conformational ensembles of intrinsically disordered proteins. *Proc. Natl. Acad. Sci. U. S. A.* **2010**, *107*, 8183-8188.

22. Orte, A.; Birkett, N. R.; Clarke, R. W.; Devlin, G. L.; Dobson, C. M.; Klenerman, D., Direct characterization of amyloidogenic oligomers by single-molecule fluorescence. *Proc. Natl. Acad. Sci. U. S. A.* **2008**, *105*, 14424-14429.

23. Sisamakis, E.; Valeri, A.; Kalinin, S.; Rothwell, P. J.; Seidel, C. A. M., Accurate Single-Molecule FRET Studies Using Multiparameter Fluorescence Detection. *Methods Enzymol.* **2010**, *475*, 455-514.

24. Banerjee, P. R.; Mitrea, D. M.; Kriwacki, R. W.; Deniz, A. A., Asymmetric Modulation of Protein Order-Disorder Transitions by Phosphorylation and Partner Binding. *Angew. Chem., Int. Ed. Engl.* **2016**, *55*, 1675-1679.

25. Aznauryan, M.; Nettels, D.; Holla, A.; Hofmann, H.; Schuler, B., Single-molecule spectroscopy of cold denaturation and the temperature-induced collapse of unfolded proteins. *J. Am. Chem. Soc.* **2013**, *135*, 14040-14043.

26. Chung, H. S.; McHale, K.; Louis, J. M.; Eaton, W. A., Single-molecule fluorescence experiments determine protein folding transition path times. *Science* **2012**, *335*, 981-984.

27. Banerjee, P. R.; Deniz, A. A., Shedding light on protein folding landscapes by single-molecule fluorescence. *Chem. Soc. Rev.* **2014**, *43*, 1172-1188.

28. Cremades, N.; Cohen, S. I.; Deas, E.; Abramov, A. Y.; Chen, A. Y.; Orte, A.; Sandal, M.; Clarke, R. W.; Dunne, P.; Aprile, F. A., et al., Direct observation of the interconversion of normal and toxic forms of alpha-synuclein. *Cell* **2012**, *149*, 1048-1059.

29. Shammas, S. L.; Garcia, G. A.; Kumar, S.; Kjaergaard, M.; Horrocks, M. H.; Shivji, N.; Mandelkow, E.; Knowles, T. P.; Mandelkow, E.; Klenerman, D., A mechanistic model of tau amyloid aggregation based on direct observation of oligomers. *Nat. Commun.* **2015**, *6*, 7025.

30. Kayci, M.; Chang, H.-C.; Radenovic, A., Electron spin resonance of nitrogen-vacancy defects embedded in single nanodiamonds in an ABEL trap. *Nano Lett.* **2014**, *14*, 5335-5341.

31. Fields, A. P.; Cohen, A. E., Electrokinetic trapping at the one nanometer limit. *Proc. Natl. Acad. Sci. U. S. A.* **2011**, *108*, 8937-8942.

32. Gradinaru, C. C.; Marushchak, D. O.; Samim, M.; Krull, U. J., Fluorescence anisotropy: from single molecules to live cells. *Analyst* **2010**, *135*, 452-459.

33. Schweers, O.; Mandelkow, E. M.; Biernat, J.; Mandelkow, E., Oxidation of cysteine-322 in the repeat domain of microtubule-associated protein tau controls the in vitro assembly of paired helical filaments. *Proc. Natl. Acad. Sci. U. S. A.* **1995**, *92*, 8463-8467.

34. Kashiwagi, T.; Yokoyama, K.; Ishikawa, K.; Ono, K.; Ejima, D.; Matsui, H.; Suzuki, E., Crystal structure of microbial transglutaminase from Streptoverticillium mobaraense. *J. Biol. Chem.* **2002**, *277*, 44252-44260.

35. Vogelsang, J.; Kasper, R.; Steinhauer, C.; Person, B.; Heilemann, M.; Sauer, M.; Tinnefeld, P., A Reducing and Oxidizing System Minimizes Photobleaching and Blinking of Fluorescent Dyes. *Angew. Chem., Int. Ed. Engl.* **2008**, *47*, 5465-54659.

36. Kalinin, S.; Sisamakis, E.; Magennis, S. W.; Felekyan, S.; Seidel, C. A. M., On the Origin of Broadening of Single-Molecule FRET Efficiency Distributions beyond Shot Noise Limits. *J. Phys. Chem. B* **2010**, *114*, 6197-6206.

37. Milles, S.; Lemke, E. A., Mapping multivalency and differential affinities within large intrinsically disordered protein complexes with segmental motion analysis. *Angew. Chem., Int. Ed. Engl.* **2014**, *53*, 7364-7367.

38. Ellis, J. P.; Culviner, P. H.; Cavagnero, S., Confined dynamics of a ribosome-bound nascent globin: Cone angle analysis of fluorescence depolarization decays in the presence of two local motions. *Protein Sci.* **2009**, *18*, 2003-2015.

39. Lipari, G.; Szabo, A., Effect of librational motion on fluorescence depolarization and nuclear magnetic resonance relaxation in macromolecules and membranes. *Biophys. J.* **1980**, *30*, 489-506.

40. Schröder, G. F.; Alexiev, U.; Grubmüller, H., Simulation of Fluorescence Anisotropy Experiments: Probing Protein Dynamics. *Biophys. J.* **2005**, *89*, 3757-3770.

41. Hughes, L. D.; Rawle, R. J.; Boxer, S. G., Choose Your Label Wisely: Water-Soluble Fluorophores Often Interact with Lipid Bilayers. *PLoS One* **2014**, *9*, e87649.

42. Wang, Q.; Moerner, W. E., Lifetime and Spectrally Resolved Characterization of the Photodynamics of Single Fluorophores in Solution Using the Anti-Brownian Electrokinetic Trap. *J. Phys. Chem. B* **2013**, *117*, 4641-4648.

43. Soranno, A.; Buchli, B.; Nettels, D.; Cheng, R. R.; Müller-Späth, S.; Pfeil, S. H.; Hoffmann, A.; Lipman, E. A.; Makarov, D. E.; Schuler, B., Quantifying internal friction in unfolded and intrinsically disordered proteins with single-molecule spectroscopy. *Proc. Natl. Acad. Sci. U. S. A.* **2012**, *109*, 17800-17806.

44. Elbaum-Garfinkle, S.; Cobb, G.; Compton, J. T.; Li, X. H.; Rhoades, E., Tau mutants bind tubulin heterodimers with enhanced affinity. *Proc. Natl. Acad. Sci. U. S. A.* **2014**, *111*, 6311-6316.

45. Carmel, G.; Mager, E. M.; Binder, L. I.; Kuret, J., The Structural Basis of Monoclonal Antibody Alz50's Selectivity for Alzheimer's Disease Pathology. *J. Biol. Chem.* **1996**, *271*, 32789-32795.

46. Lakowicz, J. R., *Principles of fluorescence spectroscopy*, 3rd ed.; Springer: New York, 2006.

47. Wang, Q.; Moerner, W. E., Single-molecule motions enable direct visualization of biomolecular interactions in solution. *Nat. Methods* **2014**, *11*, 555-558.

48. Meyer, V.; Holden, M. R.; Weismiller, H. A.; Eaton, G. R.; Eaton, S. S.; Margittai, M., Fracture and Growth Are Competing Forces Determining the Fate of Conformers in Tau Fibril Populations. *J. Biol. Chem.* **2016**, *291*, 12271-12281.

49. Herman, T. K.; Mackowiak, S. A.; Kaufman, L. J., High power light emitting diode based setup for photobleaching fluorescent impurities. *Review of Scientific Instruments* **2009**, *80*, 016107.

50. Rasnik, I.; McKinney, S. A.; Ha, T., Nonblinking and long-lasting single-molecule fluorescence imaging. *Nat. Methods* **2006**, *3*, 891-893.

51. Aitken, C. E.; Marshall, R. A.; Puglisi, J. D., An oxygen scavenging system for improvement of dye stability in single-molecule fluorescence experiments. *Biophys. J.* **2008**, *94*, 1826-1835.

52. Crawford, D. J.; Hoskins, A. A.; Friedman, L. J.; Gelles, J.; Moore, M. J., Visualizing the splicing of single pre-mRNA molecules in whole cell extract. *RNA* **2008**, *14*, 170-179.

53. Cohen, A. E.; Moerner, W. E., Controlling Brownian motion of single protein molecules and single fluorophores in aqueous buffer. *Opt. Express* **2008**, *16*, 6941-6956.

54. Wang, H. Y.; Foote, R. S.; Jacobson, S. C.; Schneibel, J. H.; Ramsey, J. M., Low temperature bonding for microfabrication of chemical analysis devices. *Sens. Actuators, B* **1997**, *45*, 199-207.

55. Goldsmith, R. H.; Tabares, L. C.; Kostrz, D.; Dennison, C.; Aartsma, T. J.; Canters, G. W.; Moerner, W. E., Redox cycling and kinetic analysis of single molecules of solution-phase nitrite reductase. *Proc. Natl. Acad. Sci. U. S. A.* **2011**, *108*, 17269-17274.

56. Kartalov, E. P.; Unger, M. A.; Quake, S. R., Polyelectrolyte surface interface for single-molecule fluorescence studies of DNA polymerase. *BioTechniques* **2003**, *34*, 505-510.

57. Goldsmith, R. H.; Moerner, W. E., Watching conformational- and photodynamics of single fluorescent proteins in solution. *Nat. Chem.* **2010**, *2*, 179-186.

58. Wang, Q.; Moerner, W. E., An Adaptive Anti-Brownian ELectrokinetic trap with real-time information on single-molecule diffusivity and mobility. *ACS Nano* **2011**, *5*, 5792-5799.

59. Wang, Q.; Moerner, W. E., Optimal strategy for trapping single fluorescent molecules in solution using the ABEL trap. *Appl. Phys. B* **2010**, *99*, 23-30.

60. Dutt, G. B.; Doraiswamy, S.; Periasamy, N.; Venkataraman, B., Rotational reorientation dynamics of polar dye molecular probes by picosecond laser spectroscopic technique. *J. Chem. Phys.* **1990**, *93*, 8498-8513.

61. Kapusta, P.; Erdmann, R.; Ortmann, U.; Wahl, M., Time-Resolved Fluorescence Anisotropy Measurements Made Simple. *J. Fluoresc.* **2003**, *13*, 179-183.

62. Koshioka, M.; Sasaki, K.; Masuhara, H., Time-Dependent Fluorescence Depolarization Analysis in Three-Dimensional Microspectroscopy. *Appl. Spectrosc.* **1995**, *49*, 224-228.

63. Watkins, L. P.; Yang, H., Detection of intensity change points in time-resolved single-molecule measurements. *J. Phys. Chem. B* **2005**, *109*, 617-628.

64. Boudjellaba, H.; MacGibbon, B.; Sawyer, P., On Exact Inference for Change in a Poisson Sequence. *Commun. Stat. Theory Methods* **2001**, *30*, 407-434.

65. Ameloot, M.; Hendrickx, H.; Herreman, W.; Pottel, H.; Van Cauwelaert, F.; van der Meer, W., Effect of orientational order on the decay of the fluorescence anisotropy in membrane suspensions. Experimental verification on unilamellar vesicles and lipid/alpha-lactalbumin complexes. *Biophys. J.* **1984**, *46*, 525-539.

66. Kinosita, K., Jr.; Ikegami, A.; Kawato, S., On the wobbling-in-cone analysis of fluorescence anisotropy decay. *Biophys. J.* **1982**, *37*, 461-464.

Chapter 3

3. Aggregation Competency of Labeled Tau Mutants

The material in this chapter is preliminary and unpublished data. This chapter is written to serve as a summary of the work done and provide context and guidance for future work using different labeled mutants of tau protein.

3.1 Abstract

Single-molecule fluorescence studies of proteins require mutation of the protein backbone and/or introduction of a fluorescent label. Introducing such alterations, however, can have unintended consequences and must therefore be chosen carefully. While many methods exist for determining the perturbation of the modifications to the protein, here we describe the use of bulk fluorescence as a proxy for determining the amount of tau protein that has incorporated into an aggregate. By analyzing 13 different mutants of htau40, we can start to understand the effect that label position has on aggregation competency.

3.2 Introduction

There are many ways to determine if a mutation or label affect the protein of interest. For tau protein, mutations and label effects can be tested by studying binding of tau protein to tubulin,[1] electron microscopy of formed fibrils,[2] the effect of spin labels on fibril formation,[3] or circular dichroism of labeled species.[4] Another method is to induce aggregation of labeled tau and measure how much labeled protein is incorporated into the aggregate by measuring the fluorescence of the supernatant.[5]

This final method of assessing the effect of the label at the designated position was chosen with an eye toward future experiments that will use the anti-Brownian electrokinetic (ABEL) trap to observe the formation of aggregates. Therefore, the assessment method was chosen to probe whether the label interferes with the particular property we hope to study in the future. While microtubule polymerization assays might be a better technique for assessing the function of the labeled tau protein, for example, that would not provide an accurate predictor of the aggregation competency. Using this approach, we have tested 13 different ATTO647N-labeled mutants of htau40, spanning from residue 17 to 433.

3.3 Results and Discussion

*3.3.1 **Labeled protein incorporates into fibrils***

Upon incubation with seeds and excess htau40 protein (with both naturally occurring cysteines mutated to serines, C291S and C322S), labeled htau40 monomer was incorporated into fibrils. This incorporation was determined by measuring the fluorescence of the sample before and after sedimenting the fibrils; any labeled monomer that was incorporated into the fibril was absent from the supernatant, and any decrease in fluorescence intensity after centrifugation was assumed to be due to incorporation. All 13 mutants displayed a decrease in fluorescence intensity of the solution (Figure 3-1). The percent change in fluorescence was calculated for each of 13 different htau40 mutants labeled with ATTO647N according to:

$$\%\ change = \frac{I_{before\ sedimentation} - I_{after\ sedimentation}}{I_{before\ sedimentation}} \times 100 \qquad \text{(equation 3-1)}$$

where $I_{before\ sedimentation}$ and $I_{after\ sedimentation}$ are the integrated fluorescence intensity before and after the sample was centrifuged, respectively, integrated over the entire fluorescence spectrum from λ = 600 – 800 nm.

A control sample of htau40-310-ATTO647N that did not contain seeds was also analyzed. The aggregation in a sample without seeds should be much slower and less efficient than those samples that did contain seeds. While the average percent change for the control sample is smaller than for the 310 sample that contained seeds, as expected, the large error bars on both samples make it difficult to be definitive about the difference in efficiency of aggregation.

The results show that for some mutants — specifically htau40-103, htau40-322, htau40-323, and htau40-324 — there is a large change in the fluorescence intensity, indicating that a greater percentage of labeled protein was incorporated into the formed fibril and absent from the supernatant after sedimentation. Many of these results come with quite a large error, but htau40-103, htau40-331, and htau40-376 show the most reproducible results.

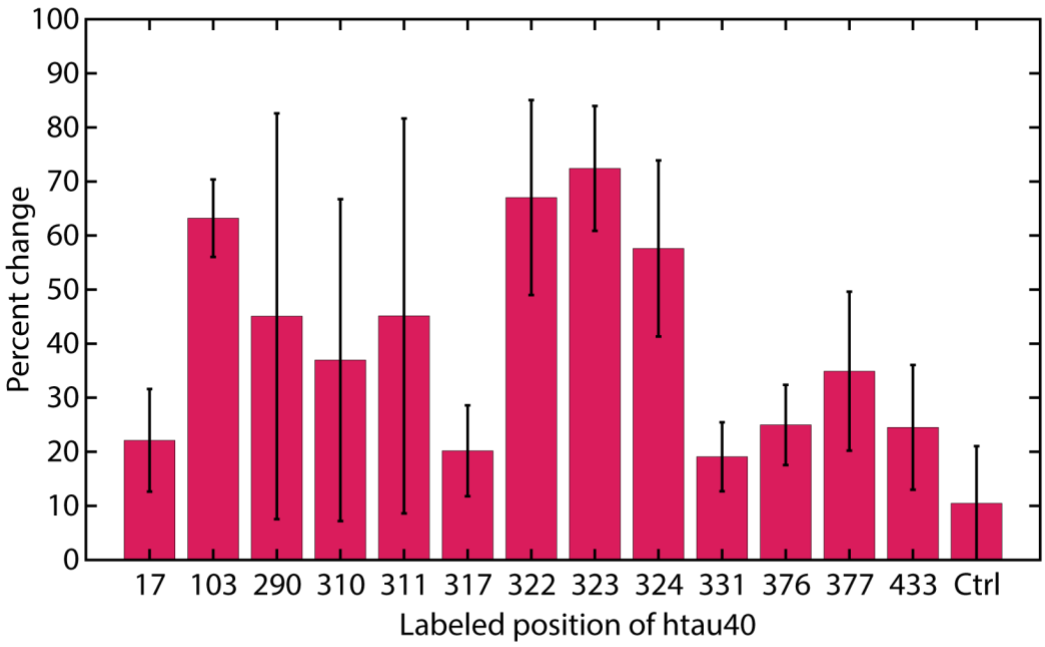

Figure 3-1. Percent change of fluorescence intensity in bulk solutions of aggregated tau protein. Total error bar height represents 2x the standard deviation. 'Ctrl' represents a control sample that contained labeled htau40-310-ATTO647N, heparin, htau40 (no cysteines) and no seeds. Each bar represents the average of three trials.

3.3.1.1 *Future directions to improve reproducibility*

Through discussions with Professor Martin Margittai, some potential avenues have been identified for improving reproducibility of these experiments. The small volume of added seeds to each reaction (10 µL) may result in inconsistent addition of seeds to each reaction. This would cause inconsistent rates of aggregation across multiple samples. The reproducibility of some samples (htau40-103, htau40-331, and htau40-376), therefore, may be due to inconsistent addition of seeds to the samples for all three trials.

Another possible method for improving aggregation is providing agitation during the incubation at 37 °C, which was not performed here. This agitation would speed the aggregation process and correspondence with Martin indicates that without this agitation aggregation may be much slower than originally anticipated (>10 days rather than the 48 hours allotted here).

In the future, it is possible to quantify the amount of labeled monomer incorporated into the sedimented fibrils by dissolving the pellets in SDS and measuring the fluorescence.

3.3.2 Choice of mutant locations

The mutations that were chosen span almost the entire length of the protein, from residue 17 to 433. These residues were mutated to cysteines (except in the case of residue 322 which is a naturally occurring cysteine) for labeling with ATTO647N-maleimide, and natural cysteines were mutated to serines. I will now give a brief overview of literature precedent and current understanding of these residues to serve as a guide for future decisions.

3.3.2.1 *htau40-17*

Residue 17 is a hydrophilic threonine in the native sequence of htau40.[6] NMR analysis of full-length tau protein has shown that while the N-terminal projection domain as a whole has a high degree of flexibility and rapidly interconverts between conformations, residues 1 – 20 favor a compact conformation,

with strong contacts to residues 30 – 50.[6] This compact conformation aligns with the negative H-N residual dipole coupling (RDC) measurements, which suggest a high propensity for turn formation in IDPs.[6] These same NMR studies show contacts between residues 1 – 20 and the C-terminal,[6] a finding that reinforced the prior FRET study that found residues 17 and 432 in close proximity.[4] Electron paramagnetic resonance (EPR) measurements confirm that a full length tau labeled with an iodoacetamide spin-label (JAA6) at position 17 (htau40-17_{JAA6}) is highly flexible, indicating that any interactions with other segments of the protein are transient.[4]

3.3.2.2 *htau40-103*

Residue 103 is a hydrophobic alanine in the natural htau40 sequence.[6] This residue also resides in the N-terminal projection domain, which is characterized by a high rate of interconversion of conformations via NMR relaxation studies.[6]

3.3.2.3 *htau40-290*

Residue 290 is a lysine amino acid with basic characteristic (positively charged) in htau40, located in the 2nd repeat of the microtubule-binding region (MTBR).[6] While I have not found literature focused specifically on residue 290, EPR studies confirm that residue 291 has a high degree of flexibility when mutated to a cysteine and labeled with a spin label.[4] NMR studies suggest that regions on either side of position 290 (^{274}Lys – Leu^{284} and ^{305}Ser – Asp^{315}) have high β-sheet propensity and are essential in paired helical filament formation.[6]

3.3.2.4 *htau40-310*

Residue 310 is a hydrophilic tyrosine amino acid in the htau40 sequence in the 3rd repeat of the MTBR.[6-7] When mutated to a tryptophan residue, it is almost completely solvent exposed.[4, 8] FRET

measurements of htau40-310_W-17_{DANS} show low FRET, indicating that the N-terminus (position 17) is not close to this part of the repeat region (position 310).[4]

While solvent exposed in solution, position 310 also resides in a β-sheet prone region between ^{305}Ser and Asp^{315}.[6, 9] It is also part of the hexapeptide ^{306}Val – Lys^{311} that is necessary for aggregation initiation.[10] Cryo-EM experiments elucidating the protofilament core show that this position is in the first β-strand and is in close proximity to the leucine at position 376 in the eighth β-strand, and residues 306 to 311 form a complementary packing with residues 373 – 378.[11]

3.3.2.5 *htau40-311*

Residue 311 is a lysine amino acid with basic character in the htau40 sequence.[6] It is positioned in the 3rd repeat of the MTBR[7] and is the final residue of a β-sheet prone hexapeptide motif required for initiating aggregation.[10] Cryo-EM structures of the protofilament core of aggregates position this residue as terminating the first of the β-strands.[11]

3.3.2.6 *htau40-317*

Residue 317 is a lysine amino acid with basic character in the 3rd repeat of the MTBR.[6-7] When a peptide only comprising the repeat domain was analyzed via NMR and molecular dynamics simulations, the stretch from ^{314}Asp – Lys^{317} was found to have a propensity for forming turns.[12] This is believed to hold true for htau40.[6] Cryo-EM studies of the protofilament core show it positioned in the second β-strand.[11] Between residues 313 and 317, this protofilament comes closest to residues 321 – 324 of the second protofilament.[11]

3.3.2.7 *htau40-322*

Residue 322 is one of two naturally occurring cysteines in htau40, and it is hydrophilic in nature (the other naturally occurring cysteine is at position 291).[6, 13] EPR studies of htau40-322$_{JAA6}$ (spin labeled cysteine at 322) indicate a high degree of flexibility.[4] This residue is located in the 3rd repeat of the MTBR[7] and at the end of the second β-strand of the protofilament core.[11]

This position has also been used extensively for FRET studies, leading to the proposed "paperclip" model.[4] In this model, the FRET distance between residue 322 and 432 is 25.6 Å (E_{FRET} = 0.29), and the distance between 18 and 322 is 30.1 Å (E_{FRET} = 0.14).[4] Upon denaturation, however, the distance between 18 and 322 expands slightly to 32.3 Å.[4] Single-molecule FRET studies have shown a slightly larger E_{FRET} between positions 322 and *433* of E_{FRET} = 0.51 (Note: not directly comparable to the distance between 322 and 432 above).[5]

3.3.2.8 *htau40-323*

Residue 323 is a hydrophilic glycine residue in htau40.[6] It also resides in the 3rd repeat of the MTBR,[7] but just beyond the third β-strand of the protofilament core.[11] This glycine acts as a β-turn to introduce a right turn into the protofilament core.[11]

3.3.2.9 *htau40-324*

Residue 324 is a hydrophilic serine in htau40,[6] located in the 3rd repeat of the MTBR.[7] This residue is one of the major phosphorylation sites that is more commonly phosphorylated in Alzheimer's disease and causes detachment of tau from microtubules.[6] NMR studies, however, show this is not a strong contact point between tau and microtubules, indicating that the disruption of microtubule binding is likely a long-range electrostatic interaction.[6]

3.3.2.10 *htau40-331*

Residue 331 is a positively charged basic lysine in the native htau40 sequence.[6] This is part of the structured core of the protofilament from ^{281}Lys – Arg^{406}, as detailed by cryo-EM.[11]

3.3.2.11 *htau40-376*

Residue 376 is a hydrophobic leucine in the native htau40 sequence.[6] It is located in the weakly homologous R' repeat region shown in Figure 1-2. NMR relaxation rate measurements show this residue to be in a region (^{370}Lys – Lys^{395}) with transient β-sheet structure.[6] It was also shown that the stretch from 360 – 441 transiently contacts the repeat region and residues 1 – 40.[6]

Cryo-EM measurements show that this residue is part of the protofilament core for both straight and paired helical filaments.[11]

3.3.2.12 *htau40-377*

Residue 377 is a hydrophilic threonine in htau40.[6] It has similar properties to position 376, above.

3.3.2.13 *htau40-433*

Residue 433 is a hydrophilic serine in htau40.[6] It is located in a region with high α-helical propensity.[6]

FRET efficiency has been shown to drop when moving an IAEDANS label from position 435 to 433, indicating that the label may disrupt some secondary structure at the C-terminal end when attached to position 433.[4] Single-molecule FRET used position 433 as a common mutation on the C-terminal tail.

3.4 Conclusion and Future Directions

Thinking forward, we would like to complete a similar study as that in chapter 2, using the anti-Brownian electrokinetic trap to prolong observation time of individual protein molecules in order to measure their anisotropy. With a robust set of labeled positions, we hope to expand our understanding of the conformational heterogeneity of tau protein by learning about the local environment of the fluorophore in different regions of the protein, perhaps identifying more long-lived conformations. Further, aggregates can be studied in order to detail the conformational changes that occur during the aggregation process, likely resulting in an increase in anisotropy as the label experiences a more restricted environment.

3.5 Experimental Section

Samples were prepared with 1 μM labeled tau protein and 9 μM unlabeled htau40-wt (1:9 ratio labeled monomer: unlabeled monomer, 10 μM total concentration).[1] Formed fibrils of tau protein contained 24.99 μM htau40-wt and 10 nM htau40-310-atto633 (25 μM total concentration)[2] and were sonicated for 60 sec in a bath sonicator to break them into smaller seeds. 10 % seeds (molar monomer equivalent)[3] were added to the reaction, along with 20 μM heparin,[4] and the reaction was left for ~48 hours

[1] 'Wild-type' tau protein from the Margittai lab was a construct in which the natural cysteines have been mutated to serines (htau40-C291S-C322S).

[2] We used these fibrils because it is what Michael Holden originally sent us for another separate purpose. The integration of hT40-310-atto633 is not necessary for this experiment. Michael checked that the labeled protein was incorporated into the fibril by sedimenting the protein and running the sediment and supernatant on a gel. He was unable to see a band in the supernatant lane, so assumes it incorporated but cannot be sure or exact about percent incorporation.

[3] 'Molar monomer equivalent' is a term used by the Margittai lab. If a reaction, such as this one, is run with 10 μM total monomer concentration, then 10 % of that concentration is 1 μM of seeds.

[4] The Margittai lab has had variable success with different heparin suppliers in the past. While they always see aggregation, they do not always see the characteristic single line spectrum in their EPR experiment. They test their heparin before use by inducing aggregation and verifying that a single line spectrum results. The heparin used in these studies came from a verified stock from the Margittai lab.

at 37 °C. The monomer, heparin and seeds were added to a buffer containing 10 mM phosphate buffer, 100 mM NaCl and 25 % glycerol for 250 µL final volume.

After the tau protein was allowed to aggregate for 48 hours, 200 µL of each sample was removed and centrifuged at 130,000 x g for 30 min in a Beckman Coulter ultracentrifuge at 4 °C (rotor 120.2 TLA, 60 000 rpm).[5] After centrifugation, the supernatant was removed and the fluorescence emission spectrum of the supernatant and the remaining sample from before centrifugation was measured on a Fluoromax-4 fluorimeter in the Chanda lab. For ATTO647N dye, samples were excited at 570 nm, with emission recorded from 600 – 800 nm, with increments of 2 nm and slit widths of 5 nm. The fluorescence signal was integrated and the percent change in fluorescence was determined.

[5] Samples should be within 1 mg of one another to properly balance the centrifuge. This can be achieved by removing sample to achieve the proper weight. Removing sample (rather than adding buffer) will keep concentrations the same.

3.6 References

1. Elbaum-Garfinkle, S.; Cobb, G.; Compton, J. T.; Li, X. H.; Rhoades, E., Tau mutants bind tubulin heterodimers with enhanced affinity. *Proc. Natl. Acad. Sci. U. S. A.* **2014**, *111*, 6311-6316.

2. Elbaum-Garfinkle, S.; Ramlall, T.; Rhoades, E., The role of the lipid bilayer in tau aggregation. *Biophys. J.* **2010**, *98*, 2722-2730.

3. Margittai, M.; Langen, R., Template-assisted filament growth by parallel stacking of tau. *Proc. Natl. Acad. Sci. U. S. A.* **2004**, *101*, 10278-10283.

4. Jeganathan, S.; von Bergen, M.; Brutlach, H.; Steinhoff, H. J.; Mandelkow, E., Global hairpin folding of tau in solution. *Biochemistry* **2006**, *45*, 2283-2293.

5. Elbaum-Garfinkle, S.; Rhoades, E., Identification of an Aggregation-Prone Structure of Tau. *J. Am. Chem. Soc.* **2012**, *134*, 16607-16613.

6. Mukrasch, M. D.; Bibow, S.; Korukottu, J.; Jeganathan, S.; Biernat, J.; Griesinger, C.; Mandelkow, E.; Zweckstetter, M., Structural polymorphism of 441-residue tau at single residue resolution. *PLoS Biol.* **2009**, *7*, e34.

7. Gustke, N.; Trinczek, B.; Biernat, J.; Mandelkow, E. M.; Mandelkow, E., Domains of tau protein and interactions with microtubules. *Biochemistry* **1994**, *33*, 9511-9522.

8. Jeganathan, S.; Hascher, A.; Chinnathambi, S.; Biernat, J.; Mandelkow, E. M.; Mandelkow, E., Proline-directed pseudo-phosphorylation at AT8 and PHF1 epitopes induces a compaction of the paperclip folding of Tau and generates a pathological (MC-1) conformation. *J. Biol. Chem.* **2008**, *283*, 32066-32076.

9. Eliezer, D.; Barré, P.; Kobaslija, M.; Chan, D.; Li, X.; Heend, L., Residual Structure in the Repeat Domain of Tau: Echoes of Microtubule Binding and Paired Helical Filament Formation. *Biochemistry* **2005**, *44*, 1026-1036.

10. von Bergen, M.; Friedhoff, P.; Biernat, J.; Heberle, J.; Mandelkow, E. M.; Mandelkow, E., Assembly of tau protein into Alzheimer paired helical filaments depends on a local sequence motif ((306)VQIVYK(311)) forming beta structure. *Proc. Natl. Acad. Sci. U. S. A.* **2000**, *97*, 5129-5134.

11. Fitzpatrick, A. W. P.; Falcon, B.; He, S.; Murzin, A. G.; Murshudov, G.; Garringer, H. J.; Crowther, R. A.; Ghetti, B.; Goedert, M.; Scheres, S. H. W., Cryo-EM structures of tau filaments from Alzheimer's disease. *Nature* **2017**, *547*, 185-190.

12. Mukrasch, M. D.; Markwick, P.; Biernat, J.; Bergen, M.; Bernado, P.; Griesinger, C.; Mandelkow, E.; Zweckstetter, M.; Blackledge, M., Highly populated turn conformations in natively unfolded tau protein identified from residual dipolar couplings and molecular simulation. *J. Am. Chem. Soc.* **2007**, *129*, 5235-5243.

13. Lee, G.; Cowan, N.; Kirschner, M., The primary structure and heterogeneity of tau protein from mouse brain. *Science* **1988**, *239*, 285-288.

Chapter 4

4. Global Analysis of Perovskite Photophysics Reveals Importance of Geminate Pathways

The material in this chapter was originally published as Manger, L. H.*; Rowley, M. B.*; Fu, Y.; Foote, A. K.; Rea, M. T.; Wood, S. L.; Jin, S.; Wright, J. C.; Goldsmith, R. H., Global Analysis of Perovskite Photophysics Reveals Importance of Geminate Pathways. *J. Phys. Chem. C* 2017, *121*, 1062-1071. *These authors contributed equally to this work.

Lydia Manger performed time-resolved photoluminescence measurements on $MAPbI_3$ perovskites and initial data processing. Matthew Rowley developed a simulation to describe the recombination kinetics of the material.

4.1 Abstract

Hybrid organic-inorganic perovskites demonstrate desirable photophysical behaviors and promising applications from efficient photovoltaics to lasing, but the fundamental nature of excited state species is still under debate. We collected time-resolved photoluminescence of single-crystal nanoplates of methylammonium lead iodide perovskite ($MAPbI_3$), with excitation over a range of fluences and repetition rates, to provide a more complete photophysical picture. A fundamentally different way of simulating the photophysics is developed that relies on unnormalized decays, global analysis over a large array of conditions, and inclusion of steady-state behavior; these details are critical to capturing observed behaviors. These additional constraints require inclusion of spatially-correlated pairs, along with free carriers and traps, demonstrating the importance of our comprehensive analysis. Modeling geminate and non-geminate pathways shows geminate processes are dominant at high carrier densities and early times.

Our combination of data and simulation provides a detailed picture of perovskite photophysics across multiple excitation regimes that was not previously available.

4.2 Introduction

Lead halide perovskites, such as methylammonium lead iodide perovskite ($MAPbI_3$), have garnered attention as highly efficient photovoltaic materials with confirmed power conversion efficiencies reaching 20.5%.[1] $MAPbI_3$ absorbs strongly across the solar spectrum,[2] has a favorable band gap of 1.57 eV,[3-4] offers the low-cost solution processability[5-8] characteristic of organic semiconductors, and displays the long carrier lifetime and diffusion lengths characteristic of inorganic semiconductors.[9-10] In fact, carrier diffusion lengths greater than 175 μm have been reported for single-crystal perovskites with long carrier lifetimes (82 μs) and high carrier mobilities (24.0 $cm^2 V^{-1} s^{-1}$).[7] Despite being solution-processed, these materials have low trap density — estimated as low as ~10^{10} cm^{-3} in single crystals[7] or mid-10^{16} to high-10^{17} cm^{-3} in films[11-14] — compared to typical organic thin films[15] with trap densities ~10^{19} cm^{-3}. Furthermore, the band gap energy of the perovskites can be readily tuned between 1.48 and 3.2 eV by halide and cation substitution.[3, 11, 16-17] When the tunability of emission wavelength is considered in conjunction with their high photoluminescence quantum efficiency, these materials and their nanostructures become ideal active materials for low-threshold lasers.[11, 17-19]

Despite the impressive and rapid improvements of various optoelectronic applications of perovskites, there remain essential and fundamental questions regarding the identities and nature of the elementary photoexcitations. For example, there has been debate regarding whether the photoexcitations exist as bound excitons or free electrons and holes.[9-10, 20-21] Polaronic character of free carriers has been suggested as a means of protection.[22] Understanding the underlying photophysics is critical for designing efficient photovoltaic and other optoelectronic devices, and understanding how loss mechanisms may be controlled.[8, 23-26] Equally important is the understanding of the species contributing to the low-density lasing

threshold — an electron-hole plasma[27-28] is believed to be responsible. The low exciton binding energy for $MAPbI_3$ (2 – 50 meV)[29-35] suggests that excitons quickly dissociate, but there is some question about how long the charge carriers remain spatially correlated. Transient absorption (TA) and time-resolved photoluminescence (TRPL) measurements have indicated a bimolecular recombination rate and a quadratic dependence of rate on pump fluence.[13, 27, 36-38] Others have indicated a monomolecular decay rate at low excitation fluences and bimolecular[29, 39] or stretched exponential recombination rate[14] at high fluences. These TA and TRPL traces have been analyzed in varying ways, with studies focusing on fitting either only early[27] or only late[40] decay dynamics. Often only normalized photoluminescence (PL) decays are analyzed, as opposed to accounting for the absolute signal levels across different excitation regimes. In addition, many of these studies have focused on a small range of pump fluences (1 – 2 orders of magnitude) and one repetition rate of the excitation laser, providing characterization over a limited experimental domain. Consequently, even though perovskite materials exhibit highly desirable properties over a range of excitation conditions spanning their use as photovoltaics (low excitation intensity, low repetition rate) and as media for lasers (high excitation intensity, high repetition rate), most experimental investigations have focused on extremely narrow windows and most analyses have been applied to only subsets of the available transient data, leading to incongruence between photophysical models.

In this work, we provide a global perspective on the photophysics of single-crystal $MAPbI_3$ nanostructures by examining TRPL decays over five orders of magnitude of pump fluence (10^{-4} J/cm^2/pulse to 10^{-9} J/cm^2/pulse) and at two extremes of repetition rate (250 kHz and 20 MHz). Critically, the entire TRPL decays are examined without normalization. They are also analyzed under both non-equilibrium conditions, where kinetic factors dominate, and equilibrium conditions where kinetics are unimportant. This data set that spans multiple regimes of perovskite photophysical behaviors is then used to develop and constrain rate equations for all excited state species — free carriers, filled and free traps, and previously largely unconsidered spatially-correlated geminate and non-geminate pairs that are central to our analysis. The

term “geminate pair” has traditionally been used in reference to disordered semiconductors and implies a correlation in lattice position;[41] herein we use it to highlight this correlation for electron-hole pairs originating from the same exciton. Carriers which recombine with a random partner are referred to as “non-geminate”. These rate equations are evaluated over time in a numerical simulation, allowing us to illustrate the evolving populations of the various photoexcited species throughout the decay, and show which radiative pathways contribute to the observed photoluminescence signal. This approach allows us to identify the need for an exciton-like excited state species, observe the changing branching ratio between geminate and non-geminate recombination pathways, resolve how different species contribute to PL under high excitation power (lasing) and low excitation power (solar cell) regimes, and understand how different existing photophysical models can be incorporated into a single global model.

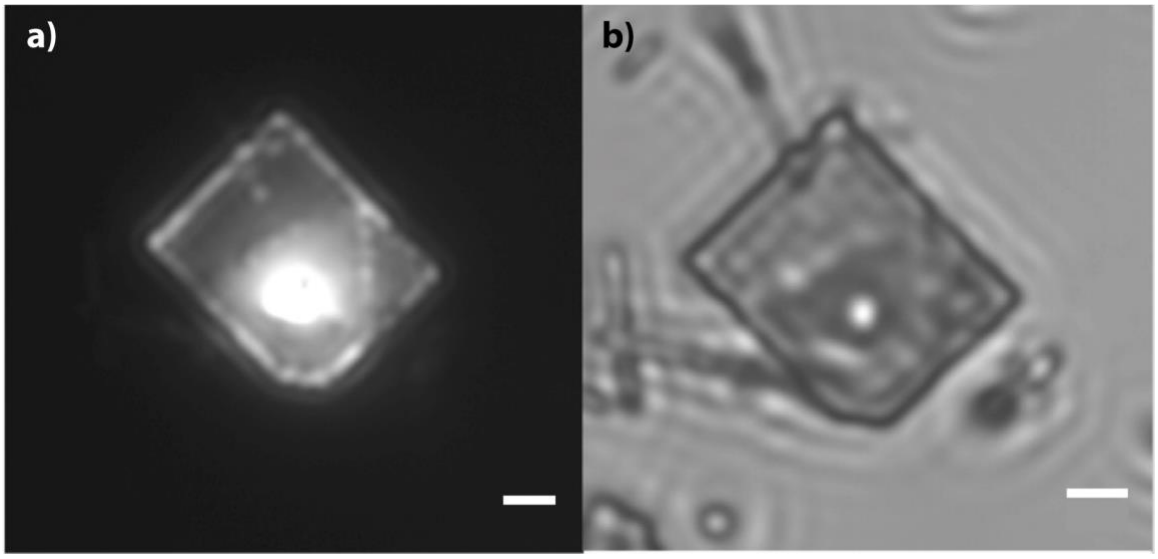

Figure 4-1. $MAPbI_3$ crystal imaged under (a) pulsed excitation and (b) white light. Scale bar is 2 μm.

4.3 Results and Discussion

4.3.1 Development of a model to capture photophysical processes

TRPL traces of individual solution grown single-crystal nanoplates of $MAPbI_3$ (Figure 4-1)[17] were collected at 20 MHz and 250 kHz repetition rates over excitation fluences from 10^{-4} J/cm^2/pulse to 10^{-9} J/cm^2/pulse (Figure 4-2a, b, gray). Previous reports have mainly focused on narrow ranges of excitation

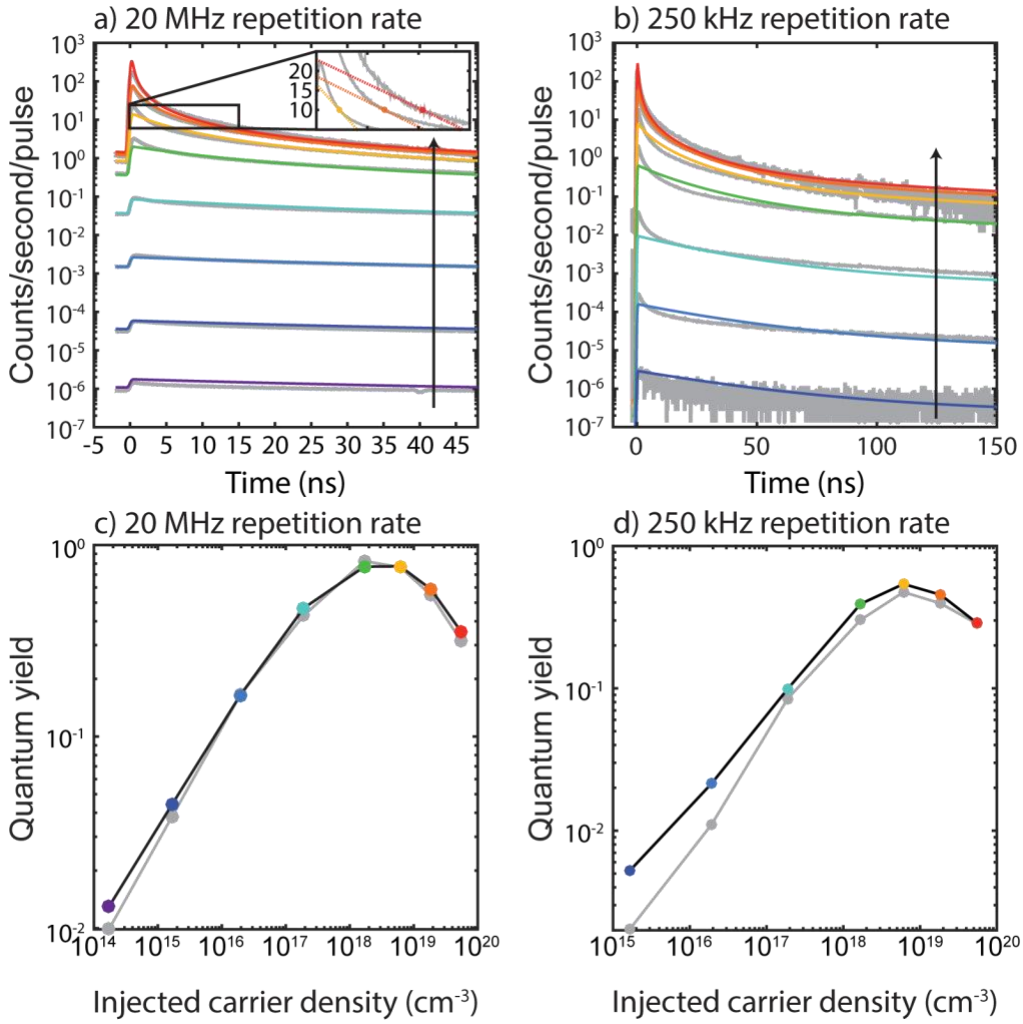

Figure 4-2. TRPL data and simulation for a single nanoplate of $MAPbI_3$ perovskite. TRPL data (gray) and simulation (multiple colors) at (a) 20 MHz and (b) 250 kHz repetition rate. The black arrow denotes increasing excitation intensity. The inset in (a) highlights the different slopes at equal fluorescence intensity for the three highest power curves and is displayed on a linear axis. (c) Quantum yield from measured samples (gray) and simulation (multiple colors) at 20 MHz and (d) at 250 kHz repetition rate. Excitation fluences from high to low: (—) 3.97×10^{-4}, (—) 1.33×10^{-4}, (—) 4.39×10^{-5}, (—) 1.21×10^{-5}, (—) 1.36×10^{-6}, (—) 1.38×10^{-7}, (—) 1.19×10^{-8}, (—) 1.23×10^{-9} J/cm^2/pulse.

fluences and/or a single repetition rate.[27, 29, 37, 40] The TRPL traces show both excitation fluence and repetition rate impact the recombination kinetics of the single-crystal nanoplate. At high excitation fluence, a non-monoexponential decay behavior is observed, with fast early-time dynamics and slow late-time dynamics. The relative importance of these different kinetic regimes varies with excitation power and repetition rate, indicating that the relative contributions of different relaxation pathways change. In particular, the decay transients at 20 MHz and 250 kHz repetition rates for the same injected carrier density have different decay dynamics, indicating that the steady-state built up over many repeated pulses is important to the decay dynamics. Note especially that the slope of the early-time kinetics for the three highest fluences (red, orange and yellow in Figure 4-2a, inset) at 20 MHz have different slopes at the same fluorescence count rate (i.e. 10 counts/second/pulse). The difference reflects changes in the nature of the charge carriers between early times where kinetic factors control the transient behavior, and late times where a quasi-steady-state controls the transient behavior, as will be shown below.

We then developed a numerical simulation to model the decay behaviors (Figure 4-2a, b, multiple colors). This comprehensive simulation evaluates rate equations that include all major radiative and non-radiative decay pathways, as illustrated in Figure 4-3. Critical to the success of this model is the inclusion of a contributing species (illustrated in the left side box in Figure 4-3) beyond the free charge carriers and traps. Kinetic evidence for such a species is conspicuously observed in the Figure 4-2a, inset. At three different excitation intensities, the same PL rate is observed at different times. If a single dominant contributing carrier exists, then the rate of PL decay should be uniquely determined by that species' population, which is proportional to the absolute PL level; this simple scheme predicts that the slopes should be the same for the three curves at equivalent PL values. The observation of different slopes, however, demands that multiple species are contributing to the PL signal. Indeed, the complexity of our early-time PL decay curves at high excitation power defies explanation with only bimolecular recombination of free carriers. Comparing decay rates with absolute intensities reveals this constraint and would have

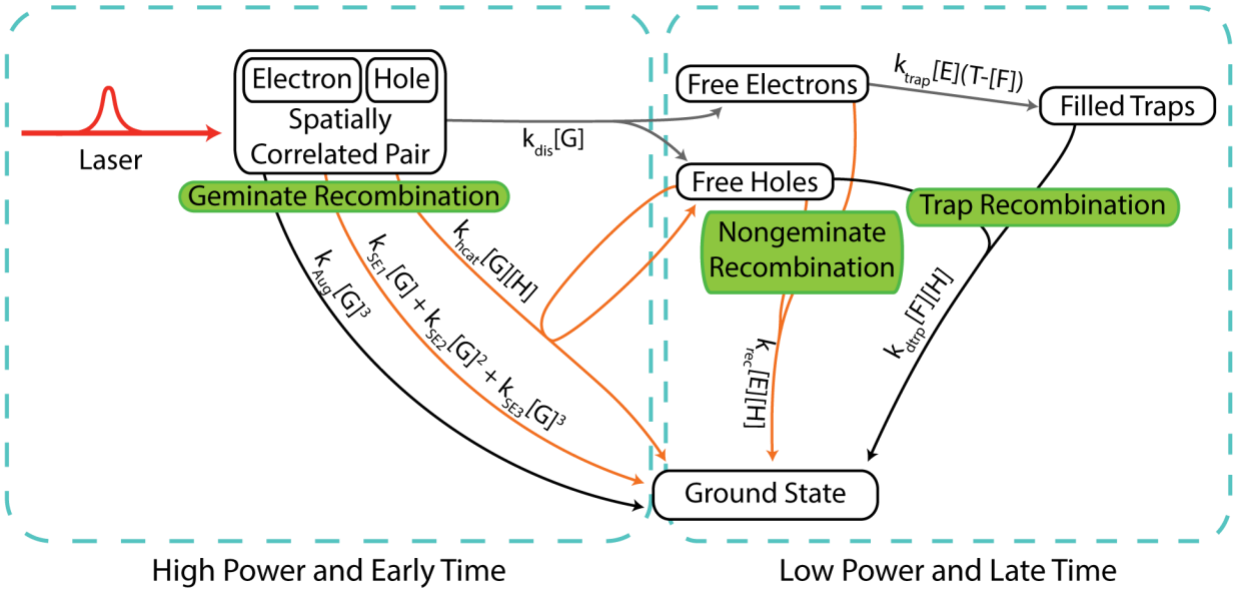

Figure 4-3. Radiative and non-radiative decay pathways in perovskites. Radiative decay processes are indicated by orange arrows, non-radiative transitions between excited states by gray arrows, and non-radiative transitions to ground state by black arrows. Geminate recombination of spatially-correlated pairs dictates kinetics at high power and early time, while traps and non-geminate recombination of free electrons and holes are responsible for decays at low excitation power and late times.

been obscured had the data been normalized, as will be discussed later. These arguments apply similarly to the lowest powers, which exhibit strikingly similar decay curves despite being offset several orders of magnitude in PL intensity. These key comparisons would be impossible to make with normalized data.

The exciton binding energy of $MAPbI_3$ has been reported to be between 2 – 50 meV,[29-35] and therefore the excitons dissociate quickly, suggesting they cannot account for this alternate excited state species. In fact, the generation of free charge carriers occurs in ~2 ps, as measured with time-resolved terahertz spectroscopy.[42-43] Dissociation of excitons and accumulation of free carriers has also been observed as a dynamic Burstein-Moss blue-shift in TA spectra.[13, 33] The alternate species required by the above analysis must retain some characteristics of free carriers — such as the ability to contribute to the dynamic Burstein-Moss effect — and some of the characteristics of an exciton — such as the ability to behave kinetically as a single quasi-particle. Additionally, the species must be kinetically connected to both free carriers and excitons. One species that can satisfy these conditions is a spatially-correlated electron-

hole pair consisting of an electron and hole occupying proximal lattice positions[41] but no longer Coulombically bound as an exciton. It takes some time for the charge carriers to diffuse apart, and for that time they are much closer than expected for a random spatial distribution. This type of species has previously been reported in polymer/fullerene bulk heterojunction materials[44] and implicated in perovskite recombination kinetics as an "electron-hole encounter complex".[45] Our kinetic modeling shows that the inclusion of spatially-correlated pairs enables the faithful reproduction of the observed photophysics over a large range of excitation conditions. This species is distinct from the "correlated-electron hole plasma" described by Saba *et al*.[27] which is mediated by the exciton binding energy and can enhance optical absorption but does not imply long-term spatial correlation.

Table 4-1. Rate equations used in the numerical simulation.

$$\frac{dG}{dt} = pulse(t) - k_{SE1}G - k_{SE2}G^2 - k_{SE3}G^3 - k_{dis}G - k_{hcat}GH - k_{Aug}G^3$$

$$\frac{dE}{dt} = k_{dis}G - k_{rec}EH - k_{trap}E(T - F)$$

$$\frac{dH}{dt} = k_{dis}G - k_{rec}EH - k_{hcat}GH - k_{dtrp}FH$$

$$\frac{dF}{dt} = k_{trap}E(T - F) - k_{dtrp}FH$$

As described in Figure 4-3 and Table 4-1, these spatially-correlated pairs (G)[41, 45] participate in multiple previously described relaxation pathways: 3rd order non-radiative Auger losses (k_{Aug});[11, 13, 46] amplified spontaneous emission[11, 17-18] approximated as a Taylor Series expansion to third order (k_{SE});[47] recombination of the electron in a spatially-correlated pair with a free hole that catalyzes decay to the ground state (k_{hcat});[48] or dissociation (k_{dis})[29, 45] into free electrons and holes. The free electrons (E) and free holes (H) radiatively recombine (k_{rec})[13, 18, 46] to the ground state. Free electrons can also be trapped (k_{trap})[11] at trap sites (T) to create filled traps (F). The electron from a filled trap can then recombine non-radiatively with a free hole (k_{dtrp})[13, 46] via Shockley-Read-Hall recombination. Each of these species and pathways is

necessary to obtain the global fit shown in Figure 4-2. Simpler models are able to fit a few of the curves, but at the expense of other curves (Figure 4-7). For example, the absolute PL signal intensity is affected strongly by k_{Aug} for high powers, by k_{hcat} for middle powers, and by all parameters related to traps for low powers. Inclusion of non-trivial steady-states is particularly important for high repetition rate data since the system cannot decay to the ground state before the next excitation pulse. Normalizing the PL curves or fitting a single repetition rate, as is commonly practiced in the community, would make fitting substantially easier, but would destroy the sensitivity of these parameters. On the other hand, higher order correlations between parameters could be captured, resulting in even better fits, by allowing individual rate constants to vary as a function of carrier densities, as opposed to relying on a single set of constants as used in Figure 4-2.

The simulation was optimized using genetic and simplex algorithms to minimize the least squares error. In contrast to earlier studies, fitting algorithms considered a complete, unnormalized data set over a large range of conditions, rather than fit each normalized condition separately. The simulation provided a single global set of parameters (Table 4-2) that capture the behaviors across all excitation fluences and repetition rates. Importantly, our simulation was able to capture the absolute intensities of the transients without normalization, making it sensitive to the steady-state carrier concentrations created by successive pulsed excitations. This sensitivity provides information about the steady-state populations that would be lost if the decays were normalized to their maximum intensity. The simulation was also able to capture the shifting PL quantum yield of these samples at 20 MHz and 250 kHz (Figure 4-2c, d). A maximum quantum yield was reached around 10^{19} injected carriers/cm^3. As will be shown below, the quantum yield then decreases due to the increased importance of Auger losses that occurs at a high density of spatially-correlated pairs (Figure 4-4a, b). These results are consistent with previous quantum yield studies on $MAPbI_3$ perovskite thin films.[11, 27] Figure 4-3 emphasizes the shifting importance of both radiative and non-

radiative pathways. Namely, that spatially-correlated pairs are important for high powers and early times, whereas free carriers and traps control the dynamics at lower powers and later (>5 ns) times.

Table 4-2. Simulation parameters used in the global fitting with estimated error values. *The parameters with large error values indicate parameters to which the simulation is insensitive.

Parameter Name	Parameter Value	Estimated Error
Trap Density (T)	2.52×10^{18} cm^{-3}	6×10^{16} (2%)
E-H Recombination Rate Constant (k_{rec})	5.9×10^{-13} cm^3s^{-1}	2×10^{-14} (3%)
Trapping Rate Constant (k_{trap})	9.1×10^{-13} cm^3s^{-1}	2×10^{-14} (2%)
Trap Decay Rate Constant (k_{dtrp})	3.42×10^{-12} cm^3s^{-1}	9×10^{-14} (3%)
ASE 1st Order Rate Constant (k_{SE1})	200 s^{-1}	*4×10^{4} (>100%)**
ASE 2nd Order Rate Constant (k_{SE2})	7.4×10^{-12} cm^3s^{-1}	9×10^{-13} (12%)
ASE 3rd Order Rate Constant (k_{SE3})	1.4×10^{-35} cm^6s^{-1}	*4×10^{-31} (>100%)**
Hole-Catalyzed Spatially-Correlated Pair Decay Rate Constant (k_{hcat})	4.4×10^{-12} cm^3s^{-1}	3×10^{-13} (6%)
Spatially-Correlated Pair Dissociation Rate Constant (k_{dis})	2.44×10^{7} s^{-1}	8×10^{5} (3%)
Auger Recombination Rate (k_{Aug})	1.08×10^{-30} cm^6s^{-1}	6×10^{-32} (6%)

Since the model faithfully reproduces the experimental data over a wide range of conditions, we can more closely inspect the time-varying populations of photoexcited species (Figure 4-4) and examine the internal excited state dynamics of hybrid perovskite materials in unprecedented detail. Furthermore, the range of excitation intensity and repetition rate that this model spans allows us to describe the excited state kinetics more comprehensively than would be possible if only a subset of the data were used.

While we do not observe lasing here, the highest excitation powers are above the previously reported lasing threshold (600 nJ/cm^2) for rods prepared under the same conditions.[17] Plots of the populations of excited state species show that at high powers, as would be typically employed in the $MAPbI_3$ perovskite lasing regime,[11, 17] spatially-correlated pairs dominate in the first 5 ns of the decay, while free electrons and holes dominate at times >5 ns (Figure 4-4a). Under low excitation power conditions, such as would be found in the operation of a solar cell, these $MAPbI_3$ perovskite crystals have a steady-state

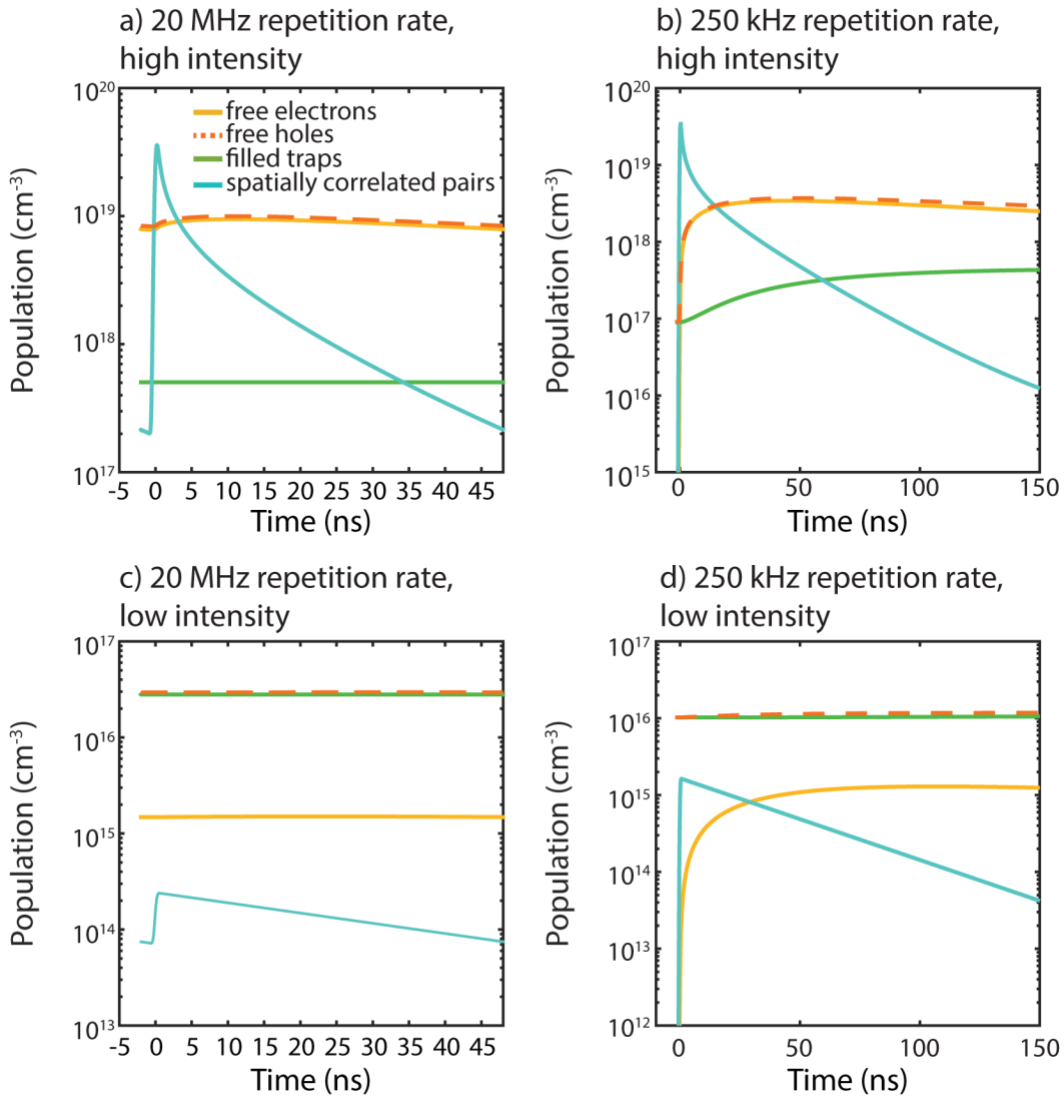

Figure 4-4. Evolution of the populations of various excited state species (a) at 20 MHz and 3.97×10^{-4} J/cm^2/pulse, (b) at 250 kHz and 3.97×10^{-4} J/cm^2/pulse, (c) at 20 MHz and 1.23×10^{-9} J/cm^2/pulse, and (d) at 250 kHz and 1.19×10^{-8} J/cm^2/pulse. Population dynamics of free electrons (yellow), free holes (orange dashed lines), filled traps (green) and spatially-correlated pairs (blue) are shown.

concentration of filled electron traps and photodoped holes (Figure 4-4d). In this regime, these free carrier species dominate at all times. The free electron population is still significantly affected by the dissociation of spatially-correlated pairs, but due to the large degree of photodoping, hole populations are static.[29] In the solar cell regime, therefore, the presence of free electrons and holes, as well as trap states, are the most significant contributors to excited state kinetics for these $MAPbI_3$ crystals. These species contribute to the monomolecular decay kinetics that have been previously observed under low fluence conditions.[13, 29] While focusing on a single excited state species can provide adequate treatment over a small range of excitation powers, both spatially-correlated pairs and free carriers are critical for proper fitting of the entire set of PL decays.

While the importance of both exciton recombination[11, 31] and free electron-hole recombination[13, 36] at high excitation fluences has been debated in the field, the analysis shown here instead focuses more on the notion of geminate vs. non-geminate recombination and can unify the various regimes previously debated. Upon excitation, an exciton is formed and quickly dissociates into a free electron and hole with opposite momenta. Interactions with phonons[49] can rob the free carriers of their momentum and extend the spatial correlation time. Ordinarily, these interactions are inefficient because of low phonon energies, and the correlation time can be assumed to be short.[20, 50] However, a unique feature of the hybrid organic-inorganic perovskite $MAPbI_3$ is that the regular lattice phonons are supplemented by normal vibrational modes of the methylammonium ions. These normal modes are not as strongly coupled to the rest of the lattice and exhibit higher energies (1500 – 3200 cm^{-1}).[51] These higher energy vibrations can more efficiently carry away momentum and lead to longer spatial correlation times. Instead of recoiling apart in opposite directions, the free carriers are quickly robbed of their momentum by the high-energy vibrations and then the thermalized carriers only diffuse apart in a random walk. Since these free electrons and holes have remained spatially-correlated, it is more likely that they will recombine. Herein we use the term “geminate recombination” to refer to this recombination of an electron and hole that originated from the same lattice

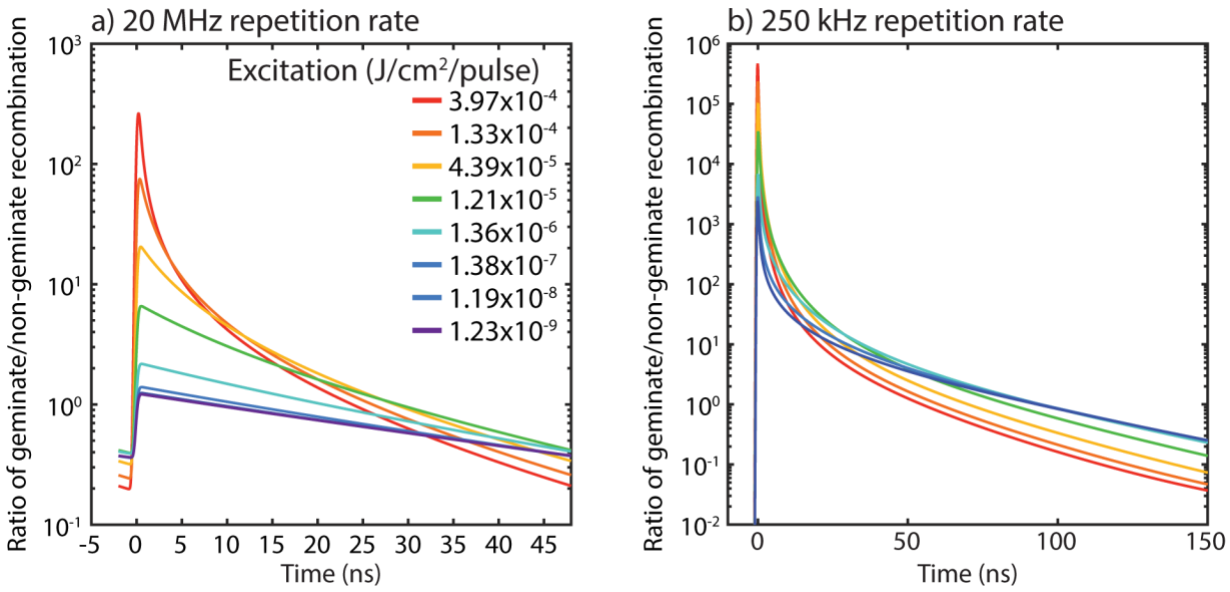

Figure 4-5. Ratio of geminate recombination to non-geminate recombination at (a) 20 MHz and (b) 250 kHz. Excitation fluences from low to high: (—) 1.23×10^{-9}, (—) 1.19×10^{-8}, (—) 1.38×10^{-7}, (—) 1.36×10^{-6}, (—) 1.21×10^{-5}, (—) 4.39×10^{-5}, (—) 1.33×10^{-4}, (—) 3.97×10^{-4} J/cm^2/pulse.

position and excitation event. A spatially-correlated electron-hole pair exists longer than a true exciton, but behaves kinetically like an exciton, i.e. as a single quasi-particle that decays exponentially, and it can still contribute to the observed dynamic Burstein-Moss effect. Our new interpretation allows both the exciton perspective and the free carrier perspective to co-exist without challenging the expectation of rapid exciton dissociation.

Another useful tool that our simulation provides is the ability to analyze which pathways generate the signal during the PL decay. We are particularly interested in the ratio of signal originating from geminate recombination to non-geminate recombination (Figure 4-5). One of the features of the quasi-steady-state is that the relative importance of the non-geminate pathway increases as the quasi-steady-state is established. At 20 MHz, for example, the quasi-steady-state conditions allow electrons and holes to exist in addition to spatially-correlated pairs. These conditions lower the ratio of geminate to non-geminate

recombination for high frequencies. Non-geminate recombination has previously been invoked in perovskite literature,[13, 38] but the inclusion of geminate recombination was essential for proper fitting of

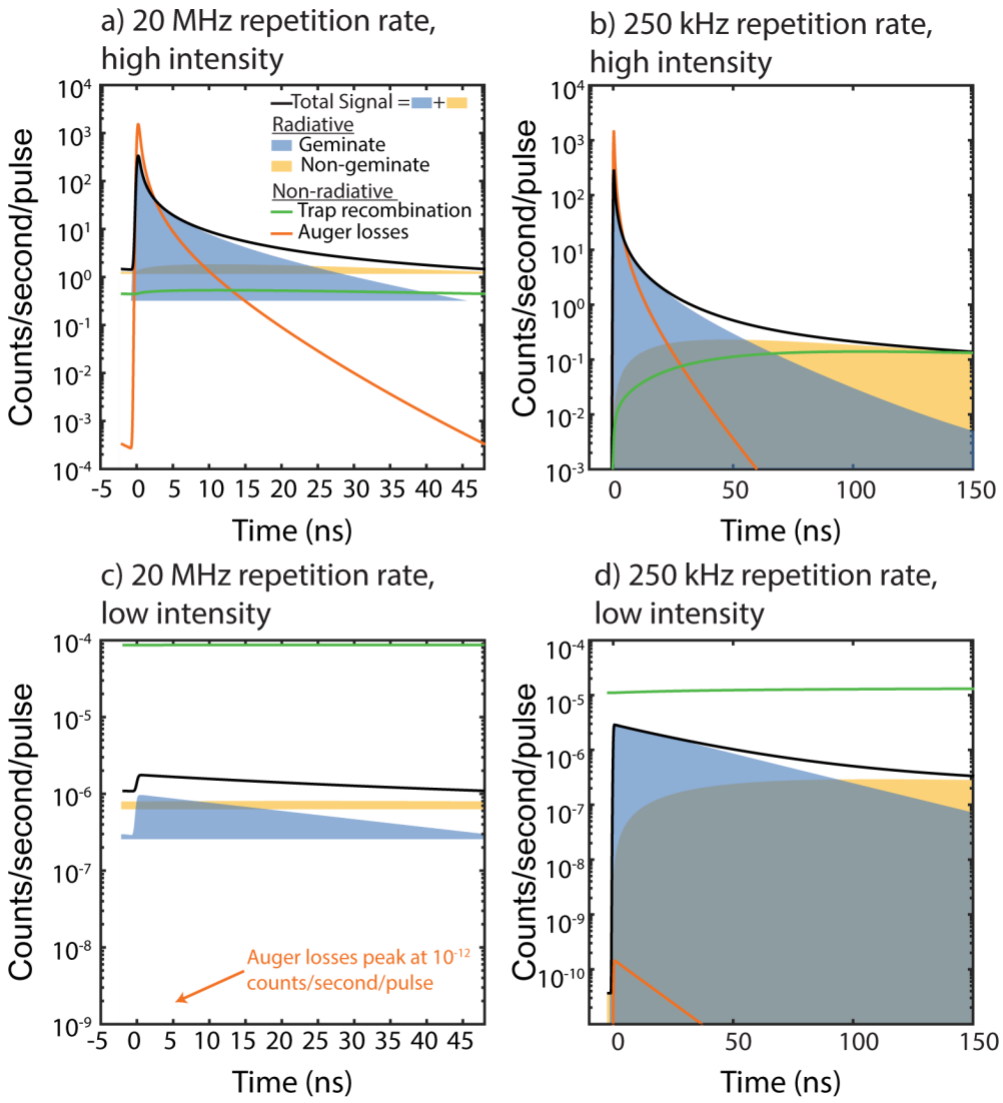

Figure 4-6. Contribution of radiative pathways to overall signal and importance of non-radiative pathways over time (a) at 20 MHz and 3.97×10^{-4} J/cm^2/pulse, (b) at 250 kHz and 3.97×10^{-4} J/cm^2/pulse, (c) at 20 MHz and 1.23×10^{-9} J/cm^2/pulse, and (d) at 250 kHz and 1.19×10^{-8} J/cm^2/pulse. Radiative non-geminate recombination (free electron-hole recombination) (yellow), Auger losses (orange), trap recombination (green) and radiative geminate recombination (includes amplified spontaneous emission and hole catalyzed decays) (blue). The shaded curves (blue and yellow) represent radiative pathways that contribute to the overall signal (black). The Auger losses and trap recombination (orange and green) are included to show at which points these non-radiative pathways affect the shape of the decay and represent the equivalent counts/second/pulse that were lost to these non-radiative pathways.

the data presented here. At high powers and early times, signal generated from geminate recombination greatly exceeds that from non-geminate recombination. This is consistent with the spatially-correlated pairs dominating under the same conditions (Figure 4-4). Geminate recombination dominates the signal until ~100 ns at 250 kHz repetition rate and low intensity (Figure 4-6), even though the population of spatially-correlated pairs is the lowest population at that time (Figure 4-4d). This difference results from the decrease in quantum yield for non-geminate recombination because free holes can recombine non-radiatively with filled traps. While significant geminate recombination until 100 ns would be unlikely in other materials with equally high charge mobilities, the high energy phonons present in $MAPbI_3$ makes this geminate recombination at later times and at lower excitation intensities possible. Geminate recombination pathways, typically attributed to excitons but applied here to spatially-correlated pairs, provide the kinetics needed to reproduce the early decay dynamics of our curves. The dominance of spatially-correlated pairs at high fluences and repetition rates, as opposed to free carriers, suggests facile geminate recombination, a benefit for lasing applications. However, the dominance of geminate pathways even at low fluences may be detrimental for solar devices because wasteful recombination is more competitive. Alternatively, it is possible that the spatial correlation of the pair may reduce the excitation's susceptibility to wasteful trapping processes.

Finally, it is instructive to compare the values in Table 4-2 to other values determined in the literature. In some cases, such as the detrapping rate, k_{dtrp}, agreement is quite close to other reported values: Stranks *et al.* report a trap depopulation rate of 8×10^{-12} cm^3s^{-1}, [29, 40] which is consistent with the value of 3.42×10^{-12} cm^3s^{-1} reported here. In other cases, deviations of 1 – 2 orders of magnitude are seen. In our analysis, however, photoluminescence originates from more than one decay process. This change means that in our model, multiple rate constants collectively contribute to the decay and previously reported values are therefore not necessarily directly comparable to the parameters estimated in our current investigation. For example, the rate of electron-hole recombination has been previously reported

in the range of 10^{-9} – 10^{-11} cm^3s^{-1}, [13, 27, 34, 52-53] while here we report a value of 5.9×10^{-13} cm^3s^{-1}. Our model provides a lower rate for electron-hole recombination because photons are originating from other sources, such as geminate recombination of spatially-correlated pairs. The Auger recombination rate here (1.08×10^{-30} cm^6s^{-1}) is lower than the literature value of ~10^{-28} cm^6s^{-1}.[27, 34, 46] This shift can be attributed to other dissociation pathway of spatially-correlated pairs (k_{dis}) that contributes to losses. Other values, such as those for amplified spontaneous emission, do not have analogs in other models.

We also note that the trap density found here (2.52×10^{18} cm^{-3}) is somewhat higher than the trap density of 10^{16} – 10^{17} cm^{-3} estimated via other TRPL studies,[11-13, 29] and higher than the trap density of 2.0×10^{15} cm^{-3} estimated via current-voltage characteristics.[7] However, estimations of trap density via current-voltage measurements assume an equilibrium behavior while estimates from PL measurements are highly model dependent. In fact, if we simulate our data with the model described by deQuilettes *et al.*[14] we find that our data produces a trap density of 1.58×10^{16} cm^{-3} (Figure 4-7a). We also note that our raw data (both curve shapes and quantum yields) look very similar to data reported in previous TRPL measurements albeit over a limited range.[27, 29, 37, 40] In particular, we observe the turnover in quantum yield at a similar carrier density to that reported by Saba *et al.*[27] and Xing *et al*.[11] The agreement of curve shape, quantum yield, and certain parameters lead us to believe that our model is a more detailed and inclusive extension of existing models and not a complete deviation from them. Critically, use of our model allows simultaneous fitting over many powers and repetition rates. Application of the simpler model of deQuilettes *et al.*[14] to our data results in somewhat better fits at a single fluence, but significantly poorer fits at most other fluences (Figure 4-7b).

4.3.2 Model dependency of trap density

A variety of estimates for trap density have appeared in the literature[12-14, 29] and our estimated value of 2.52×10^{18} cm^{-3} is near the high end of this range. However, the calculation of trap density is highly

model dependent. When we use the non-global model reported by deQuilettes *et al.*[14] to fit our data (Figure 4-7a), we calculate a trap density of 1.58×10^{16} cm^{-3}, a trapping rate of 1.48×10^{-8} cm^3s^{-1}, a monomolecular rate constant of 5.31×10^{6} s^{-1}, and a bimolecular rate constant of 4.33×10^{-11} cm^3s^{-1}, all values that are of the same order of magnitude as those reported by deQuilettes *et al.,* further exemplifying how the trap density is model dependent. While the model of deQuilettes *et al.* performs better than our model at a single normalized PL decay, extension of their model to other powers shows significant deviations at higher and lower excitations where long time behavior is off by multiple orders of magnitude (Figure 4-7b). We also performed partial-global simulations of the model from deQuilettes *et al*. in which we attempted to fit decays from multiple excitation fluences at 20 MHz (250 kHz data was not considered in this test, making for less demanding constraints) repetition rate with one set of parameters (Figure 4-7d). This simulation fails to reproduce the curves at low excitation fluences and all curves at longer times.

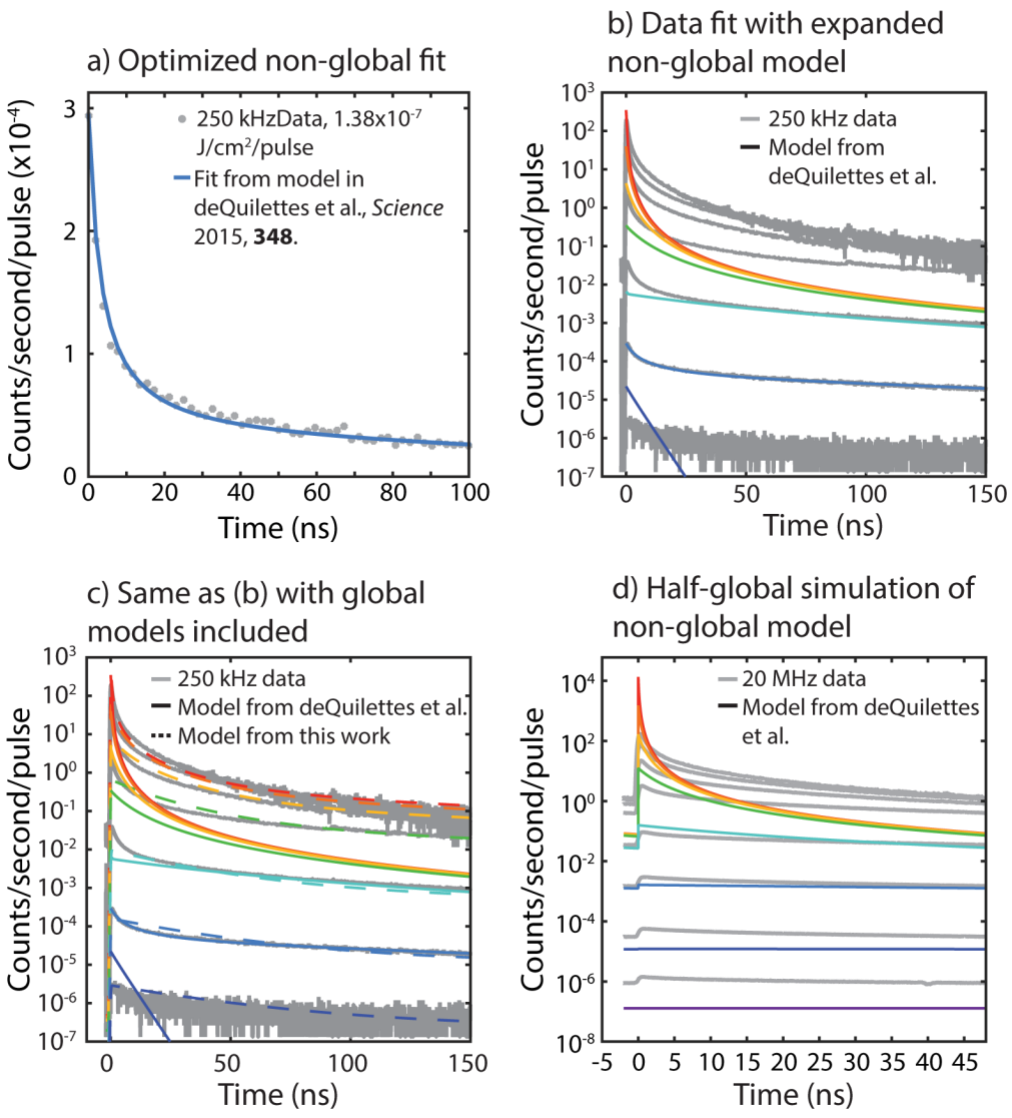

Figure 4-7. A simpler model allows excellent fits at one set of conditions but fails on the global data set. (a) Data collected at 250 kHz repetition rate with excitation fluence of 1.38×10^{-7} J/cm^2/pulse (gray) and an optimized fit using the model in deQuilettes *et al.*, Science 2015, *348*, 683-686. (b) Data collected at 250 kHz repetition rate with the fit from (a) extrapolated to the other excitation fluences, showing poor fits. (c) The same data as (b) with the global fit from the model described in this work included for comparison. Dashed lines are the global fit presented here and solid lines are a non-global fit from deQuilettes *et al.* that has been used to fit the data from the 1.38×10^{-7} J/cm^2/pulse excitation and then extended to the other fluences. (d) Data collected at 20 MHz repetition rate with a simulation of the model in deQuilettes *et al.* where all excitation fluences at only 20 MHz repetition rate were fit with one set of parameters (Note: only the 20 MHz data is fit here, making it a less constrained fit), showing the inability of this model to capture global behavior.) Excitation fluences from high to low: (—) 3.97×10^{-4}, (—) 1.33×10^{-4}, (—) 4.39×10^{-5}, (—) 1.21×10^{-5}, (—) 1.36×10^{-6}, (—) 1.38×10^{-7}, (—) 1.19×10^{-8}, (—) 1.23×10^{-9} J/cm^2/pulse. Dashed lines are the global fit presented here and solid lines are a non-global fit from deQuilettes *et al.* that has been used to fit the data from the 1.38×10^{-7} J/cm^2/pulse excitation and then extended to the other fluences.

4.3.3 Improvement of fit with a partial-global simulation

Fitting the 20 MHz and 250 kHz data simultaneously provided a single set of global rate parameters across all excitation fluences and both repetition rates. Fitting the data from a single repetition rate with one set of parameters ("partial-global"), however, was easier as fewer constraints existed. In Figure 4-8a, we show a fit of the 20 MHz data where only the 20 MHz data was considered in the optimization. Notably, it fits the early time curve of the highest to middle powers somewhat better than the global fit. Using these parameters with a simulation at the 250 kHz repetition rate, however, gives much worse fits to the 250 kHz experimental data. In Figure 4-8b we optimize a fit of 250 kHz data where only the 250 kHz data is considered. The curvature is better captured in this fit, but at the cost of significant reductions in quality of the 20MHz fit. These differences suggest that though our model captures much of the observed behavior, subtle higher-order parameter correlations or minor additional photophysical mechanisms may be needed to perfectly capture the behavior.

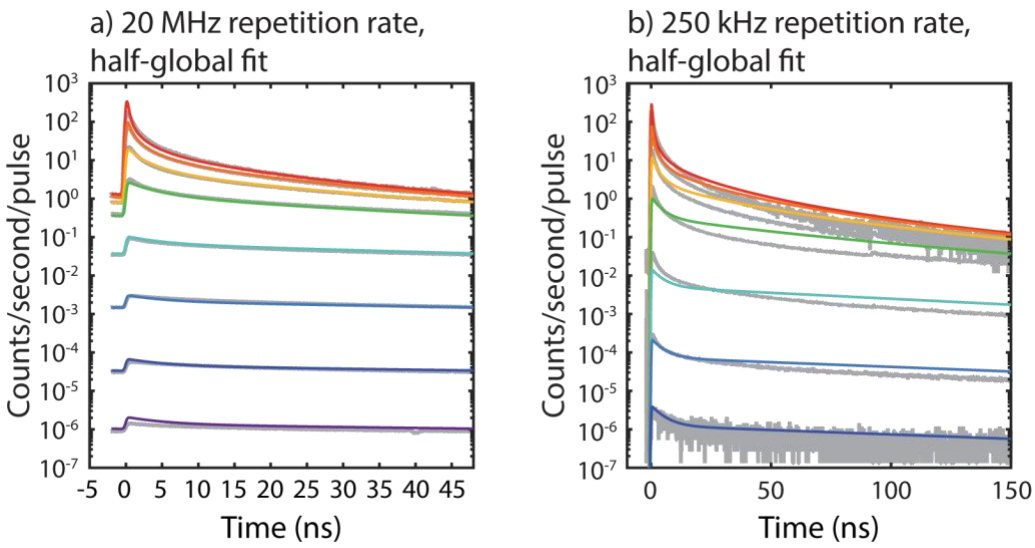

Figure 4-8. Optimized simulations at one repetition rate, showing how better fits can be produced when the constraint of fitting two repetition rates is relaxed. Parameters were optimized for (a) 20 MHz data while considering data at 20 MHz and (b) 250 kHz data while only considering data at 250 kHz. Excitation fluences from high to low: (—) 3.97×10^{-4}, (—) 1.33×10^{-4}, (—) 4.39×10^{-5}, (—) 1.21×10^{-5}, (—) 1.36×10^{-6}, (—) 1.38×10^{-7}, (—) 1.19×10^{-8}, (—) 1.23×10^{-9} J/cm^2/pulse.

Table 4-3. Parameters for 20 MHz fit in Figure 4-8a.

Parameter Name	Parameter Value
Trap Density (T)	5.99×10^{17} cm^{-3}
E-H Recombination Rate Constant (k_{rec})	4.33×10^{-12} cm^3s^{-1}
Trapping Rate Constant (k_{trap})	8.7×10^{-12} cm^3s^{-1}
Trap Decay Rate Constant (k_{dtrp})	1.93×10^{-11} cm^3s^{-1}
ASE 1st Order Rate Constant (k_{SE1})	3.22×10^{-1} s^{-1}
ASE 2nd Order Rate Constant (k_{SE2})	1.3×10^{-11} cm^3s^{-1}
ASE 3rd Order Rate Constant (k_{SE3})	3.2×10^{-34} cm^6s^{-1}
Hole-Catalyzed Spatially-Correlated Pair Decay Rate Constant (k_{hcat})	1.6×10^{-11} cm^3s^{-1}
Spatially-Correlated Pair Dissociation Rate Constant (k_{dis})	1.96×10^{8} s^{-1}
Auger Recombination Rate (k_{Aug})	3.81×10^{-30} cm^6s^{-1}

Table 4-4. Parameters for 250 kHz fit in Figure 4-8b.

Parameter Name	Parameter Value
Trap Density (T)	1.50×10^{18} cm^{-3}
E-H Recombination Rate Constant (k_{rec})	4.62×10^{-12} cm^3s^{-1}
Trapping Rate Constant (k_{trap})	5.4×10^{-12} cm^3s^{-1}
Trap Decay Rate Constant (k_{dtrp})	1.58×10^{-11} cm^3s^{-1}
ASE 1st Order Rate Constant (k_{SE1})	149 s^{-1}
ASE 2nd Order Rate Constant (k_{SE2})	2.9×10^{-11} cm^3s^{-1}
ASE 3rd Order Rate Constant (k_{SE3})	1.2×10^{-32} cm^6s^{-1}
Hole-Catalyzed Spatially-Correlated Pair Decay Rate Constant (k_{hcat})	1.5×10^{-11} cm^3s^{-1}
Spatially-Correlated Pair Dissociation Rate Constant (k_{dis})	1.14×10^{8} s^{-1}
Auger Recombination Rate (k_{Aug})	1.30×10^{-30} cm^6s^{-1}

4.3.4 An alternate view of non-geminate recombination

An alternative view of the scheme presented in Figure 4-3 is presented in Figure 4-9. Before recombination is possible, an electron and hole must come together and become a spatially-correlated

pair. Because the electron and hole were not generated from the same excitation event, we distinguish them here as a non-geminate spatially-correlated pair. We now show the recombination of a free electron and hole as a 2-step process: the formation of the spatially-correlated non-geminate pair is a reversible process with a forward and reverse rate constant, and the recombination of the spatially-correlated non-geminate pair to the ground state. In the limit where the rate at which the electron and hole encounter each other (k_{rec}) is slow, the kinetics of the 2-step decay process is determined entirely by the first step ($k_{rec}[E][H]$), as is used in Figure 4-3. We have therefore decided to represent the two steps together as a single decay process in Figure 4-3 for simplicity.

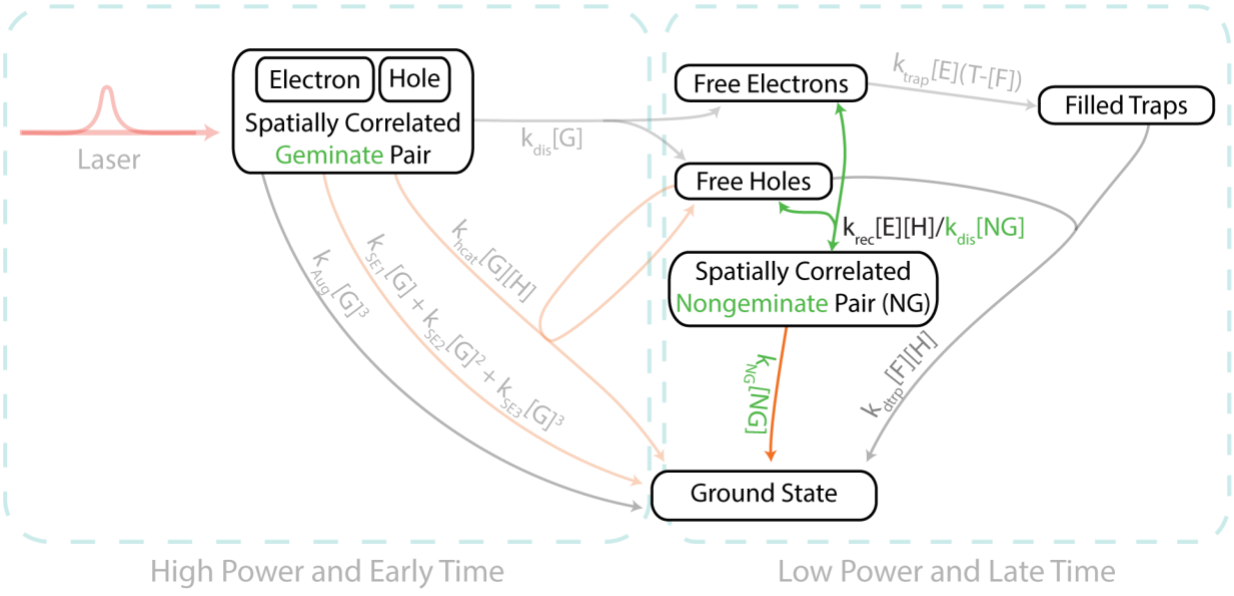

Figure 4-9. Alternative version of Figure 4-3 in which spatially-correlated non-geminate pairs are explicitly included. Green has been used to highlight important changes.

4.3.5 A second $MAPbI_3$ perovskite plate

TRPL decays from a second plate are shown in Figure 4-10, gray. The trends for the nanoplate in Figure 4-10 are qualitatively similar to those in Figure 4-2. This plate showed slight pile-up error at the highest excitation fluence at 250 kHz (data not shown), so this data was excluded from the simulation analysis. We applied our global simulation model to this data (Figure 4-10, multiple colors) and extracted the rate parameters unique to this data set (Table 4-5). While the model did not capture the fast decay

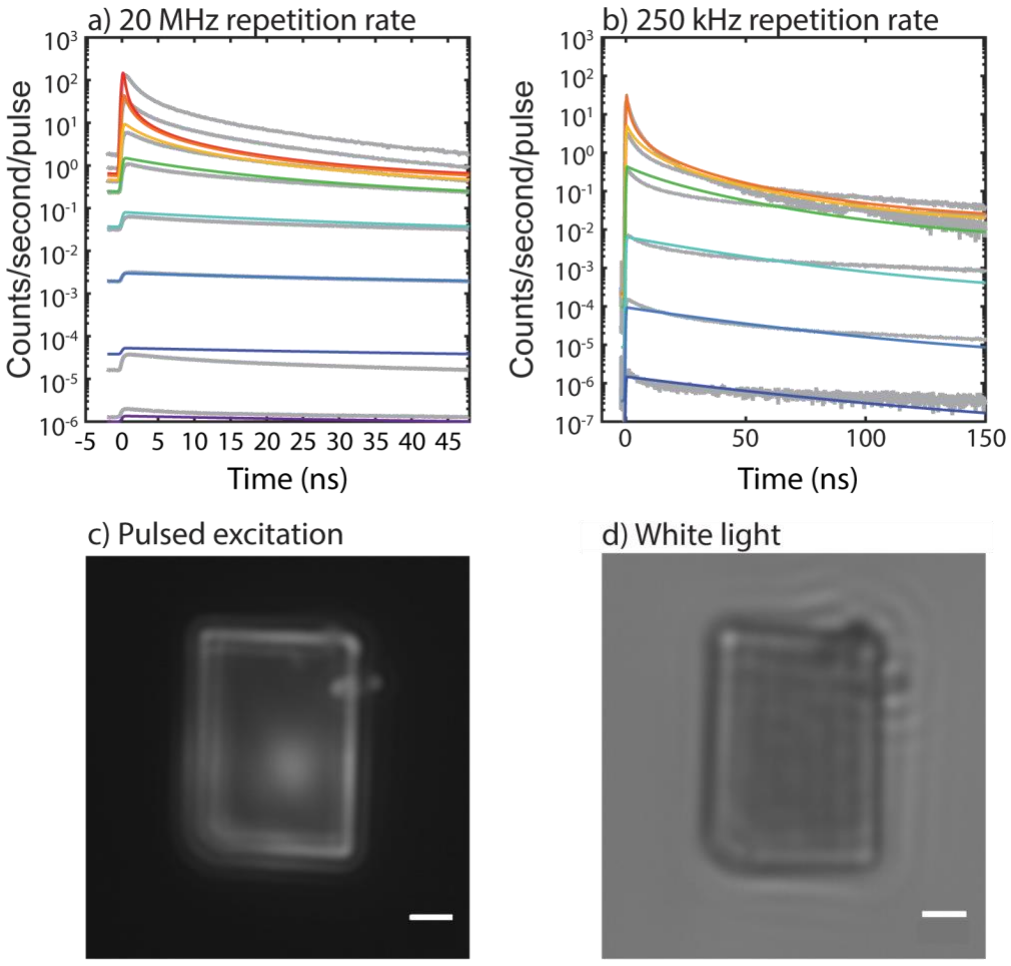

Figure 4-10. $MAPbI_3$ perovskite TRPL data for another single nanoplate. TRPL data at (a) 20 MHz and (b) 250 kHz repetition rates. The highest power curve at 250 kHz was removed due to pile-up error. (c) PL image of the perovskite plate under pulsed excitation and (d) white light image of the same plate. Excitation fluences from high to low: (—) 3.97×10^{-4}, (—) 1.33×10^{-4}, (—) 4.39×10^{-5}, (—) 1.21×10^{-5}, (—) 1.36×10^{-6}, (—) 1.38×10^{-7}, (—) 1.19×10^{-8}, (—) 1.23×10^{-9} J/cm^2/pulse. Scale bar is 2 µm.

dynamics at the high fluences of the 20 MHz repetition rate data, it fit all other fluences qualitatively as well as those shown in Figure 4-2. The rate parameters used to fit this data set, Table 4-5, are similar to those for the plate discussed earlier and summarized in Table 4-2.

Table 4-5. Simulation parameters used for global fitting in Figure 4-10.

Parameter Name	Parameter Value
Trap Density (T)	1.79×10^{18} cm^{-3}
E-H Recombination Rate Constant (k_{rec})	1.81×10^{-13} cm^3s^{-1}
Trapping Rate Constant (k_{trap})	2.6×10^{-13} cm^3s^{-1}
Trap Decay Rate Constant (k_{dtrp})	5.29×10^{-12} cm^3s^{-1}
ASE 1st Order Rate Constant (k_{SE1})	345 s^{-1}
ASE 2nd Order Rate Constant (k_{SE2})	7.3×10^{-12} cm^3s^{-1}
ASE 3rd Order Rate Constant (k_{SE3})	1.6×10^{-35} cm^6s^{-1}
Hole-Catalyzed Spatially-Correlated Pair Decay Rate Constant (k_{hcat})	3.7×10^{-12} cm^3s^{-1}
Spatially-Correlated Pair Dissociation Rate Constant (k_{dis})	1.66×10^{7} s^{-1}
Auger Recombination Rate (k_{Aug})	3.06×10^{-30} cm^6s^{-1}

*4.3.6 **Photostability of samples***

$MAPbI_3$ perovskites are sensitive to moisture and undergo photodegradation. In order to test the photostability of these materials, we recorded TRPL traces from the lowest fluence to the highest fluence and then repeated the series on the same plate. The decays on the first sequence (Figure 4-11, red, dark green and purple dashed) are comparable to those on the second series (orange, light green, light blue). There is a small difference in the intensity of the two green traces, but the decay slope remains consistent. This difference implies that photostability may affect the absolute signal level by a small amount, and that the shape of the decay is unchanged.

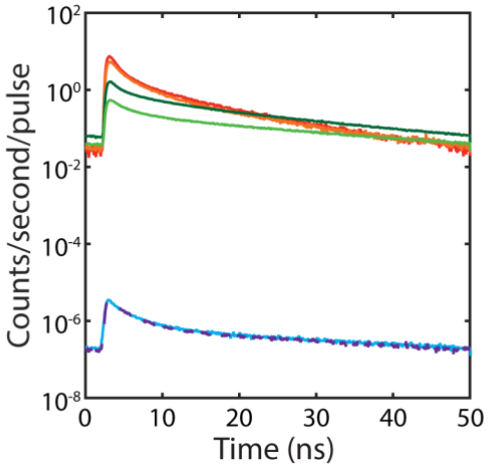

Figure 4-11. Photostability of a $MAPbI_3$ perovskite plate at 20 MHz excitation. The excitation fluences used were 3.97×10^{-4} (red/orange), 1.33×10^{-4} (light/dark green) and 1.23×10^{-9} (light blue/purple dashed) J/cm^2/pulse. The first series taken was purple dashed line, dark green and red, followed by light blue, light green and orange.

4.3.7 Characterization of $MAPbI_3$ perovskite plates

The scanning electron microscopy was performed using a LEO SUPRA 55 VP field-emission SEM operated at 1.5 kV (Figure 4-12a). The optical image of the $MAPbI_3$ nanostrucutres was taken using an optical microscope (Olympus, BX51M) (Figure 4-12b). The photoluminescence of a single nanoplate was collected with an Aramis Confocal Raman microscope using a 532 nm laser source (Figure 4-12c). The UV–vis absorption of the nanostructured film was collected using a JASCO V-550 spectrometer (Figure 4-12c). Absorbance and emission PL from a single nanoplate (Figure 4-12c) are characteristic of this material.[5]

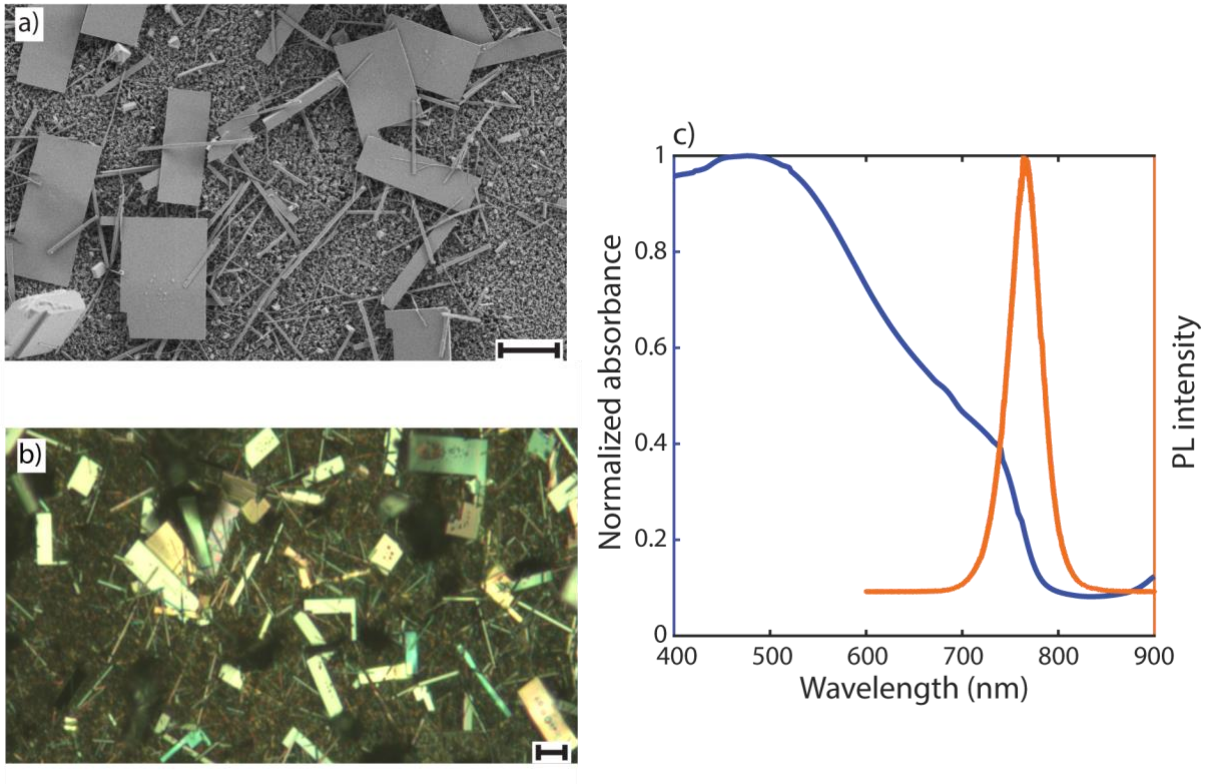

Figure 4-12. Characterization of $MAPbI_3$ perovskite nanostructures. (a) Scanning electron microscope (SEM) image and (b) optical image of $MAPbI_3$ perovskite nanostructures. (c) Absorption spectra of $MAPbI_3$ nanostructured film and PL emission spectra of a single nanoplate. Scale bars are 5 µm.

4.4 Conclusion

We have studied TRPL of individual $MAPbI_3$ perovskite nanoplates over 5 orders of magnitude in excitation power and at two very different repetition rates. These data were globally fit using a simulation that accounts for the radiative and non-radiative decay pathways of all excited state species. This simulation allows us to define the dynamics of each charge carrier species, identify the important pathways that dominate at different times, repetition rates, and charge carrier densities, and predict the dependence of the quantum efficiency on charge carrier density. Our simulation not only captures the known dynamics

previously understood but also requires an excited state species distinct from free carriers at early times that we believe to be spatially-correlated electron-hole pairs. Further, our analysis indicates that geminate recombination of these spatially-correlated pairs is responsible for the signal at high excitation fluences and at early times, while non-geminate bimolecular free electron-hole recombination and trap-mediated decay dominate at low excitation fluences and longer times. The experimental and simulation data presented here introduces two novel concepts for perovskite photophysics: spatially-correlated electron-hole pairs as another contributor to decay dynamics possessing some of the characteristics of excitons, and the dominance of geminate recombination of these spatially-correlated pairs, concepts whose necessity is apparent only when presented with a global unnormalized set of TRPL data. These additions provide a rationale for how these two regimes (solar cell and lasing) can be viewed as two extremes of a single larger model, thus unifying the two sides of the exciton vs. free carrier debate in $MAPbI_3$ perovskites. Consequently, this model – which accounts for previously disregarded pieces of data (i.e. absolute PL intensity) – has highlighted limitations of current modeling methods and allowed us to expand our understanding of the fundamental photoexcitations. Future work will entail extending this model and approach to other perovskite materials such as cesium and alloyed cation perovskites.

4.5 Experimental Section

4.5.1 Synthesis of $MAPbI_3$ perovskite nanoplates

All chemicals and reagents were purchased from Sigma-Aldrich (St. Louis, MO). The CH_3NH_3I (MAI) was synthesized by slowly mixing methylamine (40 % in methanol) and HI (57 wt % in water) in an evaporating dish in a molar ratio of 1:1. The MAI precipitated as the solvent was carefully removed at 100 °C on a hot plate. The product was collected by filtration and washed with diethyl ether several times. Finally, the product was recrystallized in ethanol to form white crystals, and dried at 50 °C in an oven for 24 hours.[17, 19] The perovskite nanoplate film was synthesized from a $PbAc_2$ thin film immersed in a CH_3NH_3I

solution in isopropanol with a concentration of 40 mg/mL for ~20 h reaction time following previous reported procedures.[17, 19] $PbAc_2$ thin film was prepared by drop-casting 100 mg/mL $PbAc_2 \cdot 3H_2O$ aqueous solution on a glass slide at 50 ˚C in an oven, and then dried for another 1 h at 50 ˚C. We kept spreading out the lead acetate solution to obtain a uniform film on the substrate during the deposition process. After reaction, the $CH_3NH_3PbI_3$ perovskite samples were taken out and subsequently dipped into isopropanol to remove the residual salt on the film, and then were dried under a stream of N_2.

4.5.2 Experimental set-up and considerations

$MAPbI_3$ perovskite nanocrystals were excited with a 639 nm pulsed laser (500 ps FWHM, Figure 4-13) focused with a 40x air objective (NA 0.75). This setup is similar to others that have been used for TRPL experiments with one notable exception: the emission signal was reduced with neutral density (ND) filters (Figure 4-14). Dampening the signal was necessary to prevent damage to our APD and prevent pile-up error in photon counting (Figure 4-15). Pile-up error occurs when the probability of detecting a photon exceeds 5 % of the pulse rate (Figure 4-15b, pink)[54]. Inserting ND filters allowed us to eliminate any influence of this process on decay kinetics (Figure 4-15b, blue and purple).

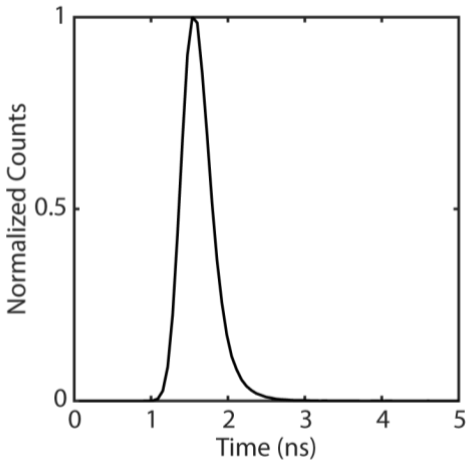

Figure 4-13. Instrument response function with a full width at half maximum of 500 ps.

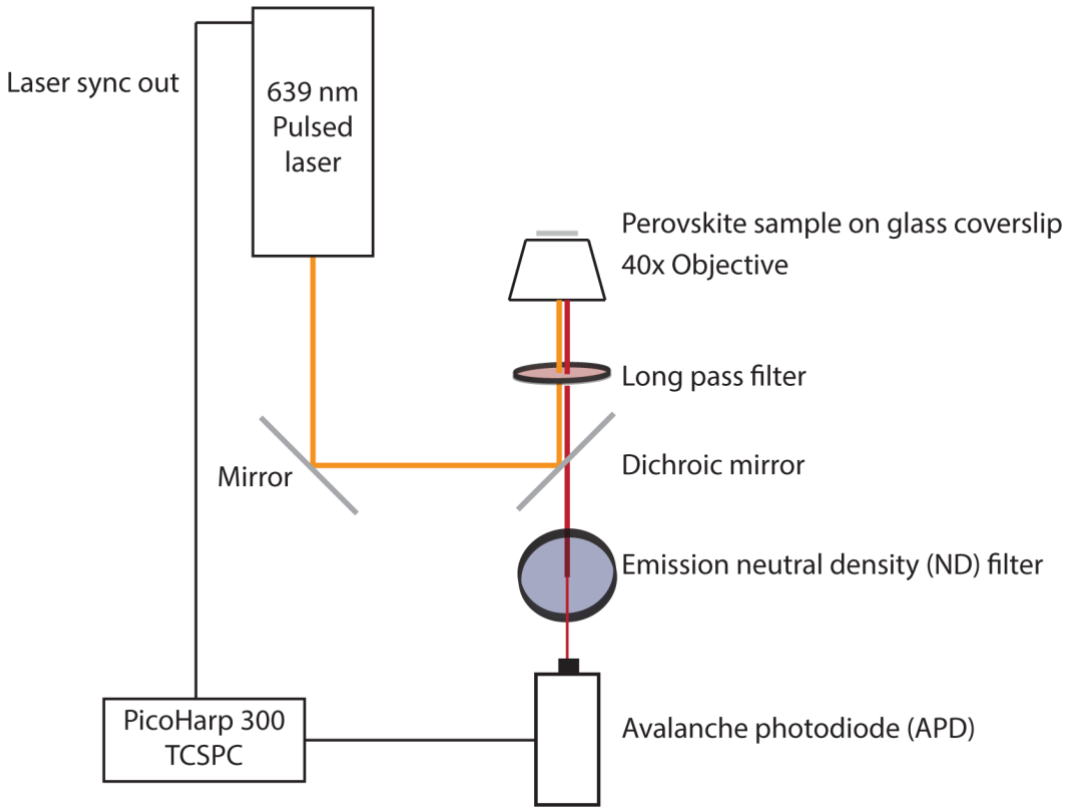

Figure 4-14. Experimental setup for perovskite time-resolved photoluminescence data collection.

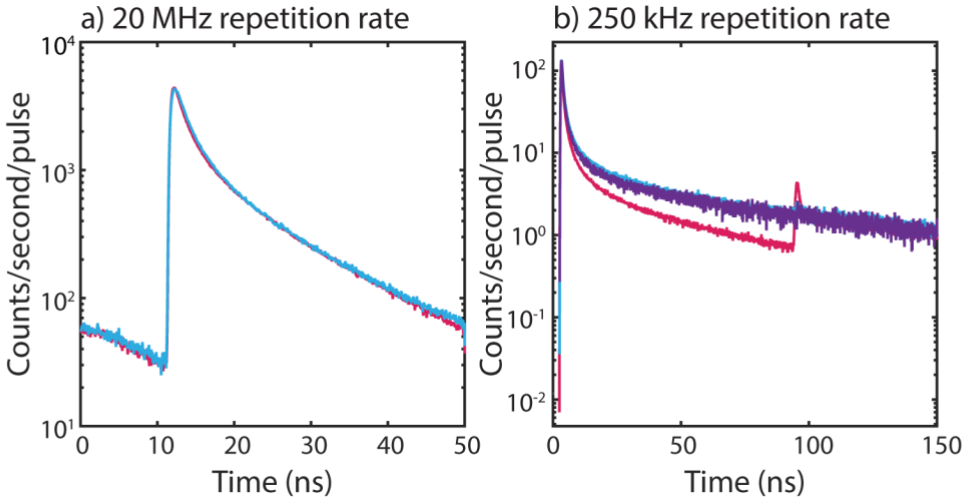

Figure 4-15. Effect of pile-up error at 3.97×10^{-4} J/cm^2/pulse excitation with (a) 20 MHz and (b) 250 kHz repetition rates. (a) Signal was dampened by 9 (pink) or 10 (blue) orders of magnitude in the emission path. (b) Signal was dampened by 7 (pink), 8 (blue) or 9 (purple) orders of magnitude in the emission path. The pink curve in (b) shows pile-up error evidenced by a steeper slope and second pulse around 100 ns. Filters were carefully selected to avoid the regime where pile-up error impacts decay kinetics.

4.5.3 Time-resolved photoluminescence

The single-crystal $MAPbI_3$ nanoplates were transferred to a methanol rinsed and plasma cleaned (300 W, 3 min) glass coverslip (Fisher Scientific) from the growth surface using a dry contact method and studied on a home-built confocal fluorescence microscope (Figure 4-14). Excitation was provided through the coverslip with a 639 nm picosecond pulsed diode laser (LDH-D-C-640, PicoQuant, Berlin, Germany). The excitation light (fluences used: 3.97×10^{-4}, 1.33×10^{-4}, 4.39×10^{-5}, 1.21×10^{-5}, 1.36×10^{-6}, 1.38×10^{-7}, 1.19×10^{-8}, 1.23×10^{-9} J/cm^2/pulse) was focused to a 0.99 µm^2 spot through a CFI Plan Fluor 40x air objective (NA 0.75) (Nikon, Melville, NY) mounted on a Nikon Eclipse Ti-U inverted microscope, and the emission was collected through the same objective. The emission passed through a 635 nm dichroic beamsplitter (Semrock, Rochester NY), a 635 nm long-pass filter (Semrock), and a 200 µm pinhole (Newport Corporation, Irvine, CA). The instrument response function was 500 ps full width at half maximum (Figure 4-13). The filtered signal was then attenuated using absorptive neutral density filters (Thorlabs, Newton, NJ) in order to ensure

≤ 1 photon is detected for each excitation pulse (Figure 4-15). Emission was detected on a τ-SPAD single photon counting module (PicoQuant) and recorded using a PicoHarp 300 time-correlated single photon counting module (PicoQuant) with 64 ps resolution. Images of the nanoplates were recorded with a high-resolution CMOS camera (Thorlabs) (Figure 4-1). The injected carrier density, n_0, is calculated[13] as $n_0 = j\alpha$, where j is the pump fluence (photons/cm^2) and α is the absorption coefficient of $MAPbI_3$ (4.561×10^4 cm^{-1} at 639 nm)[10]. This calculation assumes that each photon leads to an excited state species. Photo-degradation and/or photo-curing[55-56] of perovskite samples was minimal under these conditions (Figure 4-11).

4.5.4 Simulation

The simulation evaluated rate equations for all species and updated excited state populations at time steps of 5 ps. These rate equations are shown in Table 4-1. The excitation beam was modeled as a Gaussian profile in time and was included as an additional term to the spatially-correlated pair rate equation. At the end of a period, the simulation was repeated with initial state populations equal to those at the final time step of the period. This strategy was repeated until all populations converged to a steady-state, and the final concentrations were saved for analysis. The photoluminescence output by the numerical simulation was scaled by a constant factor to account for the collection efficiency of our experimental setup.

Rate constants and the total trap density were used as fitting parameters to simultaneously optimize the simulation to the entire set of experimental data (all excitation powers at 20 MHz and 250 kHz repetition rates). First, a genetic fitting routine was used to find the global minimum well in the very large parameter space. Then a simplex fitting routine was used to efficiently minimize the error within that well. To optimize the global fit, the squares of the differences in the logarithm of the experimental and simulation intensities were summed and minimized. Taking the logarithm of the data ensured that high and low

excitation fluences were weighted equally. For the 250 kHz curves, only the first 120 ns of data were included in the error calculation to avoid de-emphasizing the important early time regime. Second and mixed partial derivatives of the error function were found numerically to generate a Hessian matrix. This matrix was then inverted to find the variances, reported here (Table 4-2) as estimated errors for the parameters. Note that the optimization was entirely insensitive to two parameters, k_{SE1} and k_{SE3}, but they were included here for completeness.

4.5.5 Quantum yield calculation

The experimental TRPL decay was integrated over time to calculate the detected counts/second/pulse emitted from the sample. The signal was then divided by the excitation fluence to find the relative quantum yield. For the simulation data, integrating the photoluminescence output and dividing by excitation power gave absolute quantum yields. The constant scaling factor described above in the simulation was then applied to the experimental relative quantum yields to yield the data shown in Figure 4-2c and Figure 4-2d.

4.5.6 Code availability

Global analysis code in Python is available on github.com (http://dx.doi.org/10.5281/zenodo.1313878).

4.6 References

1. Li, X.; Bi, D.; Yi, C.; Décoppet, J.-D.; Luo, J.; Zakeeruddin, S. M.; Hagfeldt, A.; Grätzel, M., A Vacuum Flash–Assisted Solution Process for High-Efficiency Large-Area Perovskite Solar Cells. *Science* **2016**.

2. Green, M. A.; Ho-Baillie, A.; Snaith, H. J., The emergence of perovskite solar cells. *Nat. Photonics* **2014**, *8*, 506-514.

3. Eperon, G. E.; Stranks, S. D.; Menelaou, C.; Johnston, M. B.; Herz, L. M.; Snaith, H. J., Formamidinium Lead Trihalide: a Broadly Tunable Perovskite for Efficient Planar Heterojunction Solar Cells. *Energy Environ. Sci.* **2014**, *7*, 982-988.

4. Kim, H. S.; Lee, C. R.; Im, J. H.; Lee, K. B.; Moehl, T.; Marchioro, A.; Moon, S. J.; Humphry-Baker, R.; Yum, J. H.; Moser, J. E., et al., Lead Iodide Perovskite Sensitized All-Solid-State Submicron Thin Film Mesoscopic Solar Cell with Efficiency Exceeding 9%. *Sci. Rep.* **2012**, *591* 1-7.

5. Fu, Y.; Meng, F.; Rowley, M. B.; Thompson, B. J.; Shearer, M. J.; Ma, D.; Hamers, R. J.; Wright, J. C.; Jin, S., Solution Growth of Single Crystal Methylammonium Lead Halide Perovskite Nanostructures for Optoelectronic and Photovoltaic Applications. *J. Am. Chem. Soc.* **2015**, *137*, 5810-5818.

6. Burschka, J.; Pellet, N.; Moon, S.-J.; Humphry-Baker, R.; Gao, P.; Nazeeruddin, M. K.; Gratzel, M., Sequential Deposition as a Route to High-Performance Perovskite-Sensitized Solar Cells. *Nature* **2013**, *499*, 316-319.

7. Dong, Q.; Fang, Y.; Shao, Y.; Mulligan, P.; Qiu, J.; Cao, L.; Huang, J., Electron-Hole Diffusion Lengths >175 μm in Solution-Grown CH3NH3PbI3 Single Crystals. *Science* **2015**, *347*, 967-969.

8. You, J.; Hong, Z.; Yang, Y.; Chen, Q.; Cai, M.; Song, T.-B.; Chen, C.-C.; Lu, S.; Liu, Y.; Zhou, H., et al., Low-Temperature Solution-Processed Perovskite Solar Cells with High Efficiency and Flexibility. *ACS Nano* **2014**, *8*, 1674-1680.

9. Stranks, S. D.; Eperon, G. E.; Grancini, G.; Menelaou, C.; Alcocer, M. J.; Leijtens, T.; Herz, L. M.; Petrozza, A.; Snaith, H. J., Electron-Hole Diffusion Lengths Exceeding 1 Micrometer in an Organometal Trihalide Perovskite Absorber. *Science* **2013**, *342*, 341-344.

10. Xing, G.; Mathews, N.; Sun, S.; Lim, S. S.; Lam, Y. M.; Gratzel, M.; Mhaisalkar, S.; Sum, T. C., Long-range balanced electron- and hole-transport lengths in organic-inorganic CH3NH3PbI3. *Science* **2013**, *342*, 344-347.

11. Xing, G.; Mathews, N.; Lim, S. S.; Yantara, N.; Liu, X.; Sabba, D.; Grätzel, M.; Mhaisalkar, S.; Sum, T. C., Low-Temperature Solution-Processed Wavelength-Tunable Perovskites for Lasing. *Nat. Mater.* **2014**, *13*, 476-480.

12. Draguta, S.; Thakur, S.; Morozov, Y. V.; Wang, Y.; Manser, J. S.; Kamat, P. V.; Kuno, M., Spatially Non-Uniform Trap State Densities in Solution-Processed Hybrid Perovskite Thin Films. *J. Phys. Chem. Lett.* **2016**, *7*, 715-721.

13. Manser, J. S.; Kamat, P. V., Band Filling with Free Charge Carriers in Organometal Halide Perovskites. *Nat. Photonics* **2014**, *8*, 737-743.

14. deQuilettes, D. W.; Vorpahl, S. M.; Stranks, S. D.; Nagaoka, H.; Eperon, G. E.; Ziffer, M. E.; Snaith, H. J.; Ginger, D. S., Impact of Microstructure on Local Carrier Lifetime in Perovskite Solar Cells. *Science* **2015**, *348*, 683-686.

15. Willa, K.; Hausermann, R.; Mathis, T.; Facchetti, A.; Chen, Z.; Batlogg, B., From Organic Single Crystals to Solution Processed Thin-Films: Charge Transport and Trapping with Varying Degree of Order. *J. Appl. Phys.* **2013**, *133707* 1-7.

16. Noh, J. H.; Im, S. H.; Heo, J. H.; Mandal, T. N.; Seok, S. I., Chemical Management for Colorful, Efficient, and Stable Inorganic-Organic Hybrid Nanostructured Solar Cells. *Nano Lett.* **2013**, *13*, 1764-1769.

17. Zhu, H.; Fu, Y.; Meng, F.; Wu, X.; Gong, Z.; Ding, Q.; Gustafsson, M. V.; Trinh, M. T.; Jin, S.; Zhu, X. Y., Lead Halide Perovskite Nanowire Lasers with Low Lasing Thresholds and High Quality Factors. *Nat. Mater.* **2015**, *14*, 636-642.

18. Deschler, F.; Price, M.; Pathak, S.; Klintberg, L. E.; Jarausch, D. D.; Higler, R.; Huttner, S.; Leijtens, T.; Stranks, S. D.; Snaith, H. J., et al., High Photoluminescence Efficiency and Optically Pumped Lasing in Solution-Processed Mixed Halide Perovskite Semiconductors. *J. Phys. Chem. Lett.* **2014**, *5*, 1421-1426.

19. Fu, Y.; Zhu, H.; Schrader, A. W.; Liang, D.; Ding, Q.; Joshi, P.; Hwang, L.; Zhu, X. Y.; Jin, S., Nanowire Lasers of Formamidinium Lead Halide Perovskites and Their Stabilized Alloys with Improved Stability. *Nano Lett.* **2016**, *16*, 1000-1008.

20. Saba, M.; Quochi, F.; Mura, A.; Bongiovanni, G., Excited State Properties of Hybrid Perovskites. *Acc. Chem. Res.* **2016**, *49*, 166-173.

21. Pazos-Outón, L. M.; Szumilo, M.; Lamboll, R.; Richter, J. M.; Crespo-Quesada, M.; Abdi-Jalebi, M.; Beeson, H. J.; Vrućinić, M.; Alsari, M.; Snaith, H. J., et al., Photon Recycling in Lead Iodide Perovskite Solar Cells. *Science* **2016**, *351*, 1430-1433.

22. Zhu, X. Y.; Podzorov, V., Charge Carriers in Hybrid Organic-Inorganic Lead Halide Perovskites Might Be Protected as Large Polarons. *J. Phys. Chem. Lett.* **2015**, *6*, 4758-4761.

23. Liu, D.; Kelly, T. L., Perovskite Solar Cells with a Planar Heterojunction Structure Prepared Using Room-Temperature Solution Processing Techniques. *Nat. Photonics* **2014**, *8*, 133-138.

24. Sheng, C.; Zhang, C.; Zhai, Y.; Mielczarek, K.; Wang, W.; Ma, W.; Zakhidov, A.; Vardeny, Z. V., Exciton Versus Free Carrier Photogeneration in Organometal Trihalide Perovskites Probed by Broadband Ultrafast Polarization Memory Dynamics. *Phys. Rev. Lett.* **2015**, *116601* 1-5.

25. Malinkiewicz, O.; Yella, A.; Lee, Y. H.; Espallargas, G. M.; Graetzel, M.; Nazeeruddin, M. K.; Bolink, H. J., Perovskite Solar Cells Employing Organic Charge-Transport Layers. *Nat. Photonics* **2014**, *8*, 128-132.

26. Jung, H. S.; Park, N. G., Perovskite Solar Cells: from Materials to Devices. *Small* **2015**, *11*, 10-25.

27. Saba, M.; Cadelano, M.; Marongiu, D.; Chen, F. P.; Sarritzu, V.; Sestu, N.; Figus, C.; Aresti, M.; Piras, R.; Lehmann, A. G., et al., Correlated Electron-Hole Plasma in Organometal Perovskites. *Nat. Commun.* **2014**, *5049* 1-10.

28. Eaton, S. W.; Lai, M.; Gibson, N. A.; Wong, A. B.; Dou, L.; Ma, J.; Wang, L. W.; Leone, S. R.; Yang, P., Lasing in Robust Cesium Lead Halide Perovskite Nanowires. *Proc. Natl. Acad. Sci. U. S. A.* **2016**, *113*, 1993-1998.

29. Stranks, S. D.; Burlakov, V. M.; Leijtens, T.; Ball, J. M.; Goriely, A.; Snaith, H. J., Recombination Kinetics in Organic-Inorganic Perovskites: Excitons, Free Charge, and Subgap States. *Phys. Rev. Appl.* **2014**, *034007* 1-8.

30. Even, J.; Pedesseau, L.; Katan, C., Analysis of Multivalley and Multibandgap Absorption and Enhancement of Free Carriers Related to Exciton Screening in Hybrid Perovskites. *J. Phys. Chem. C* **2014**, *118*, 11566-11572.

31. D'Innocenzo, V.; Grancini, G.; Alcocer, M. J. P.; Kandada, A. R. S.; Stranks, S. D.; Lee, M. M.; Lanzani, G.; Snaith, H. J.; Petrozza, A., Excitons Versus Free Charges in Organo-Lead Tri-Halide Perovskites. *Nat. Commun.* **2014**, *3586* 1-6.

32. Lin, Q.; Armin, A.; Nagiri, R. C. R.; Burn, P. L.; Meredith, P., Electro-Optics of Perovskite Solar Cells. *Nat. Photonics* **2015**, *9*, 106-112.

33. Yang, Y.; Ostrowski, D. P.; France, R. M.; Zhu, K.; van de Lagemaat, J.; Luther, J. M.; Beard, M. C., Observation of a Hot-Phonon Bottleneck in Lead-Iodide Perovskites. *Nat. Photonics* **2015**, *10*, 53-59.

34. Yang, Y.; Yang, M.; Li, Z.; Crisp, R.; Zhu, K.; Beard, M. C., Comparison of Recombination Dynamics in CH3NH3PbBr3 and CH3NH3PbI3 Perovskite Films: Influence of Exciton Binding Energy. *J. Phys. Chem. Lett.* **2015**, *6*, 4688-4692.

35. Tanaka, K.; Takahashi, T.; Ban, T.; Kondo, T.; Uchida, K.; Miura, N., Comparative Study on the Excitons in Lead-Halide-Based Perovskite-Type Crystals CH3NH3PbBr3 CH3NH3PbI3. *Solid State Commun.* **2003**, *127*, 619-623.

36. Yamada, Y.; Nakamura, T.; Endo, M.; Wakamiya, A.; Kanemitsu, Y., Photocarrier Recombination Dynamics in Perovskite CH3NH3PbI3 for Solar Cell Applications. *J. Am. Chem. Soc.* **2014**, *136*, 11610-11613.

37. Yamada, Y.; Yamada, T.; Phuong, L. Q.; Maruyama, N.; Nishimura, H.; Wakamiya, A.; Murata, Y.; Kanemitsu, Y., Dynamic Optical Properties of CHNHPbI Single Crystals As Revealed by One- and Two-Photon Excited Photoluminescence Measurements. *J. Am. Chem. Soc.* **2015**, *137*, 10456–10459.

38. Stamplecoskie, K. G.; Manser, J. S.; Kamat, P. V., Dual Nature of the Excited State in Organic-Inorganic Lead Halide Perovskites. *Energy Environ. Sci.* **2015**, *8*, 208-215.

39. Noel, N. K.; Abate, A.; Stranks, S. D.; Parrott, E. S.; Burlakov, V. M.; Goriely, A.; Snaith, H. J., Enhanced Photoluminescence and Solar Cell Performance via Lewis Base Passivation of Organic-Inorganic Lead Halide Perovskites. *ACS Nano* **2014**, *8*, 9815-9821.

40. Wehrenfennig, C.; Liu, M.; Snaith, H. J.; Johnston, M. B.; Herz, L. M., Homogeneous Emission Line Broadening in the Organo Lead Halide Perovskite CH3NH3PbI3–xClx. *J. Phys. Chem. Lett.* **2014**, *5*, 1300-1306.

41. Pelant, I.; Valenta, J., *Luminescence Spectroscopy of Semiconductors*; Oxford University Press: Oxford ; New York, 2012, p 542.

42. Ponseca, C. S.; Savenije, T. J.; Abdellah, M.; Zheng, K.; Yartsev, A.; Pascher, T.; Harlang, T.; Chabera, P.; Pullerits, T.; Stepanov, A., et al., Organometal Halide Perovskite Solar Cell Materials Rationalized: Ultrafast Charge Generation, High and Microsecond-Long Balanced Mobilities, and Slow Recombination. *J. Am. Chem. Soc.* **2014**, *136*, 5189-5192.

43. Ponseca Jr, C. S.; Sundstrom, V., Revealing the Ultrafast Charge Carrier Dynamics in Organo Metal Halide Perovskite Solar Cell Materials Using Time Resolved THz Spectroscopy. *Nanoscale* **2016**, *8*, 6249-6257.

44. De, S.; Pascher, T.; Maiti, M.; Jespersen, K. G.; Kesti, T.; Zhang, F.; Inganäs, O.; Yartsev, A.; Sundström, V., Geminate Charge Recombination in Alternating Polyfluorene Copolymer/Fullerene Blends. *J. Am. Chem. Soc.* **2007**, *129*, 8466-8472.

45. Savenije, T. J.; Ponseca, C. S.; Kunneman, L.; Abdellah, M.; Zheng, K.; Tian, Y.; Zhu, Q.; Canton, S. E.; Scheblykin, I. G.; Pullerits, T., et al., Thermally Activated Exciton Dissociation and Recombination Control the Carrier Dynamics in Organometal Halide Perovskite. *J. Phys. Chem. Lett.* **2014**, *5*, 2189-2194.

46. Wehrenfennig, C.; Eperon, G. E.; Johnston, M. B.; Snaith, H. J.; Herz, L. M., High Charge Carrier Mobilities and Lifetimes in Organolead Trihalide Perovskites. *Adv. Mater.* **2014**, *26*, 1584-1589.

47. Barnes, N. P.; Walsh, B. M., Amplified Spontaneous Emission-Application to Nd:YAG Lasers. *IEEE J. Quantum Electron.* **1999**, *35*, 101-109.

48. Kinder, J. M.; Mele, E. J., Nonradiative Recombination of Excitons in Carbon Nanotubes Mediated by Free Charge Carriers. *Phys. Rev. B* **2008**, *78*, *155429* 1-8.

49. Wright, A. D.; Verdi, C.; Milot, R. L.; Eperon, G. E.; Perez-Osorio, M. A.; Snaith, H. J.; Giustino, F.; Johnston, M. B.; Herz, L. M., Electron-Phonon Coupling in Hybrid Lead Halide Perovskites. *Nat. Commun.* **2016**, *11755* 1-9.

50. Piermarocchi, C.; Tassone, F.; Savona, V.; Quattropani, A., Exciton Formation Rates in GaAs/Al(x)Ga(1-x)As Quantum Wells. *Phys. Rev. B* **1997**, *55*, 1333-1336.

51. Bakulin, A. A.; Selig, O.; Bakker, H. J.; Rezus, Y. L.; Muller, C.; Glaser, T.; Lovrincic, R.; Sun, Z.; Chen, Z.; Walsh, A., et al., Real-Time Observation of Organic Cation Reorientation in Methylammonium Lead Iodide Perovskites. *J. Phys. Chem. Lett.* **2015**, *6*, 3663-3669.

52. D'Innocenzo, V.; Srimath Kandada, A. R.; De Bastiani, M.; Gandini, M.; Petrozza, A., Tuning the Light Emission Properties by Band Gap Engineering in Hybrid Lead Halide Perovskite. *J. Am. Chem. Soc.* **2014**, *136*, 17730-17733.

53. Tian, W.; Zhao, C.; Leng, J.; Cui, R.; Jin, S., Visualizing Carrier Diffusion in Individual Single-Crystal Organolead Halide Perovskite Nanowires and Nanoplates. *J. Am. Chem. Soc.* **2015**, *137*, 12458-12461.

54. Wahl, M., *Time-Correlated Single Photon Counting*; PicoQuant GmbH: Berlin, Germany, 2014, p 14.

55. Tian, Y.; Merdasa, A.; Unger, E.; Abdellah, M.; Zheng, K.; McKibbin, S.; Mikkelsen, A.; Pullerits, T.; Yartsev, A.; Sundström, V., et al., Enhanced Organo-Metal Halide Perovskite Photoluminescence from Nanosized Defect-Free Crystallites and Emitting Sites. *J. Phys. Chem. Lett.* **2015**, *6*, 4171-4177.

56. Tian, Y.; Peter, M.; Unger, E.; Abdellah, M.; Zheng, K.; Pullerits, T.; Yartsev, A.; Sundstrom, V.; Scheblykin, I. G., Mechanistic Insights into Perovskite Photoluminescence Enhancement: Light Curing with Oxygen can Boost Yield Thousandfold. *Phys. Chem. Chem. Phys.* **2015**, *17*, 24978-24987.

Chapter 5

5. An Introduction to Tau Protein and the Anti-Brownian Electrokinetic (ABEL) Trap for Non-Specialists: for the Wisconsin Initiative for Science Literacy

5.1 Protein Function

Proteins are the building blocks of life. Their unique sequence of amino acids determines their structure and function. Proteins come in various shapes, sizes, and function: antibodies are proteins that fight infections; hormones are proteins that coordinate bodily processes; structural proteins provide support to connective tissues; transport proteins move molecules around the body. These are just a few of the examples of proteins that the human body relies on to perform essential functions.

Since proteins are essential for life, what, then, happens when proteins malfunction? And what are the different ways that they can malfunction? These two questions have important ramifications for understanding disease and finding treatments. In my research, I have been concerned with tau protein. Tau protein is implicated in Alzheimer's disease and other neurodegenerative diseases. Even though the cause of these diseases is not well understood, the brains of patients with these neurodegenerative diseases often contain a buildup of aggregates of tau protein. Why the tau protein aggregates and why it no longer performs its intended function is an active area of research.

5.2 Tau Protein

Everyone has tau protein – it is an essential component of healthy brains. Tau protein is known as an intrinsically disordered protein or IDP because in its healthy (native) state it does not have a well-defined structure as some other proteins do. This means that tau protein is free to explore many different structures: sometimes it might be folded like a paperclip, sometimes it might be folded like an "S" (Figure 5-1). In the middle of the protein is a region known as the microtubule-binding region.

To understand tau protein, and its importance, imagine a railroad track that connects one station to the next. Different trains can move along these tracks carrying a variety of cargo. But when the railroad ties are torn up, the structural integrity of the tracks crumbles and they are no longer able to transport their cargo. A similar process happens in the brains of people with Alzheimer's disease.

Brains are primarily composed of neurons, special cells that contain a cell body, axon and dendrites (Figure 5-2). Microtubules function as the railroad tracks. They run along the axons of neurons and provide structural support and a mechanism for transport. Upon closer inspection, tau protein is found bound to

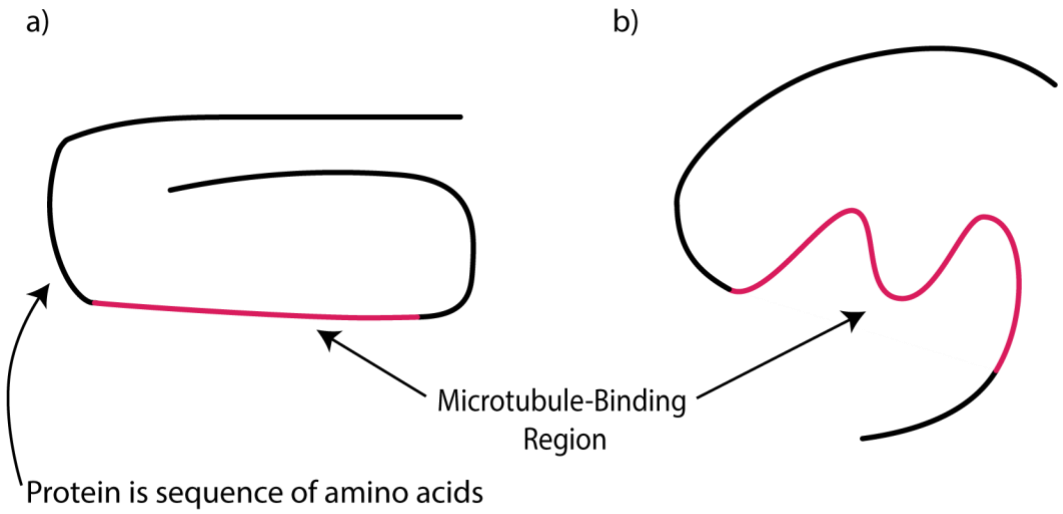

Figure 5-1. Possible structures of tau protein.

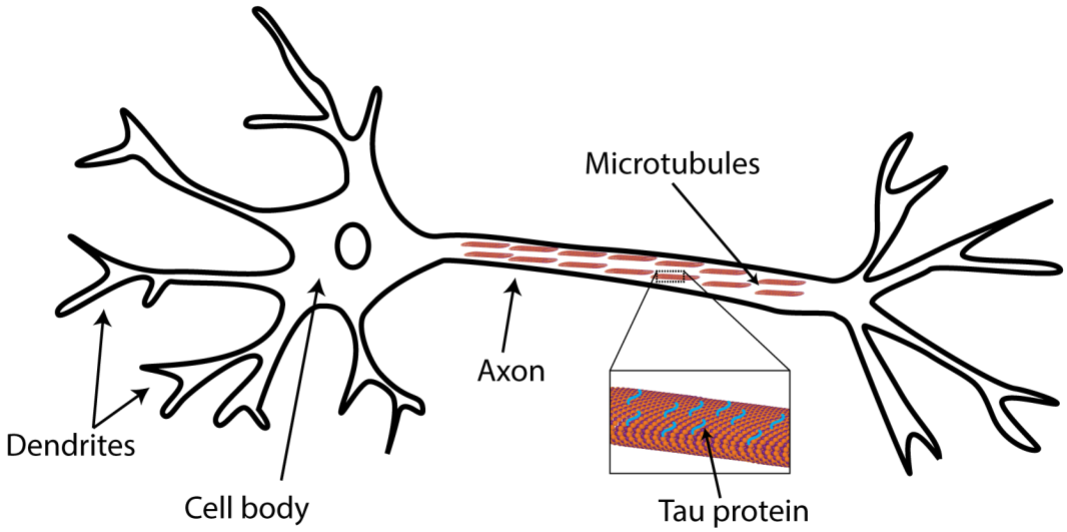

Figure 5-2. Schematic of neuron showing microtubules in the axon.

microtubules, stabilizing the tracks (i.e. railroad ties) (Figure 5-2, inset). But in the neurons of Alzheimer's patients, tau protein is no longer found attached to microtubules, but rather found in tangled clumps.

We are interested in learning more about the many structures that this protein adopts and how it behaves in solution so that we can understand how the molecule exists in the aqueous environment of the cell. We are also interested in learning about this molecule at the single-molecule level so that we can understand the heterogeneity, or mixture, of behavior before it begins to be harmful.

5.3 Single-Molecule Studies

Studying single molecules is a fairly recent path of experimentation. Traditional methods for studying a sample of protein, for example, have relied on looking at millions of molecules at a time. But when we look at millions of molecules at once, we miss information from the individual molecules. Imagine looking at a crowd of people at a concert and you are asked to gauge the energy of the crowd. People are moving and dancing, so you conclude that the energy level is high. But if you could take the time to look at each individual person, you might find that some people are dancing much more than others; your original

assessment of the energy level is not uniform across the crowd. The different energy of each person in the crowd cannot be understood by the ensemble measurement of looking out over the crowd, but a single-person measurement of looking at each individual could give a more detailed picture. Understanding the heterogeneity of a sample of molecules is similar to this: we want to know how each molecule moves independently so that we can learn more about properties that would otherwise be hidden.

Since we want to learn about individual molecules, and we want to learn about them in a relevant situation, we study proteins in a solution. Unfortunately, a protein in solution will not stand still while being observed on a microscope because it experiences Brownian motion. Brownian motion is a term to describe the natural, random movement of particles in solution. One way to overcome this phenomenon is to tether a molecule to the surface, essentially putting a leash on the molecule so that it does not float away. But putting a leash on a protein like tau protein, which does not have a defined shape, could force it into an unnatural configuration, thus distorting the data and making the experiment irrelevant to the true motion of the molecule. On the other hand, the molecule can be left to float freely in solution so that we only see it when it is in the field of view of the microscope. Even though we only get to see it for 0.001 seconds, its conformation is not being distorted. A third option would allow for a molecule to freely diffuse, but also cancel its natural, random motion so that it can be observed for a longer period of time. This third option is made possible by the anti-Brownian electrokinetic (ABEL) trap.

5.4 Anti-Brownian Electrokinetic (ABEL) Trap

The anti-Brownian electrokinetic trap, or ABEL trap, was developed at Stanford University in California, and is used in only a handful of labs around the world. The ABEL trap consists of a microfluidic device, a rotating laser spot, and feedback voltages (Figure 5-3).

A microfluidic device is used to hold and control small volumes of liquid, typically less than ~1/5th of one teaspoon (or 1 milliliter). The ABEL trap microfluidic holds ~1/5000th of one teaspoon (or 1

microliter). Even with this small volume, there are still approximately 602,000 individual protein molecules in the trap. If approximately 40,000 of these protein molecules were to lie end-to-end, they would span the width of a typical human hair. There are 4 reservoirs in the microfluidic, each containing an electrode that will be used to apply feedback to the molecule of interest.

The laser travels around a grid of 32 spots, spending ~800 nanoseconds (0.00000008 seconds) at each spot (Figure 5-3b). Only one of the 32 spots are illuminated at a given time. When the location of the laser overlaps with the location of the protein, a fluorophore attached to the protein is illuminated and excited. A fluorophore is a special type of molecule that, when excited, will emit fluorescence, similar to materials that glow in the dark. Think of the molecule as a person in a dark room. Without light, the person cannot be located. But if the person turns on a flashlight, then it becomes easier to estimate where we expect the person to be standing. In this analogy the flashlight is the fluorophore, and the person is the molecule we are interested in.

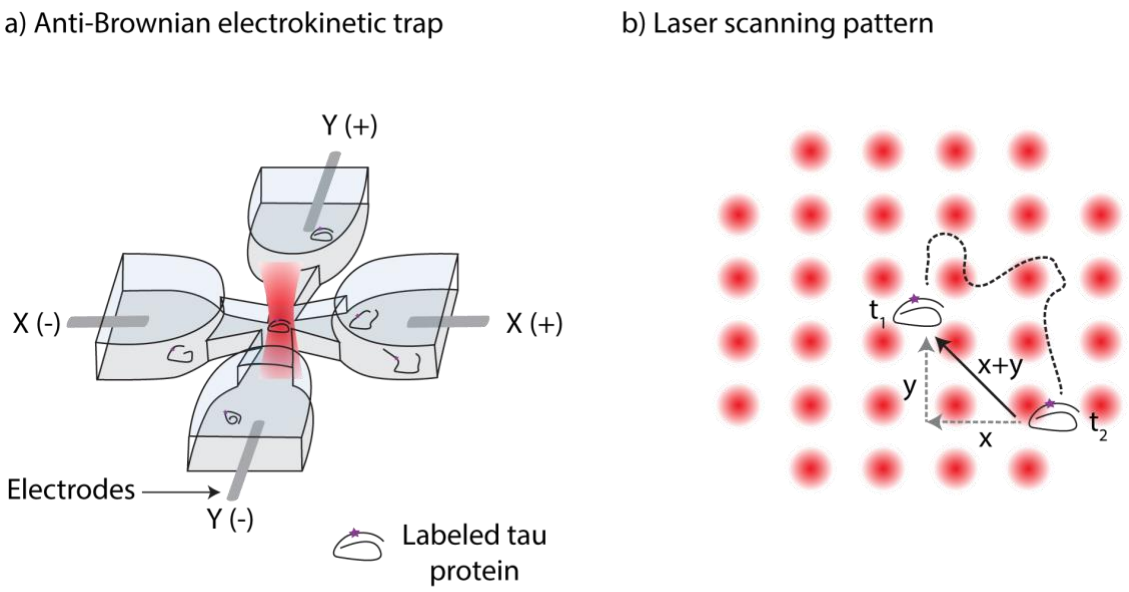

Figure 5-3. Anti-Brownian electrokinetic (ABEL) trap design. (a) Microfluidic device showing tau protein in the trap and 4 electrodes. (b) A molecule moves from its initial position at t_1 to a position at t_2 via Brownian motion along the dashed line. The electrodes then exert a force in the x and y directions to push the molecule back to center.

Once we know where the protein is, it is time to apply feedback voltages. These bursts of electricity will cause the solution in the microfluidic to flow in a particular direction, dragging the molecule with it.

Imagine a molecule initially at t_1 in Figure 5-3b. This is the ideal position for the molecule — right in the center. But as detailed earlier, the molecule will move away from this spot via Brownian motion, as indicated by the black dashed line, to a new position at t_2. The system now finds the molecule at this new position and calculates the electricity to apply to push the molecule back to its original position. There are two sets of electrodes that will be used to apply the feedback in the x- and y-directions (gray dashed lines). Combining a force in the x-direction and a force in the y-direction will give an overall force that moves the molecule diagonally (black arrow).

5.5 Fluorescence anisotropy

Now that we have a molecule of interest trapped in our ABEL trap, we want to learn as much information as possible. We will use the fluorophore, the flashlight, attached to the molecule as a proxy for understanding what conformations the molecule is adopting since we cannot see the molecule directly. One way to do this is to measure anisotropy. Anisotropy is a measure of the extent of polarized emission when a molecule is excited with polarized light. Let's look at this a little more closely to find an intuitive understanding of this phenomenon and why it is helpful for our experiments.

Light has polarization. You may have experienced this polarization when you wear polarized sunglasses — the world looks different if you hold your head upright vs. tilted to one side. If you looked at a computer screen with perfectly polarized light, in one orientation you would be able to see something on the screen while wearing your polarized glasses, and then by tilting your head, the screen would appear completely dark because no light is able to pass through your polarized lenses.

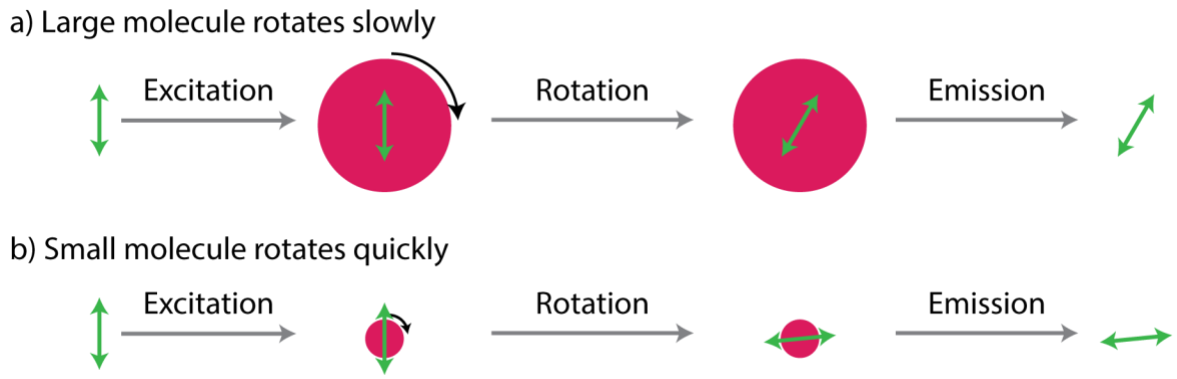

Figure 5-4. Anisotropy measurement shows how much the molecule has rotated. A photon (green double-headed arrow) interacts with a molecule (pink circle) and the molecule is excited. The molecule then moves and rotates, and the orientation of the photon is also changed so that when the photon is emitted, the photon is in a different orientation than when it excited the molecule. (a) A large molecule rotates slowly and (b) a small molecule rotates quickly so that the orientation of the emitted green arrow is different.

We will be exciting our molecules with polarized light so that all the molecules absorb light with a specific orientation. A molecule absorbs a "photon" of light (a term for a bundle of light energy) when the light is oriented in one direction, say vertically (Figure 5-4). But when the molecule releases that light, the molecule has moved and rotated in solution and will release the light in a different orientation, say diagonally. Based on the polarization of this emission light (orientation of green arrow in Figure 5-4 on right), we can determine how much the molecule rotated while it was "holding onto" the light. The extent that the molecule has rotated during the period of time the molecule holds onto the light will provide information about the conformation of the protein — a person swimming in a pool will somersault slower when not holding her legs in tightly than when curled tightly into a ball. This measurement, therefore, allows us to understand how compact the protein is while it rotates and moves through the solution.

5.6 What We Have Learned

Using this method, we have studied the single-molecule motions of tau protein in solution. We used anisotropy as a way to describe how much these molecules rotated in solution, which we then used to describe the variety of conformations that the protein adopts. When we plotted a distribution of these

anisotropy values, we found that there were two distinct peaks, indicating that there were some molecules that tumbled faster (more compact structures), and some that tumbled slower (less compact structures). This work contributes to the needed understanding of the conformations of tau protein since the conformation of tau protein may be important for determining disease pathology. One possible interpretation of this finding is that one conformation is more prone to the pathological aggregation seen in neurodegenerative diseases, but more studies are needed to fully characterize the biological ramifications. From here, studying the anisotropy of this same protein in the presence of factors that induce or hinder aggregation of the protein can provide information about the changes in conformation experienced under such conditions, which could have relevance to understanding disease progression and potential therapeutic treatments.

Appendix A

6. Supplemental Experimental Details and Procedures

Unless otherwise noted, anytime N_2 was used to blow something dry, it was house N_2 passed over desiccant, through a 0.2 µm Whatman PTFE membrane filter and pipet tip. Anytime a solution was "pushed" through the trap, it refers to using a syringe and tubing to inject solution into the trap instead of using a pipet and letting the surface tension draw the liquid inside. Injectors were made by cutting the sharp point off of a syringe needle, using 1/16" inner diameter tygon tubing (1/8" outer diameter, 1/32" wall thickness) then a small piece of pipet tip was pushed into the end of the tubing to keep the end open while holding it (Figure 6-1).

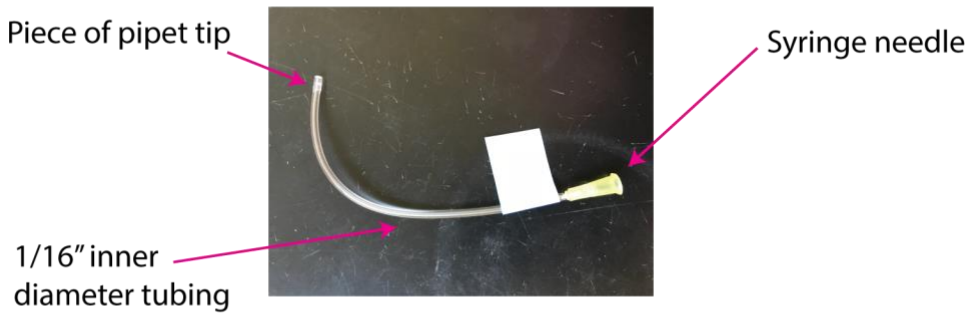

Figure 6-1. Injector used for pushing solution through ABEL trap.

6.1 Preparing Solutions for Single-Molecule Experiments

6.1.1 Cleaning glycerol via extraction and photobleaching

I hear tell of a time when people wished their solvents were as clean as glycerol. We are no longer living in that time. A year-long search ensued to find the best way to clean glycerol for single-molecule experiments using green excitation. This search included, but is not limited to: using sucrose instead, photobleaching for days to weeks, distillation, charcoal-cleaning, buying glycerol from different companies and different lots (the following protocol will list batch/lot numbers for reagents that I have used). In the end, we switched to red excitation to excite fewer impurities and settled on the following protocol for ridding glycerol of enough impurities that it could be used. This procedure produces about 45 – 50 mL of cleaned glycerol and requires about 2.5 – 3 hours for the extraction part, plus time for photobleaching.

HPLC grade acetone, HPLC grade methanol and nanopure water (18.2 MΩ) were used to rinse 2 glass vials, 125 mL separatory funnel (including stopcock and stopper), 2 separate 50 mL round bottom flasks, 100 mL round bottom flask, and a stir bar. The glassware was then dried thoroughly and plasma cleaned in O_2 plasma (300 W, 5 min).[6]

About 50 mL of glycerol (J.T. Baker, Avantor Performance Materials, product number 4043-00, batch 93586) was added to the separatory funnel and used to "grease" the stopcock. Then about 50 mL of 2,2,4-trimethylpentane (Fisher Scientific 22901; lots N07A522, R30A731, M27C703) was added. The separatory funnel was shaken vigorously, then allowed to separate for 15-20 min. The first few drops of glycerol were collected in a waste beaker, then the rest was collected in a cleaned 50 mL round bottom flask. The 2,2,4-trimethylpentane was poured into a solvent waste beaker and the collected glycerol was

[6] At one point I tried to scale up the cleaning process and was unable to fit the separatory funnel in the plasma cleaner. The resulting glycerol was not clean. I do not know if that is because of the lack of plasma cleaning or not.

added back to the separatory funnel.[7] This extraction process was repeated for a total of 3 times, collecting the last extraction in a 100 mL round bottom flask equipped with a stir bar. The glycerol was stirred at 110 °C for 1 hour, then divided into the two glass vials and placed in the photobleacher for 3-4 days (Figure 6-2).[8]

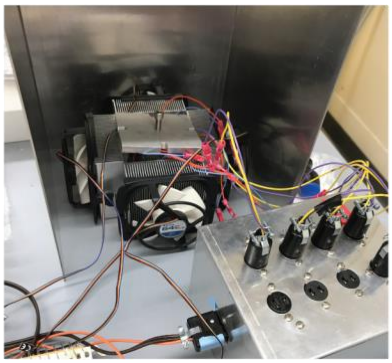

Figure 6-2. Photobleaching unit for cleaning glycerol.

6.1.2 Preparation of PCA and PCD

Protocatechuic acid (PCA) was recrystallized to improve its solubility, according to a protocol retrieved from the Hoskins lab. A water bath was prepared and heated to 105 – 165 °C. PCA (~5 mL powder) was dissolved in 5 mL nanopure water in a 50 mL falcon tube and placed in the water bath to dissolve the PCA. Once the PCA was dissolved, it was placed on ice for 10 min. The PCA was then filtered using a Buchner funnel and vacuum filtration, and it was rinsed with chilled nanopure water. The PCA was recrystallized in this fashion three more times, then the PCA crystals were left on filter paper to dry after the fourth and

[7] The 2,2,4-trimethylpentane is poured out the top so that the bottom is not contaminated with impurities.

[8] We use the higher-powered photobleacher, or as Randy called it, the “cracked-out” photobleacher.

final recrystallization. The crystals were stored at –80 °C.[9] A solution of 50 mM PCA in nanopure water was filtered with a 0.2 µm Whatman PTFE membrane filter and aliquoted.

Protocatechuate 3,4-dioxygenase (PCD) was purchased from Sigma Aldrich (P8279-25 UN, 3 U/mg) and prepared as 48 U/mL by adding 50 mM Tris HCl, pH 8.8 to 25 UN of PCD. Aliquots were stored at –80 °C.

6.2 Making ABEL Traps from Fabricated Pieces

All ABEL traps used in this work were fabricated by Dr. Kevin D. Heylman, Ph.D. Fabricated pieces were diced in WCAM and stored coated with photoresist. Drilling holes for the electrodes and bonding to a fused silica coverslip were done at Chemistry.

Holes were drilled into fabricated pieces in the student machine shop. Alignment of the holes is crucial; they must be within the "mushroom top" so that the trap is able to bond correctly (Figure 6-3a). To accomplish this alignment, we drilled a hole into a piece of glass, aligned the mushroom top to the hole

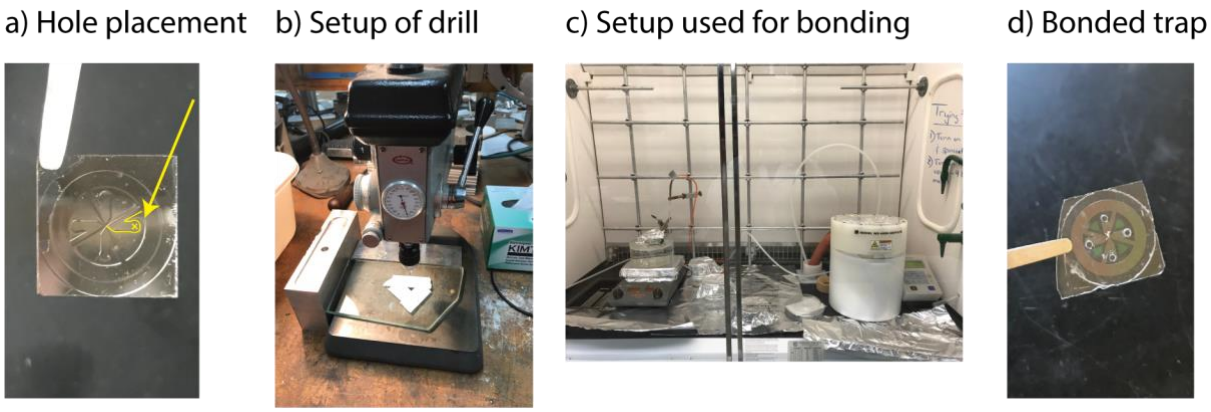

Figure 6-3. Making ABEL traps. (a) View of fabricated piece showing location where hole should be drilled (X). Yellow outline used to define the shape of the "mushroom top" of the fabricated piece. (b) Drill setup, showing metal blocks for aligning and fabricated piece taped onto a glass plate. (c) Setup of the hood with hot KOH (left) and spincoater (right). (d) Fully bonded ABEL trap.

[9] There may not be any real reason to store PCA crystals at –80 °C. The Hoskins lab says that it is just convenient for them to store them in the –80 °C, so we continue this tradition.

(fabricated side is face up), taped the trap down, squirted some nanopure water on the trap piece, then drilled the hole. Metal blocks were used on the back and side of the drill to align the glass plate (Figure 6-3b). Diamond drill bits (0.75 mm) were purchased from Kingsley North Inc (product 1-0500-25). Holes were drilled using these diamond drill bits at maximum drill speed. Each drill bit was used to create 4 – 6 holes. It was important to change drill bits frequently to keep clean holes. With each hole, the plate was cleaned of grit before taping the fabricated piece down again.

Bonding the fabricated piece to the fused silica coverslips (Esco Optics, R425025, 25.0 x 25.0) is based on literature precedent.[1-2] Photoresist was removed by soaking fabricated pieces in HPLC grade acetone overnight. Fabricated pieces and coverslips were then sonicated in HPLC grade acetone for 5 min, then rinsed with HPLC grade acetone, HPLC grade isopropanol, HPLC grade ethanol and nanopure water.[10] A 40 % wt KOH solution was heated to 70 °C in a water bath; a 7 % solution of sodium silicate was prepared and filtered with a 0.2 µm Whatman PTFE membrane filter. A cleaned fabricated piece was set into the KOH for 2 min, removed, rinsed in two large beakers of nanopure water, and blown dry with N_2. The fabricated piece was placed, fabricated side up, onto a lens paper. A coverslip was then added to the KOH and let stand for 2 min before rinsing twice and being blown dry. The coverslip was placed on a spincoater and 150 µL of 7 % sodium silicate solution was added to the center and the coverslip was spun for 25 sec on 4000 RPM with the fastest acceleration (Figure 6-3c). The coverslip was then removed and placed firmly onto the fabricated piece. If contact was not complete and parts of the trap were not bonded, they were sonicated in water to break them apart and the pieces were reused. Bonded traps were annealed by placing them on a hotplate at 90 °C and increasing the temperature by 15 °C every 15 min to reach 200 °C, where it was held for >12 hours.

[10] During this whole process, care was taken not to introduce dust or dirt that could interfere with complete bonding. Hair was pulled back, gloves were changed often, and everything was covered with foil. If dust was noticed in any beaker, the beaker was rinsed and replenished. If a coverslip was broken at any point in the process, it was cleaned from the beginning of the protocol and any solution the broken coverslip touched was replaced to dispose of any glass shards.

6.3 Making Electrodes

Electrodes for the ABEL trap were made by stripping about ¼" from the end of a skinny wire and soldering Pt wire onto it. Then black heat shrink was placed around the solder and heated to shrink (Figure 6-4).

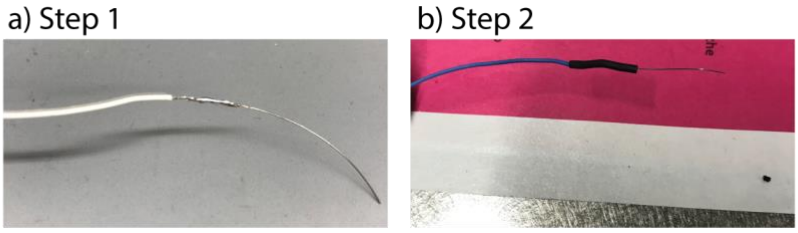

Figure 6-4. Making electrodes. (a) Step 1 is to solder Pt wire to a coated wire. (b) Step 2 is to place heat shrink over the solder to secure.

6.4 Cleaning ABEL Traps

ABEL traps were cleaned daily.[11] We have tried occasionally to use them on the second or third day after cleaning but trapping ability decreases. Traps were stored at the end of each day by pushing nanopure water through (to remove glycerol), then stored in nanopure water. Traps were blown dry using N_2. Nanopure water was added to the trap via pipet and blown dry twice.[12] Excess glycerol was wiped from the surface using methanol before placing them in a UV-Ozone cleaner (Novascan Technologies) for 30 min to remove all organic matter from the trap.

1 M KOH solution was pushed through the trap to ensure that the trap filled completely. The traps were then placed in a coverslip holder in a plastic beaker filled with 1 M KOH and sonicated for 15-30 min. The traps were removed from KOH and rinsed with nanopure water and blown dry with N_2. A pipet was used to fill the inside with water twice, and it was blown dry with N_2 after each filling.

[11] ABEL trap cleaning is a great time to catch up on music, podcasts, a good audio book, or contemplate the meaning of life (as Veronica suggests).

[12] At this point you should be able to see well-defined channels in the center.

*6.4.1 **Piranha cleaning ABEL traps***

There are times when cleaning the ABEL trap via normal methods does not remove contaminants. At these times we use a piranha solution to clean the traps. Prior to cleaning with piranha, the traps are cleaned via the usual protocol (see section 6.4). A fume hood was cleared of all organics. A 250 mL beaker equipped with a stir bar was placed in a secondary container on a hotplate. First, 75 mL of concentrated sulfuric acid was added to the beaker, then 25 mL of 30 % hydrogen peroxide was added. The reaction was stirred and bubbles and heat were observed. The traps were then dipped into the solution, one hole at a time, to allow them to start to fill. The solution of piranha is viscous and complete filling is uncommon, but most of the time some piranha will wick into the trap. The traps were left to sit for 1 hour, then rinsed in 2 baths of nanopure water and blown dry with N_2. Water was pushed through with a syringe and the trap was blown dry again. Then 1 M KOH was pushed through the trap and the traps sat in 1 M KOH overnight.[13] Used piranha solution was disposed of in the piranha waste container.

6.5 Layering ABEL Traps with Polyelectrolyte Layers

Traps are layered with polyelectrolyte layers to improve trapping. Solutions of 1 mg/mL polyethyleneimine (PEI; positively charged) and 1 mg/mL polyacrylic acid (PAA; negatively charged) are layered consecutively as PEI, followed by PAA, PEI and finishing with PAA (4 layers total). To deposit a layer, the solution is pushed into a clean trap and left to sit for 10 min. The trap is then blown dry with N_2; then water is pushed through the trap and blown dry before adding the next layer. After the terminating layer, the trap was rinsed twice with water. We have tried only depositing two layers (PEI then PAA), but surface

[13] Once traps have undergone piranha cleaning, they are named with consecutive P's after their number. Sometimes it is difficult to keep track of which trap is which in the bath. In this case, continue numbering the traps (i.e. trap 1 becomes trap 2P) so that it is clear that trap 1 and trap 1P are not the same trap, but it is also clear that trap 2 has been in piranha.

coverage was incomplete, and trapping was not ideal. Traps were used on the same day that layers were deposited for best results.

6.6 Determination of Fundamental Anisotropy

In order to determine the fundamental anisotropy, r_0, for a sample, a Perrin plot was generated using bulk fluorimeter anisotropy measurements of the sample of interest in increasing amounts of glycerol. The plot of anisotropy^{-1} vs. viscosity^{-1} was fitted to a straight line, with y-intercept = $1/r_0$. This provided the experimental r_0 value. Viscosity values were determined from the literature for a solution of aqueous glycerol at 20 °C.[3] An example is shown below (Figure 6-5).

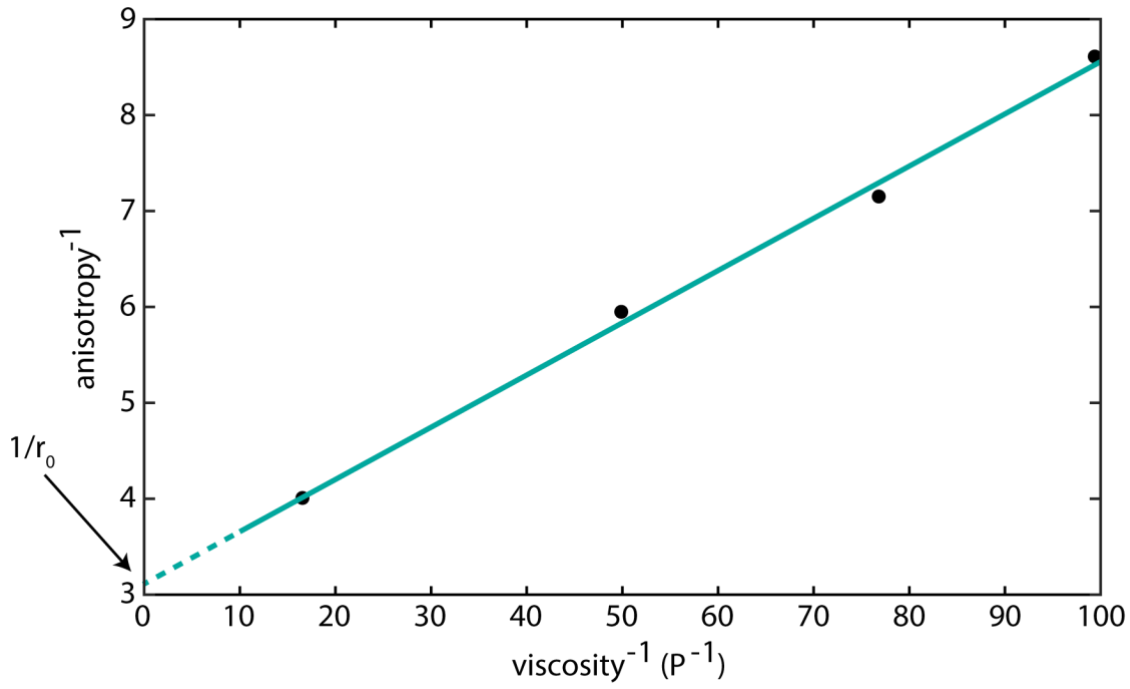

Figure 6-5. Example Perrin plot for determining fundamental anisotropy of htau40-310-ATTO647N. From the y-intercept of the equation y = 0.054x + 3.1, the fundamental anisotropy, r_0, can be found.

6.7 References

1. Wang, H. Y.; Foote, R. S.; Jacobson, S. C.; Schneibel, J. H.; Ramsey, J. M., Low temperature bonding for microfabrication of chemical analysis devices. *Sens. Actuators, B* **1997**, *45*, 199-207.

2. Khandurina, J.; McKnight, T. E.; Jacobson, S. C.; Waters, L. C.; Foote, R. S.; Ramsey, J. M., Integrated system for rapid PCR-based DNA analysis in microfluidic devices. *Anal. Chem.* **2000**, *72*, 2995-3000.

3. Segur, J. B.; Oberstar, H. E., Viscosity of Glycerol and Its Aqueous Solutions. *Ind. Eng. Chem.* **1951**, *43*, 2117-2120.

Appendix B

7. Brief Glossary of Acronyms/Shorthand

- **APD:** avalanche photodiode (on the ABEL trap setup, the term vertical is used synonymously with parallel polarization [relative to excitation polarization], and horizontal is synonymous with perpendicular polarization [relative to excitation polarization]. In some cases, the APDs were labeled as APD0 and APD1 [vertical and horizontal, respectively], and in others they were APD1 and APD2 [vertical and horizontal, respectively]. Context will help differentiate, but just be aware of this idiosyncrasy.)
- **GdmCl:** guanidinium chloride (used for denaturing protein)
- **hT40/htau40:** full-length tau protein (441 residues)
- **htau40-wt**: full-length tau protein (441 residues) from the Margittai lab with C291S and C322S
- **Millipore water/nanopure water:** refers to all water purified at 18.2 MΩ.
- **PAA:** polyacrylic acid (negatively charged PEL)
- **PCA:** protocatechuic acid or 3,4-dihydroxybenzoic acid (used with PCD for oxygen scavenging system)
- **PCD:** protocatechuate 3,4-dioxygenase (used with PCA for oxygen scavenging system)
- **PEI:** polyethyleneimine (positively charged PEL)
- **PEL/PEM:** polyelectrolyte (mono)layers
- **Trimethylpentane:** 2,2,4-trimethylpentane (used for cleaning glycerol)

> **Trolox:** (±)-6-Hydroxy-2,5,7,8-tetramethylchromane-2-carboxylic acid (triplet state quencher)

> **Quartz coverslip:** refers to fused silica coverslips (fused silica has the same purity as quartz, but different crystal structure. I was originally told they were quartz coverslips, so that language stuck.)